The Response of Stratospheric Water Vapor to a Changing Climate: Insights from In Situ Water Vapor Measurements

Professor James G. Anderson Maryann Racine Sargent

The response of stratospheric water vapor to a changing climate: Insights from in situ water vapor measurements.

Abstract

Stratospheric water vapor plays an important role in the Earth system, both through its role in stratospheric ozone destruction and as a greenhouse gas contributing to radiative forcing of the climate. Highly accurate water vapor measurements are critical to understanding how stratospheric water vapor concentrations will respond to a changing climate. However, the past disagreement among water vapor instruments on the order of 1 – 2 ppmv hinders understanding of the mechanisms which control stratospheric humidity, and the reliable detection of water vapor trends.

In response to these issues, we present a new dual axis water vapor instrument that combines the heritage Harvard Lyman-α hygrometer with the newly developed Harvard Herriott Hygrometer (HHH). The Lyman-α instrument utilizes ultraviolet photo-fragment fluorescence detection, and its accuracy has been demonstrated though rigorous laboratory calibrations and in situ diagnostic procedures. HHH employs a tunable diode near-IR laser to measure water vapor via direct absorption in a Herriott cell; it demonstrated in-flight precision of 0.1 ppmv (1-sec) with accuracy of 5%±0.5 ppmv. We describe these two measurement techniques in detail along with our methodology for calibration and details of the measurement uncertainties. We also examine the recent flight comparison of the two instruments with several other in situ

hygrometers during the 2011 MACPEX campaign, in which five independent instruments agreed to within 0.7 ppmv, a significant improvement over past comparisons.

Water vapor measurements in combination with simultaneous in situ measurements of O_3, CO, CO_2, HDO, and HCl are also used to investigate transport in the Tropical Tropopause Layer (TTL). Data from the winter 2006 CR-AVE campaign and the summer 2007 TC4 campaign are analyzed in a one-dimensional mixing model to explore the seasonal importance of transport within the TTL via slow upward ascent, convective injection, and isentropic transport from the midlatitude stratosphere. The model shows transport from midlatitudes to be significant in summer and winter, affecting ozone concentrations and therefore the radiative balance of the TTL. It also shows significant convective influence up to 420 K potential temperature in both seasons, which appreciably increases the amount of water vapor above the tropopause.

Table of Contents

Chapter 1

Introduction

"Considering the whole span of earthly time... Only within the moment of time represented by the present century has one species – man – acquired significant power to alter the nature of his world."

–Rachel Carson, from "Silent Spring"

1.1 Thesis Motivation

As the Earth's population grows beyond 7 billion people, it becomes increasingly clear that humankind has the power to impact the planet in profound ways. Man's efforts to obtain food, water, shelter, and energy have dramatically altered the Earth system, in some ways that are irreversible on human timescales. In particular, the burning of fossil fuels and release of carbon dioxide into the atmosphere continues to alter the climate system at a remarkable rate. Though the Earth has experienced various climate regimes in the past, the current rate of temperature growth far exceeds the pace of past changes. Increasing global temperatures are predicted to lead to rising sea level, threatening coastal communities around the globe, and increasing occurrence of extreme weather events such as droughts, heat waves, and floods. Climate change will also affect water supplies, crop productivity, and potentially UV dosage levels. It is therefore of critical importance to understand how increasing greenhouse gases impact all aspects of the climate system, and the complex feedbacks initiated by human activity.

By obtaining the best possible understanding of the consequences of our actions, we can more effectively motivate policy choices to ensure a sustainable future.

1.1.1 The Greenhouse Effect

The main source of energy to the Earth is shortwave radiation emitted by the sun, primarily in the visible, near-ultraviolet, and near-infrared. At the top of the atmosphere, the Earth intercepts 5.4 x 10^{24} J/yr (5.4 YJ/yr) of energy from the sun, 30% of which is reflected back to space, while 70%, or 3.8 YJ/yr, is absorbed by the Earth's surface. The Earth reemits this energy as longwave radiation in the infrared, which at steady state must balance the incoming solar radiation. In the absence of an atmosphere, basic physics can be used to calculate from this energy balance that the average surface temperature of the Earth would be 255 K. However, the presence of CO_2, H_2O, CH_4, and N_2O in the Earth's atmosphere dramatically alters this radiative balance by absorbing outgoing infrared radiation and reemitting it approximately isotropically. Because half of this reemitted radiation is directed back towards the surface of the Earth, it increases the total amount of energy directed towards the surface, thereby elevating the surface temperature. This cycling of energy, known as the greenhouse effect, results in 5.2 YJ/yr of energy being redirected to the surface, which is on the order of the amount of energy from the sun which initially reaches the planet. The natural greenhouse effect is primarily responsible for raising the average surface temperature of the Earth from 255 K to the observed 288 K [*Spiro and Stigliani*, 2003; *IPCC*, 2007].

Simple physics shows that increases in the concentration of greenhouse gases which have been observed over the last century should result in warming of the Earth's surface by increasing the amount of energy retained within the climate system. Although uncertainties remain in

predicting the magnitude of climate warming because of positive and negative feedback mechanisms in the climate system, the importance of the greenhouse effect and atmospheric greenhouse gases is indisputable.

1.1.2 Global Energy Consumption

Mankind has fundamentally altered the concentrations of greenhouse gases in the Earth's atmosphere through the burning of fossil fuels, which emit carbon dioxide into the atmosphere. Fossil fuels, including coal, oil, and natural gas, have been burned in massive quantities to drive human enterprise since the industrial revolution in the late 18th century. In the burning of fossil fuels, carbon from plant matter which was buried beneath the Earth's surface over the course of millions of years is converted into carbon dioxide and released into the atmosphere. Although these fuels have been used for the last 200 years, steadily converting buried carbon to atmospheric CO_2, the world's growing population and wealth will make energy consumption over the next several decades greater than that from the last two centuries combined.

To examine in more detail the evolution of global energy demands, we break down the total energy consumption as the product of global population, average per capita wealth, and energy intensity of the global economy [*Ehrlich and Holdren*, 1971; *Harrison et al.*, 2000]:

$$Total\ Energy\ [J] = (Population\ [\#]) * (GDP\ per\ capita\ [\$/\#]\ ) * (Energy\ use\ per\ dollar\ [J/\$])$$

The evolution of these terms over time determines the growth of global energy demand, and is shown in Figure 1.1 for 1971-2009. In 2009, for example, global population was 6.8 billion, per capita GDP was \$8,588, and energy intensity was 8.8×10^6 J/\$. Multiplying these terms gives 5.12×10^{20} J/yr, or 512 EJ/yr, as the total annual global energy consumption in 2009. Notice that although energy intensity fell over that period, the increasing population and per capita wealth

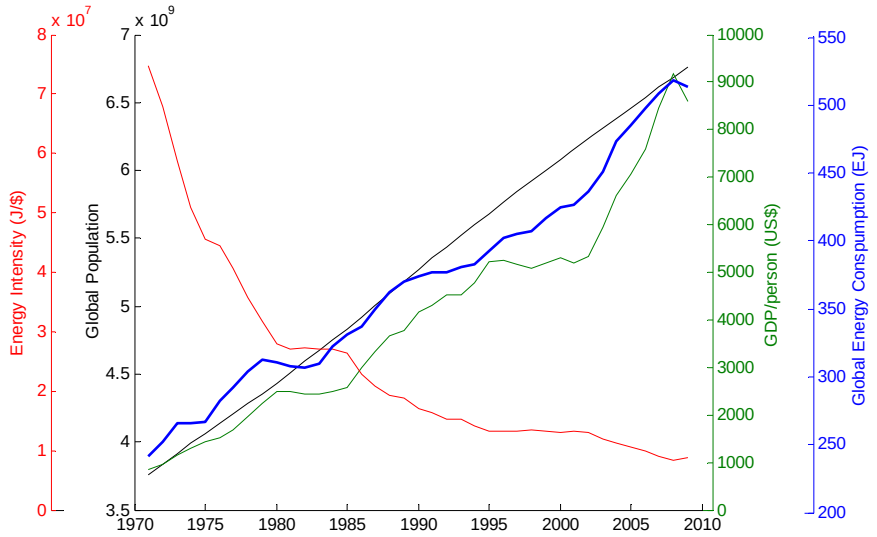

Figure 1.1: Global population, GDP per person, energy intensity, and total energy consumption for 1971-2009 [Data from *The World Bank*, 2012].

led to more than doubling of the total global energy consumption between 1971 and 2009. Figure 1.2 (left) shows the primary fuels which have been used since the industrial revolution to make this increasing energy consumption possible. Notice that very little of the growth in energy consumption has come from renewable sources, and by far the dominant sources of global energy are coal, oil, and natural gas, all fossil fuels whose combustion emits carbon dioxide. Currently 80% of global energy demand is met by fossil fuels, and without dramatic policy changes, our dependence on these fuels is predicted to continue for the next several decades.

Looking to the future, increasing global population and wealth will have vast implications for energy consumption. Global population is projected to reach 9.3 billion by 2050, a 33% increase over today, and 10.1 billion by 2100, a 44% increase [*United Nations Population Division*, 2011]. In the absence of other factors, these population increases would lead to a proportional increase in energy consumption, causing global energy use to reach 680 EJ in 2050. The potential for growth in consumption due to increasing per capita wealth is even greater, particularly considering the future growth in the economies of developing nations. With

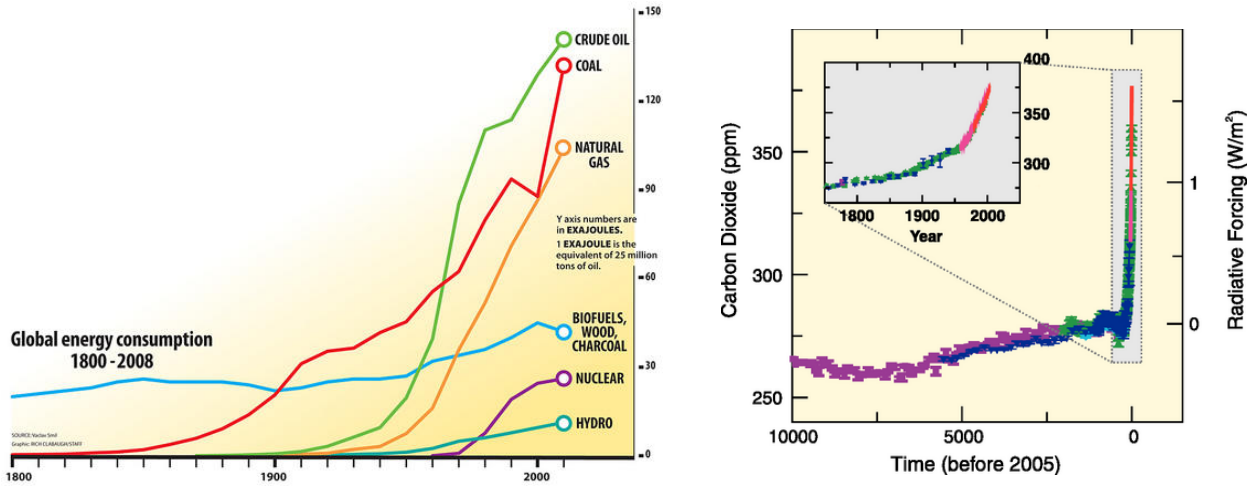

Figure 1.2: Left: Global energy consumption from 1800-2008 broken down by energy source [*Kurczy*, 2010]. Right: Atmospheric carbon dioxide concentration from 10,000 years ago to the present and associated radiative forcing [*IPCC*, 2007].

1.3 billion people in China and 1.2 billion in India, the growth in income in these countries will greatly increase future energy demands. China's per capita GDP grew at 3 times the global average over the last two decades, yet it remains at 15% of the per capita GDP of developed nations. As recently as 2000, China used only half as much energy as the United States, but by 2009 the country became the world's largest energy consumer. While projections remain highly sensitive to assumptions of China's economic growth, the country is expected to account for 36% of the increase in global energy demand by 2035, with India accounting for 18% of the increase [*World Energy Outlook*, 2010]. These increases will be offset somewhat by new technologies which increase energy efficiency, but global energy consumption is nonetheless predicted to double from today's levels by 2055, and to triple by 2100 [*Lewis and Nocera*, 2006]. In fact, the rapid population migration from rural to urban areas in the most rapidly developing economies may cause global energy demand to exceed even these projections. We conclude that though fossil fuels have been burned for the last 200 years as a source of energy, due to the rapidly increasing global population and wealth, energy demands over the next several decades

have the potential to alter the Earth system to a greater extent than all of past consumption combined.

Let us now consider how this energy consumption has affected atmospheric carbon dioxide concentrations in the past, as well as projections for the future. Carbon dioxide's long atmospheric lifetime means that even if CO_2 emissions are curtailed completely in the future, past emissions will continue to impact climate for many centuries, with 20-50% of emissions remaining in the atmosphere after 1000 years [*Archer et al*., 2009]. The right panel of Figure 1.2 shows atmospheric carbon dioxide concentrations over the past 10,000 years. From prior to the industrial revolution to 1980, CO_2 concentrations in the atmosphere grew by 20%, from 280 to 339 ppmv. By 2012, CO_2 concentrations reached 393 ppmv, 40% greater than pre-industrial times [*NOAA ESRL*, 2012]. Every emission scenario considered by the *IPCC* [2007] predicts doubling of CO_2 relative to pre-industrial times by 2100, with half of the scenarios predicting doubling by 2050 and a 150% increase by 2100. Unless drastic measures are taken, more CO_2 will be emitted to the atmosphere by fossil fuel burning in the next 30-50 years than was emitted in the last two centuries combined.

1.1.3 Consequences of Climate Change

Past anthropogenic emissions of CO_2, CH_4, and N_2O have increased radiative forcing of the climate system by an estimated 2.3 W/m^2 [*IPCC*, 2007]. This effect has been partially offset by anthropogenic contributions to aerosols which reflect shortwave radiation and cool the planet, but the net effect has been an increase in radiative forcing of ~1.6 W/m^2 [0.6-2.4 W/m^2] and an increase in global average temperature of 0.74 ^{o}C over the last 100 years. The IPCC predicts that doubling of CO_2 from pre-industrial levels would generate a ~4 W/m^2 increase in forcing,

leading to a 2–4.5 ^{o}C increase in average global temperature. Integrating over the surface of the Earth for one year, this forcing is equal to 0.06 YJ/yr of additional energy in the Earth's climate system. For comparison, the energy required to melt the Greenland ice sheet is ~0.78 YJ, meaning that if 10% of the increased energy acts to melt ice, Greenland would fully melt in 130 years.

This additional radiative forcing will alter the planet in varied and profound ways. Rising sea level due to both melting of continental ice sheets and thermal expansion of the oceans is one of the most potentially damaging consequences of climate change. Greenland and the West Antarctic ice sheet each contain enough ice to raise sea level by 7 m. One study predicts that the 3 ^{o}C temperature increase predicted due to a doubling of CO_2 would be sufficient to eliminate the Greenland ice sheet with the exception of residual mountain glaciers over a period of 1,000 years. That study did not include ice dynamics, which could significantly accelerate the process of ice loss. If Greenland melts to the point of exposing the land surface, it will reflect less sunlight leading to enhanced warming of the continent, in a cycle of melting that would be irreversible on human timescales, even if global temperatures were to return to preindustrial levels [*Gregory et al*., 2004]. In addition, thermal expansion of the oceans could lead to substantial sea level rise, with the IPCC [2007] predicting increases of 0.2-0.5 m 2100 due to thermal expansion alone. Thermal expansion of the oceans is also irreversible on the timescale of 1,000 years due to the slow process of ocean heat uptake, in which the energy associated with increased surface temperatures slowly mixes into the ocean depths on a timescale of 1000 years [*Solomon et al*., 2009]. Others suggest that the role of thermal expansion could be relatively minor based on evidence from the last interglacial period, during which the Antarctic ice sheet may have contributed the majority of increased sea level. However, if thermal expansion is

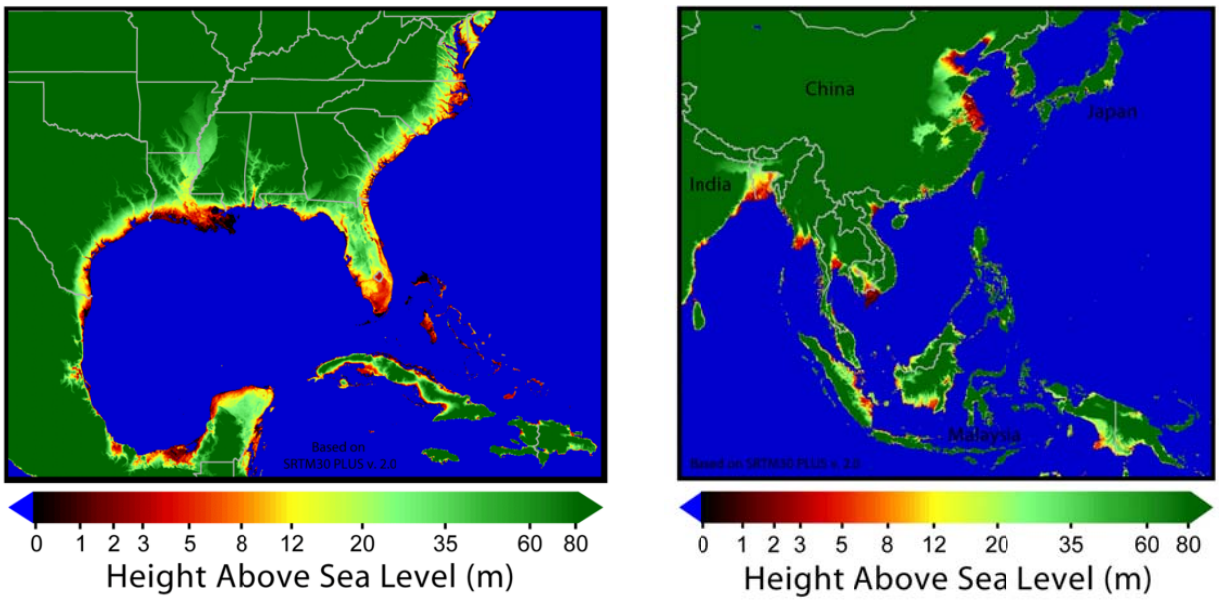

Figure 1.3: Topographic maps of the southeast United States and Southeast Asia highlighting regions near sea level that could be potentially vulnerable to sea level rise. http://www.globalwarmingart.com/wiki/File:Global_Sea_Level_Rise_Risks_png

less important, it could mean that continental ice sheets on Greenland and Antarctica are more sensitive to temperature than previously thought [*McKay et al.*, 2011].

The consequences of even 1-3 m of sea level rise could be disastrous across the globe. Figure 1.3 illustrates how the southeast United States and Southeast Asia would be affected by rising sea level. Notice that if sea level were to rise by 3 m, large areas of Florida, Louisiana, Bangladesh, China and many other areas would be inundated. The construction of sea walls or relocation of all people and industries residing in affected areas would take an enormous human and economic toll, and result in the loss of homes and livelihood for many.

Climate change will also lead to changes in global rainfall patterns, intensifying both droughts and floods across the globe. The Clausius-Clapeyron equation dictates that the saturation vapor pressure of water increases nearly exponentially with temperature. Therefore, a warmer atmosphere will allow for more evaporation of water and an intensification of the hydrologic cycle, leading to increases in rainfall in some regions and decreases in others. At the

present, rainfall has increased in the mid- and high-latitudes and in the tropics, while it has decreased in the sub-tropics. If global average temperature increases by 2 ^{o}C, dry-season precipitation in northern Africa, southern Europe, and western Australia is projected to decrease by ~20%, and that in the southwestern United States, eastern South America, and southern Africa to decrease by ~10%, which will have a profound impact on crop productivity and water resources. For comparison, the American "dust bowl" in the 1930s was the result of a ~10% decrease in rainfall over a decade. A reduction in mountain snow pack and glaciers will also exacerbate stresses on water resources. Climate change is also predicted to increase the frequency and magnitude of extreme weather events such as hurricanes, heat waves, heavy precipitation events, and flooding. Additionally, if global average temperature increases by 1.5-2.5 ^{o}C, approximately 20-30% of plant and animal species will be at risk of extinction. As in the case of rising sea level, these consequences of climate change are irreversible on a 1,000-year timescale because temperature increases caused by elevated CO_2 are expected to persist for that time period even if carbon emissions are fully curtailed [*Solomon et al*., 2009; *IPCC*, 2007].

1.1.4 Climate Feedbacks

While basic physics dictates that increasing carbon dioxide will increase temperatures at the Earth's surface, the extent of future warming is highly sensitive to the impact of climate feedbacks, many of which are not well understood. A climate feedback is a change in the climate system induced by increasing greenhouse gases which acts to either amplify or dampen the resultant warming. A change in atmospheric water vapor concentrations is the largest feedback affecting climate sensitivity. Water vapor is a strong greenhouse gas, and its concentration in the troposphere is expected to increase with rising surface temperatures,

amplifying the observed warming. Changes in stratospheric water vapor and their resultant feedbacks are more uncertain, which will be discussed in greater detail in Section 1.2.3. Cloud radiative feedbacks are the largest source of uncertainty in current climate models, as they both reflect incoming solar radiation and absorb outgoing longwave radiation. Surface warming is expected to change the distribution and types of clouds, but how this will affect their net climate feedback is poorly understood [*IPCC*, 2007]. Other climate feedbacks include the ice-albedo feedback, in which loss of ice or snow cover exposes darker-colored land or water which absorbs more short-wave radiation, amplifying climate warming. In addition, melting of high latitude permafrost may release large quantities of methane, in another important feedback that could significantly increase warming. As a whole, feedbacks complicate determination of the Earth's sensitivity to increasing greenhouse gas concentrations, and must be better understood to reduce uncertainty in future climate predictions.

Over the last 40 years, global population has increased by 80%, per capita wealth has increased 9-fold, and global energy consumption has more than doubled. These trends are predicted to continue into the future, with the majority of the world's energy obtained from the combustion of fossil fuels that release carbon dioxide into the atmosphere. Although this explosion in global population and wealth was made possible by harnessing fossil fuels as energy, the exploitation of these resources has the potential to alter the planet in ways unprecedented in the scope of human history. For the first time, humans are a dominant force in the Earth system, and we must understand and respect this power as we work towards a sustainable future.

1.2 Upper Tropospheric and Lower Stratospheric Water Vapor

In this section we focus on the impacts of upper tropospheric and lower stratospheric water vapor on climate and human health, and how these feedbacks may change in a warming climate. In order to understand how water vapor at these levels will respond to climate change, we explore the complex processes that control the amount of water entering the stratosphere. We also examine the state of water vapor measurements and their capacity to provide the continuous and accurate record necessary to address these important questions.

1.2.1 The Impact of Water Vapor on Stratospheric Ozone

Ozone is produced in the stratosphere from the photolysis of molecular oxygen by ultraviolet radiation, producing an ozone layer which peaks at 20-25 km and shields the Earth's surface from harmful UV radiation. When UV radiation is absorbed by living organisms, it damages DNA at the molecular level, which can lead to skin cancer, and damage crops and ecosystems. Skin cancer is the only cancer today with an increasing rate of occurrence, with 750,000 new cases of basal cell carcinoma and 8,000 new cases of malignant melanoma reported each year in the United States [*National Cancer Institute*, 2011]. It is therefore crucial to understand the processes that affect stratospheric ozone levels in order to predict future UV dosage in the context of a warming climate.

Complete loss of the ozone layer over Antarctica in the spring was first reported by *Farman et al.* [1985]. This ozone destruction is primarily the result of anthropogenic emissions of chlorofluorocarbons (CFCs) and other halogenated compounds which are photolyzed in the stratosphere to produce radicals that catalytically destroy ozone. During the cold polar winter, chlorine reservoir species undergo heterogeneous reactions on the surface of cold sulfate-water

aerosols and polar stratospheric clouds (PSCs) to generate reactive compounds, which quickly photolyze upon the return of sunlight in the spring to produce chlorine monoxide radicals. Chlorine and bromine monoxide destroy ozone in catalytic cycles which can destroy up to 100,000 ozone molecules per chlorine atom. Similar though less severe ozone loss has been observed over the Arctic in the spring, and ozone has declined by as much as 5-10% per decade at midlatitudes [*Logan et al.*, 1999].

In response to this observed ozone depletion, many chlorine- and bromine containing halocarbons were banned under the 1987 Montreal Protocol and its subsequent amendments. CFC concentrations have since been observed to decline, but because many of the compounds have lifetimes on the order of 50-100 yrs, effective global chlorine remains at 85% of its peak levels [*Alexander and Fairbridge*, 1999; *Mäder et al.*, 2010]. Halons, methyl bromide, and hydrochlorofluorocarbons (HCFCs) also continue to be emitted, although they are being phased out under the Montreal Protocol, contributing to stratospheric halogen concentrations. In addition, N_2O emissions are a source of ozone-destroying NO_x radicals in the stratosphere, and are currently the most important ozone-depleting anthropogenic emission [*Ravishankara*, 2009]. Thus, stratospheric concentrations of ozone-depleting substances will remain elevated for several decades due to the long lifetimes of CFCs emitted in the past, continuing emissions of some CFC replacements and bromine compounds, as well as currently unregulated N_2O emissions.

Increased climate forcing poses an additional threat to the ozone layer through changing stratospheric temperatures and water vapor concentrations. While increasing greenhouse gas levels warm the Earth's surface, conservation of energy dictates that they produce cooling in the stratosphere. At 35 km, mean stratospheric temperatures have decreased by ~0.75 K/decade since 1979, while at 50 km they have decreased by 2.5 K/decade [*Thompson and Solomon*,

2005]. The frequency and persistence of PSCs and sulfate aerosols capable of halogen activation is strongly dependant on temperature. Colder stratospheric temperatures increase the surface area for halogen activation and subsequently the catalytic polar ozone destruction by chlorine and bromine radicals. Observations over the last 20 years show that ozone loss in the Arctic spring is highly correlated with temperature. The Arctic ozone loss in the winter-spring of 2011 provides a particularly striking example of this connection, when extremely cold temperatures led to 80% ozone loss from 18-20 km compared to January levels. Vortex temperatures in March, 2011, were ~3 ^{o}C colder than March 1997, both unusually cold years, but 2011 showed twice as much ozone loss as 1997 [*Manney et al*., 2011]. Thus, even a few degrees of cooling near the threshold temperature for sulfate aerosol activation can significantly increase stratospheric ozone destruction. Decreasing stratospheric temperatures are therefore predicted to delay the recovery of ozone by approximately a decade [*WMO*, 2003].

Climate forcing from increasing greenhouse gases also has the potential to increase stratospheric water vapor levels which could enhance ozone destruction through several mechanisms. Water vapor is a source of HO_x radicals in the stratosphere, which catalytically destroy ozone. At the poles, elevated water vapor also increases the formation and persistence of PSCs; a 1 ppmv increase in water vapor increases the threshold temperature for PSC activation by ~1 ^{o}C, which would increase the spatial and temporal extent of polar ozone loss [*Kirk-Davidoff et al*., 1999]. Elevated water vapor also increases activation of sulfate-water aerosols for ozone depletion, both at the poles and at midlatitudes. Deep convective outflow has been observed to produce plumes with up to 12 ppmv of water vapor in the midlatitude stratosphere, which could potentially activate halogen-catalyzed ozone loss on sulfate-water aerosols, leading to destruction of up to 25% of local ozone over 7 days [*Anderson et al*., 2012]. Deep convection

can also transport very short-lived bromine and iodine species into the stratosphere on short timescales, which would amplify this ozone destruction. If increasing global surface temperatures lead to a greater frequency of such deep convective events, substantial local ozone destruction could be observed in the summer over populated areas. Increases in both mean stratospheric water vapor and local high water vapor plumes therefore present a continuing threat to the global ozone layer.

Furthermore, preliminary talk of injecting aerosols into the stratosphere as a way of combating climate forcing makes a thorough understanding of ozone chemistry crucial. Studies following the eruption of Mt. Pinatubo in 1991 showed that high concentrations of such aerosols lead to significant ozone destruction, particularly when combined with the effect of man-made halogenated compounds [*Tilmes et al*., 2008]. Before we can consider such large-scale geoengineering it is essential to understand the effect it would have on the ozone layer in combination with the stresses described above.

While global ozone concentrations appear to be recovering from their lowest levels associated with past halogen emissions, threats to ozone from a changing climate and potentially from geoengineering make predicting future levels particularly important. Though warmer climates have occurred previously in the Earth's history, ozone has never before been threatened by the current combination of high carbon dioxide and man-made halogenated compounds. In particular, future changes in stratospheric water vapor due to a warming climate remain a large source of uncertainty in the prediction of future ozone levels and surface UV dosage.

1.2.2 Radiative Impact of Water Vapor

Water vapor is the dominant atmospheric greenhouse gas, and because the amount of water vapor which can be held by the atmosphere increases strongly with temperature, it is very sensitive to changes in climate. The inclusion of water vapor and other climate feedbacks within general circulation models (GCMs) produces ~3 ^{o}C of warming for a doubling of CO_2 from preindustrial times, compared to 1.2 ^{o}C of warming calculated without feedbacks [*IPCC*, 2007]. Longwave radiation at the wavelengths of water absorption is fully attenuated in the lower troposphere, such that increasing water vapor concentrations at those levels will have no impact on radiative forcing. However, surface temperatures are very sensitive to changes in water vapor in the upper troposphere and lower stratosphere, where water vapor absorption lines are unsaturated. The climate feedbacks of upper tropospheric water vapor are well represented in climate models because water vapor at these levels closely follows temperature changes. Increasing upper tropospheric temperatures are predicted to increase water vapor concentrations in a positive climate feedback. On the other hand, the processes that control water vapor in the stratosphere are not well understood, which makes predictions of stratospheric water vapor levels and their radiative feedbacks much more uncertain.

One important tool in predicting stratospheric water vapor levels is to look for trends in past observations. However, past trends are unclear and show different signs over different periods of time, making extrapolation to the future very difficult. Stratospheric water vapor has been measured nearly continuously from 1964 to the present via balloon-borne frostpoint hygrometers, and from 1991 to the present from several satellite platforms. At altitudes from 14 to 25 km (380-640 K potential temperature) from 1981-2006, frostpoint hygrometer measurements show positive trends ranging from +0.3 to +0.7%/yr at various altitudes. HALOE

satellite data from 1991-2005 show globally averaged trends of -1.1 to -0.1%/yr [*Scherer et al*., 2008]. However, a clear increase in water vapor was observed in HALOE data from 20-25 km in the tropics from 1991-2001, which was not discernible elsewhere. There is more robust evidence of a ~10% drop in water vapor concentrations from 2001 to 2004, which was observed with the frostpoint hygrometer and the HALOE and SAGE II satellite instruments. This pronounced decrease in water vapor was observed beginning in 2001 in the lower tropical stratosphere, and then observed 6-18 months later at midlatitudes, and 12-18 months later in the middle stratosphere (25-35 km), consistent with the expected stratospheric transport times. Water vapor concentrations continued to decrease until 2004; since that time they have remained constant at some levels and increased at others, with significant increases in the tropical lower stratosphere returning values to those observed prior to 2002 [*Jones et al*., 2009]. Overall, stratospheric water vapor concentrations over the period of observations have shown significant variations with time, but observed trends provide no clear evidence of how water will evolve in the future.

What is clear is that changes in water vapor concentration of the magnitude that have been observed in the past have important radiative implications. *Solomon et al*. [2010] determined that a 1 ppmv increase (~1% per year) in stratospheric water vapor between 1980 and 2000, though uncertain, would have enhanced the rate of surface warming over that period by ~30% compared to estimates without this change. The 0.4 ppmv decrease in water vapor after 2001 acted to reduce the rate of global surface warming from 2000-2009 by ~25%. The combination of these trends likely contributed to the observed flattening of the global surface warming trend observed in the past decade. It is clear that although water vapor in the stratosphere is present at levels much lower than those in the troposphere, observed changes in

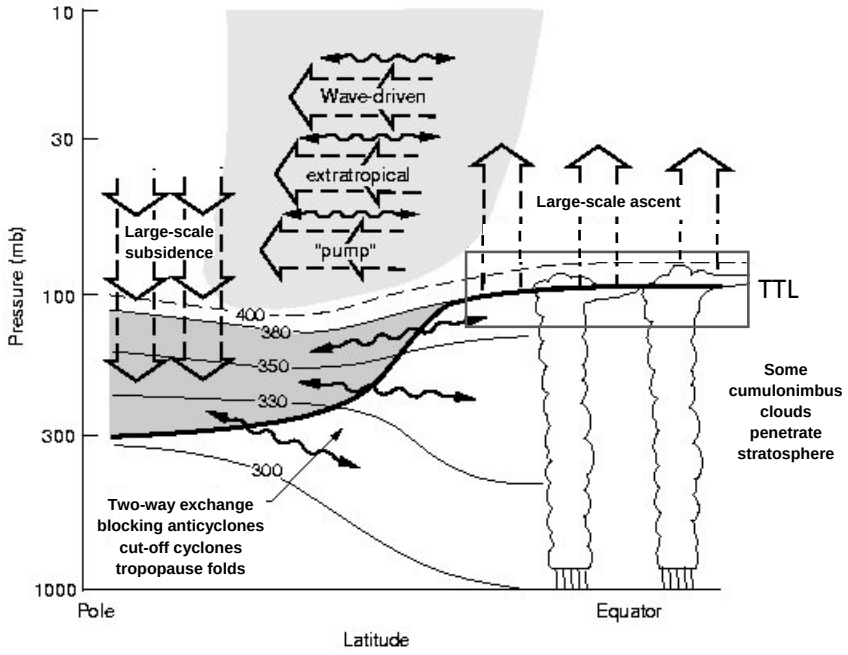

Figure 1.4: The dynamics controlling transport between the troposphere and the stratosphere. The tropopause is shown as a thick line, isentropic surfaces are shown as thin lines and labeled in Kelvin, and the TTL is indicated. The large-scale circulation is shown as broad arrows, which causes large scale ascent in the tropics and descent at the poles. The wavy double-headed arrows indicate meridional transport by eddy motions. Figure adapted from *Holton et al*. [1995].

stratospheric water vapor have a profound impact on radiative forcing and surface temperatures. It is therefore critical to better understand how stratospheric water vapor will be affected by a changing climate in order to predict future changes and their feedback on the climate system.

1.2.3 The Control of Stratospheric Humidity

The large-scale circulation of the stratosphere was first described by *Brewer* [1949] and *Dobson* [1956] in which air ascends into the stratosphere in the tropics, is transported upward and poleward in the stratosphere, and then descends back to the troposphere at higher latitudes. This circulation, which is shown in Figure 1.4, is driven by atmospheric wave-breaking in the extratropical stratosphere, which draws air upwards in the tropics through angular momentum forcing in an extratropical "pump". This circulation pattern explains the observed aridity of the

stratosphere, as most air enters the stratosphere through the high, cold tropical tropopause, where stratospheric water vapor levels are set by the saturation mixing ratio at the coldest temperatures encountered by the air parcel. In fact, the cold temperatures of the tropical tropopause produce stratospheric water vapor concentrations that are well below the saturation mixing ratios at temperatures along the extratropical tropopause.

The processes operating near the tropical tropopause are therefore extremely important to the control of water vapor concentrations in the global stratosphere. The tropical tropopause is in fact unique because it is not a sharp boundary, but rather a transition zone between purely tropospheric air and purely stratospheric air. This region is called the tropical tropopause layer (TTL), and shows both convective activity characteristic of the troposphere, and gradients in chemical tracers characteristic of the stratosphere; it is indicated in Figure 1.4. The bottom of the TTL is defined as the level of main convective outflow at ~355 K (150 hPa, 14 km); below this level, air is radiatively cooled and typical motion is subsidence, with ascent occurring predominantly by moist convection. Above that level, air is radiatively heated producing slow upward motion into the stratosphere. Deep convection does occasionally penetrate into the TTL, with the upper boundary of the region defined as the highest level at which convection has been observed, ~425 K (70 hPa, 18.5 km). The cold point tropopause is located within the layer at ~380 K (100 hPa, 16.5 km). The TTL is bounded laterally by the subtropical jets at ~30^{o} latitude, although these boundaries are somewhat permeable, with some isentropic transport in both directions between the TTL and midlatitude lowermost stratosphere [*Folkins et al*., 1999; *Gettelman and Forster*, 2002].

Water vapor is transported to the lower TTL by rapid tropospheric convection, in which the air is dehydrated to several tens of ppmv by condensation and precipitation. Within the TTL,

air parcels experience cooling as they are slowly transported upward. When water vapor concentrations exceed the local ice saturation mixing ratio (SMRi), excess water vapor condenses to form ice crystals and sediments out, dehydrating the parcel to the SMRi at the coldest temperature encountered on its trajectory. This process dehydrates the air parcels to ~3.5-4 ppmv, which is typically observed in air that has recently entered the lower stratosphere. The coldest temperature encountered by an air parcel is often the cold point tropopause where it enters the stratosphere, but it may be located remotely from that location due to longitudinal differences in TTL temperature. While vertical velocities in the TTL are on the order of 0.5 mm/s, horizontal velocities are typically ~5 m/s, allowing air parcels to travel large horizontal distances around the globe before ascending into the stratosphere. In regions of high convective activity, such as the Western Tropical Pacific, TTL temperatures can be significantly lower than average, allowing air parcels which travel through these regions to be dehydrated to levels lower than the SMRi where they cross into the stratosphere [*Holton and Gettelman*, 2001].

This concept of thermal control of water vapor entering the stratosphere is supported by the observed "tape recorder" of seasonal water vapor concentrations, in which seasonal cycles in tropical tropopause temperatures are strongly correlated with lower stratospheric water vapor concentrations [*Mote et al*., 1996]. In fact, models only considering slow ascent and dehydration to the lowest SMRi encountered on an air parcel's trajectory reproduce stratospheric water vapor concentrations well [*Feugistaler et al*., 2005]. However, the positive trend in stratospheric water vapor which was observed from 1980-2000 (see section 1.2.2) during a period with a negative trend in tropical tropopause temperatures of ~0.5 K/decade [*Zhou et al*., 2001; *Seidel and Randel*, 2006] challenges the validity of strict thermal control, though both trends are associated with large uncertainties [*Wang et al*., 2012; *Scherer et al*., 2008]. In addition, frequent

observations of supersaturation in the TTL, particularly near the tropopause, complicate the picture of rapid condensation to the SMRi.

Also complicating the picture of thermal control of stratospheric water vapor is the impact of deep convection in delivering both dehydrated and hydrated air into the TTL and lower stratosphere. Observations of elevated HDO in the TTL indicate that the significant evaporation of convectively injected ice particles takes place, demonstrating that convective processes, in addition to slow ascent with condensation and precipitation of ice, are very important in the region [*Dessler et al*., 2007]. Air detraining from deep overshooting convection is colder than ambient air, producing low water vapor concentrations in convective outflow. Cold convective outflow can also mix with ambient air in the TTL to produce cold pools that dehydrate air transported through the area. On the other hand, convection can also deposit ice crystals into unsaturated air which then evaporate and hydrate the parcel. This hydration can occur in unsaturated air downstream of a cold trap region in the lower TTL, or above the tropopause where air is always unsaturated due to the increasing temperature profile. In particular, ice deposited by convection penetrating above the tropopause has the potential to directly hydrate the stratosphere while bypassing the temperature control of the cold tropical tropopause. That added water is then transported upward and poleward by the residual circulation, irreversibly hydrating the stratosphere. Evidence of such convection has been repeatedly observed as high as 425 K via measurements of ice particles, elevated water vapor plumes, and cloud brightness temperatures [*Khaykin et al*., 2009; *de Reus et al*., 2009]. Convection penetrating the tropopause is important at midlatitudes as well, where warmer tropopause temperatures allow convection to transport both ice and water vapor in excess of local stratospheric concentrations. Such deep convection has been shown to contribute significantly to the stratospheric water vapor budget,

enhancing water vapor at 380 K in the midlatitudes by ~40% [*Dessler and Sherwood*, 2004; *Hanisco et al.*, 2007].

In order to predict how stratospheric water vapor concentrations may change in the future, it is not necessarily the process that control stratospheric water as a whole, but how those processes may *change*, which is significant. Though the tropics set the entry level for water vapor in the stratosphere, processes operating both in the tropics and at midlatitudes have the potential to change in ways that alter stratospheric humidity. Therefore, it is important to examine processes which may change tropical tropopause temperatures and associated thermal control of water vapor, tropical convection in the TTL both below and above the tropopause, and midlatitude convection above the tropopause.

Cold point tropopause temperatures are influenced by several factors which may develop differently as greenhouse gas concentrations increase. Observations of tropical tropopause temperatures show that they decreased by ~0.5 K/decade from 1980-2006 [*Zhou et al.*, 2001; *Seidel and Randel*, 2006], but several studies suggest that this trend may not continue. To first order, warming in the troposphere tends to shift the atmospheric temperature profile towards a warmer, higher tropopause, while stratospheric cooling tends to shift the tropopause colder and higher. Together these effects indicate increasing tropopause height, which has been observed, but an uncertain effect on tropopause temperature. Using a coupled chemistry-climate model, *Austin et al*. [2008] found that though surface warming only would have warmed the tropical tropopause by 0.1 K in the past, future tropospheric warming will outweigh stratospheric cooling to increase tropopause temperatures by ~1.2 K by 2100. Tropopause temperatures are also sensitive to ozone concentrations both due to direct absorption of shortwave radiation by ozone in the TTL and release of downwelling longwave radiation by ozone above in the stratosphere.

Austin et al. [2008] posit that past decreases in tropopause temperature were the result of ozone loss, but that removal of stratospheric chlorine may lead to increasing ozone in the future, increasing tropical tropopause temperatures and therefore stratospheric water vapor.

Another key factor determining tropical tropopause temperatures is the strength of the Brewer-Dobson circulation (BDC), which determines the strength of tropical upwelling and associated cooling at the tropical tropopause. Climate change increases the temperature gradient in the UT/LS, influencing the thermal wind balance and increasing the planetary wave activity at midlatitudes which drives the BDC; nearly all general circulation models therefore predict a strengthening of the BDC in a warmer climate [*Butchart et al*., 2006; *Li et al*., 2007]. Observed out-of-phase correlations between tropical and polar lower stratospheric temperature trends suggest that the BDC may be involved in past tropopause cooling trends [*Fu et al*., 2010]. In addition, *Dhomse et al*. [2008] observed increased planetary wave activity from 2000-2005, which correlates well with the decrease in tropical tropopause temperatures and water vapor over that time period. *Butchart et al*. [2006] predict based on several middle atmosphere GCMs that the increase in upwelling observed over the last decades will continue into the future at the same rate. However, as the BDC strength is related to the UT/LS temperature gradient, past increases in strength may be the partially related to ozone depletion, which also increases the temperature gradient. Using a coupled chemistry-climate model, *Li et al.* [2007] attribute ~60% of past increases in upwelling to ozone loss, suggesting that while upwelling may continue to increase, if ozone concentrations stabilize, its future trend will be smaller than that of the past decades. Additionally, tracer observations have thus far not shown evidence of a trend in stratospheric age of air, which is related to BDC strength [*Engel et al*., 2009]. However, if the strength of the

BDC does increase in the future, it would lead to colder tropical tropopause temperatures and therefore decreased water vapor entering the stratosphere.

The long-term impact of convection on stratospheric water vapor is also a large source of uncertainty. It is unclear whether deep convection will increase in the future, and if increasing convection would lead to enhanced water vapor through convective ice lofting above the tropopause or decreased water vapor through convective cooling and dehydration at and below the tropopause. We will look separately at tropical and midlatitude convection, as they are controlled by different factors and impact water vapor differently. In the tropics, increasing SSTs in a warmer climate may increase the frequency of convection capable of penetrating into the TTL and above the tropopause. *Solomon et al*. [2005] used ozonesonde data from 1980 to the present to demonstrate that ozone-depleted air parcels in the lower TTL, which are indicative of convective injection, have increased in frequency over that time period. *Gettelman et al.* [2002] have also found that convective available potential energy (CAPE), as calculated from tropical radiosonde data, has shown a positive trend since the mid-1970s. On the other hand, *Johnson and Xie* [2010] and *Austin et al.* [2008] argue that while warmer SSTs allow for more convective activation in the tropics on short timescales, on long timescales the tropospheric temperature profile will adjust such that the activation temperature for deep convection increases with SST, producing no significant change in convection in a warmer climate.

If convection does increase in a warmer climate, increased convection above the tropical tropopause could significantly moisten the stratosphere through the evaporation of injected ice particles. On the other hand, increases in cold convective outflow could cool the TTL and tropopause, leading to greater dehydration of ascending air parcels. The balance of these two effects will dictate the net impact of a potential increase in convection on stratospheric water

vapor. *Rosenlof and Reid* [2008] suggest that increasing convective cooling of the tropopause was a key factor leading to the cooling trend which began in 2000, and note that an anticorrelation between warming sea surface temperatures (SSTs) and decreasing tropopause temperatures emerged from 2000 to 2006. They suggest that continuing increases in tropical SST will lead to stronger convection and increased convective cooling of the tropopause, decreasing stratospheric water vapor in the future.

Increased climate forcing by greenhouse gases is also predicted to increase continental convective activity at midlatitudes. In particular, climate models show that increased atmospheric moisture content in a warmer climate leads to an increase in the frequency and intensity of severe storms over the United States [*Trap et al*., 2009; *Van Klooster and Roebber*, 2009]. Such changes could increase the amount of ice transported into the stratosphere by convection, increasing water vapor in both the lowermost stratosphere and overworld. Because the lowermost stratosphere is a region of descent, increases in water vapor there would have an important local radiative impact, but would not impact the global stratosphere. However, elevated water vapor above the 380 K isentrope could be isentropically transported into the tropics where it would enter the mean circulation and moisten the overworld stratosphere while bypassing the cold point [*Dessler and Sherwood*, 2004].

Overall, increasing tropospheric temperatures, changes in stratospheric ozone concentrations, changes in the Brewer-Dobson circulation, and increasing deep convection in the tropics or midlatitudes may all impact stratospheric water vapor concentrations in the future; predicting future climate feedbacks requires an improved understanding of each of these processes and their relative importance in setting stratospheric water vapor levels.

1.2.4 The State of UT/LS Water Vapor Measurements

Accurate and precise water vapor measurements are essential to understanding the mechanisms which control stratospheric humidity and to detecting short and long-term trends in stratospheric water vapor. Many techniques have been used to measure water vapor in the UT/LS, including balloon-borne and aircraft-borne in situ instruments and satellite-borne remote sensors. The 2000 SPARC Assessment of water vapor in the UT/LS [*Kley et al*., 2000] compared 15 different in situ and remote instruments and found 30-50% differences in water vapor measurements from 60-100 hPa. According to the report, the Harvard Lyman-α photofragment fluorescence hygrometer (HWV) and JPL tunable diode Laser Hygrometer (JLH) measured the highest water vapor concentrations, while the Microwave Limb Sounder (MLS) on the Aura satellite, Halogen Occultation Experiment (HALOE) on the Upper Atmosphere Research Satellite, and Stratospheric Aerosol and Gas Experiment II (SAGE II) on the Earth Radiation Budget Satellite measured the lowest values.

Since the publication of that report, water vapor measurements continued to show such discrepancies over a series of flight campaigns, including the Aura Validation Experiment–Water Isotope Intercomparison Flights (AVE-WIIF) in 2005, the Costa Rica Aura Validation Experiment (CR-AVE) in 2006, and the Tropical Composition, Cloud and Climate Coupling (TC4) in 2007. During the AVE-WIIF campaign, water vapor measurements aboard the WB-57 aircraft from HWV [*Weinstock et al*., 1994], the related Harvard Total Water Lyman-α instrument (HTW) [*Weinstock et al*., 2006], the Integrated Cavity Output Spectrometer (ICOS) water vapor isotope instrument [*Sayres et al*., 2009], the Hoxotope water isotope instrument [*St. Claire et al*., 2008], and the Aircraft Laser Infrared Absorption Spectrometer (ALIAS) [*Webster et al.,* 1994] all agreed to within 5-10%. However, this suite of in situ instruments measured 1.5-

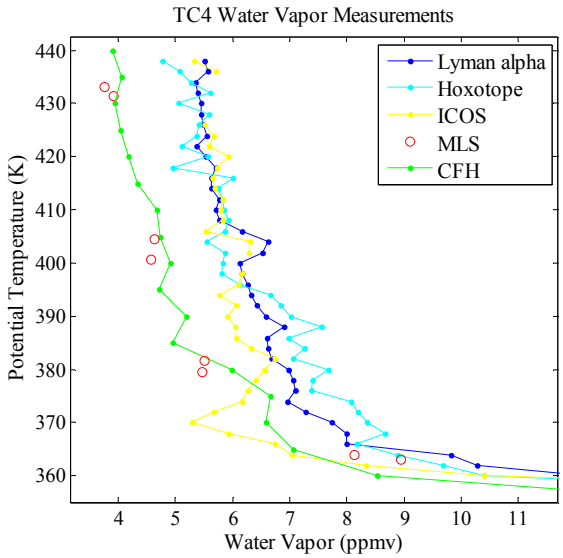

Figure 1.5: Water vapor measurements during the TC4 campaign in 2007. Shown are data from in situ aircraft instruments Lyman-α, Hoxotope, and ICOS, the MLS satellite instrument, and the CFH balloon-borne frostpoint hygrometer.

2 ppmv (30-50%) higher than the MLS satellite instrument [*Read et al.*, 2007]. During both the CR-AVE and TC4 campaigns, HWV again agreed well with ICOS and Hoxotope, but measured 1-2 ppmv higher than both MLS and the balloon-borne NOAA Cryogenic Frostpoint Hygrometer (CFH) [*Vömel et al.*, 2007] which was deployed near the aircraft flight track (Figure 1.5).

While this suite of instruments showed disagreements of 1-2 ppmv in the UT/LS over the past 10 years, a laboratory comparison of the CFH frostpoint hygrometer, JLH, and HWV showed that they agree to within 0.3 ppmv under controlled laboratory conditions [*Weinstock et al.*, 2009]. This indicates that measurement discrepancies are likely due to differences between the in-flight sampling environments of the instruments rather than calibration differences or intrinsic faults in one measurement technique. It also demonstrates that in order to resolve these measurement differences, each instrument must validate its accuracy not only in the laboratory, but under field conditions.

Recall that from 1991-2005, CFH measurements from Boulder, CO, showed an increasing trend in water vapor of ~0.7%/yr, or a 0.4 ppmv increase, while HALOE satellite data

showed a small negative trend. These trends are well within the uncertainty in the suite of water vapor measurements outlined above, demonstrating that the disparities in these measurements greatly impede our ability to establish trends in water vapor over time. The disagreement among water vapor measurements also hinders our ability to assess the mechanisms controlling stratospheric humidity because model validation is highly dependent on the chosen dataset. For example, HALOE and CFH data support models which dehydrate air to the saturation mixing ratio of the cold Western Pacific, while HWV data supports dehydration to local tropopause temperatures [*Weinstock et al*., 2009]. In addition, the water vapor dataset fails to constrain supersaturation levels near the tropopause or microphysical models of cloud/ice nucleation [*Kramer et al.*, 2009]. Improved accuracy in the water vapor community as a whole is clearly essential to predicting future stratospheric water vapor levels and their radiative impact, both through detection of trends and understanding the basic processes that control water vapor concentration.

1.3 Outline of Dissertation

In order to obtain accurate and precise water vapor measurements, it is important for each in situ instrument to thoroughly document its calibration and validation under flight conditions. To that end, we describe in Chapters 2 and 3 the operational details of the Harvard Lyman-α hygrometer and Harvard Herriott Hygrometer (HHH). In Chapter 2, we review the operation of the Lyman-α hygrometer, which measures water vapor through the photofragment fluorescence technique. We explain the components of the instrument, how the water vapor mixing ratio is determined, and its in-flight validation. We also describe the instrument's calibration in detail,

including the use of multiple reference standards and verification of the calibration accuracy at low water vapor mixing ratios.

Chapter 3 focuses on the Harvard Herriott Hygrometer, a tunable diode laser instrument which measures water vapor via infrared absorption. The instrument's optical and mechanical operation is detailed, along with its calibration and the fitting algorithm used to derive water vapor concentration from the absorption spectra. We also examine the recent flight comparison of the Lyman-α and HHH instruments with several other in situ hygrometers during the 2011 MACPEX campaign, which showed significantly better instrument agreement than past water vapor comparisons.

In Chapter 4, the importance of various transport pathways in the Tropical Tropopause Layer (TTL) is investigated using simultaneous in situ measurements of O_3, CO, CO_2, H_2O, HDO, and HCl in a simple box model. Data from the winter-time CR-AVE campaign in 2006 and the summer-time TC4 campaign in 2007 are analyzed to explore the seasonal importance of transport within the TTL via slow upward ascent, convective injection, and isentropic transport from the midlatitude stratosphere. Each of these pathways brings air into the TTL with a specific chemical signature, which is used in a one-dimensional mixing model to determine the optimal amount of transport from each pathway to best fit all measured tracer data. The model shows isentropic transport from midlatitudes to be significant in both summer and winter, significantly impacting ozone concentrations and therefore the radiative balance of the TTL. It also shows significant convective influence throughout the TTL and up to 420 K potential temperature in both seasons, which appreciably increases the amount of water vapor above the tropopause.

Finally, in Chapter 5 we revisit each of the mechanisms which may contribute to altering stratospheric water vapor concentrations in the future. By combining the conclusions of

Chapters 2, 3, and 4 with analysis from the literature, we attempt to quantify the approximate impact of each pathway on future stratospheric humidity. We also explore the continuing gaps in our understanding of these mechanisms, and propose future work aimed at resolving those outstanding questions.

References

Alexander, D. E. and R. W. Fairbridge, ed. (1999), *The Chapman & Hall Encyclopedia of Environmental Science*, pp.78-80, Kluwer Academic, Boston, MA.

Anderson, J. G., D. M. Wilmouth, J. B. Smith, and D. S. Sayres (2012), UV dosage levels in summer: Increased risk of ozone loss from convectively injected water vapor, *Science*, DOI: 10.1126.

Archer, D, M. Eby, V. Brovkin, A. Ridgwell, L. Cao, U. Mikolajewicz, K. Caldeira, K. Matsumoto, G. Munhoven, A. Montenegro, and K. Tokos (2009), Atmospheric Lifetime of Fossil Fuel Carbon Dioxide, *Annu. Rev. Earth Planet. Sci., 37*, 117–34.

Austin, J., and T. J. Reichler (2008), Long-term evolution of the cold point tropical tropopause: Simulation results and attribution analysis, *J. Geophys. Res.-Atmos.*, *113*.

Brewer, A. W. (1949), Evidence for a World Circulation Provided by the Measurements of Helium and Water Vapour Distribution in the Stratosphere, *Q J Roy Meteor Soc*, *75*(326), 351-363.

Butchart N., A. A. Scaife, M. Bourqui, J. de Grandpré, S. H. E. Hare, J. Kettleborough, U. Langematz, E. Manzini, F. Sassi, K. Shibata, D. Shindell, M. Sigmond (2006), Simulations of anthropogenic change in the strength of the Brewer–Dobson circulation, *Clim. Dyn., 27*, 727–741.

Carson, R. (1962), *Silent Spring*, p. 5, Houghton Mifflin, New York, N.Y.

de Reus, M., S. Borrmann, A. Bansemer, A. J. Heymsfield, R. Weigel, C. Schiller, V. Mitev, W. Frey, D. Kunkel1, A. Kürten, J. Curtius, N. M. Sitnikov, A. Ulanovsky, and F. Ravegnani (2009), Evidence for ice particles in the tropical stratosphere from in-situ measurements, *Atmos. Chem. Phys., 9*, 6775–6792.

Dessler, A. E., and S. C. Sherwood (2003), A model of HDO in the tropical tropopause layer, *Atmos. Chem. Phys.*, *3*, 2173-2181.

Dessler, A. E., and S. C. Sherwood (2004), Effect of convection on the summertime extratropical lower stratosphere, *J. Geophys. Res.*, *109,* D23301.

Dessler, A. E., T. F. Hanisco, and S. Fueglistaler (2007), Effects of convective ice lofting on H2O and HDO in the tropical tropopause layer*, J. Geophys. Res.*, *112*, D18309.

Dhomse, S., M. Weber, and J. Burrows (2008), The relationship between tropospheric wave forcing and tropical lower stratospheric water vapor, *Atmos. Chem. Phys., 8*, 471–480.

Dobson, G. M. B. (1956), Origin and distribution of the polyatomic molecules in the atmosphere, *Proc. R. Soc. London, Set. A, 236*, 187-193.

Drdla, K. and R Müller (2010), Temperature thresholds for polar stratospheric ozone loss, *Atmos. Chem. Phys. Discuss, 10*, 28687-28720.

Engel, A., T. Möbius, H. Bönisch, U. Schmidt, R. Heinz, I. Levin, E. Atlas, S. Aoki, T. Nakazawa, S. Sugawara, F. Moore, D. Hurst, J. Elkins, S. Schauffler, A. Andrews and K. Boering (2009), Age of stratospheric air unchanged within uncertainties over the past 30 years, *Nature Geosci., 2*, 28-31.

Farman, J. C., B. G. Gardiner, and J. D. Shanklin (1985), Large losses of total ozone in Antarctica reveal seasonal ClO_x/NO_x interaction, *Nature, 315*, 207-210.

Folkins, I., M. Loewenstein, J. Podolske, S. J. Oltmans, M. Proffitt (1999), A barrier to vertical mixing at 14 km in the tropics: Evidence from ozonesondes and aircraft measurements, *J. Geophys. Res., 104*, 22095-22102.

Fu, Q., S. Solomon, and P. Lin (2010), On the seasonal dependence of tropical lower-stratospheric temperature trends, *Atmos. Chem. Phys., 10*, 2643–2653, 2010.

Fueglistaler, S., M. Bonazzola, P. H. Haynes, and T. Peter (2005), Stratospheric water vapor predicted from the Lagrangian temperature history of air entering the stratosphere in the tropics, *J Geophys Res-Atmos*, *110*(D8).

Gettelman, A., and P. M. D. Forster (2002), A climatology of the tropical tropopause layer, J. *Meteorol. Soc. Japan, 80*, 911-924.

Gettelman, A., D. J. Seidel, M. C. Wheeler, and R. J. Ross (2002), Multidecadal trends in tropical convective available potential energy, *J. Geophys. Res*., 107, D21, 4606.

Gregory, J. G., P. Huybrechts, and S. C. B. Raper (2004), Climatology: Threatened loss of the Greenland ice-sheet, *Nature, 428*, 616.

Hanisco, T. F., E. J. Moyer, E. M. Weinstock, J. M. St. Clair, D. S. Sayres, J. B. Smith, R. Lockwood, J. G. Anderson, A. E. Dessler, F. N. Keutsch, J. R. Spackman, W. G. Read, and T. P. Bui (2007), Observations of deep convective influence on stratospheric water vapor and its isotopic composition, *Geophys Res Lett*, *34*(4).

Holton, J. R., and A. Gettelman (2001), Horizontal transport and the dehydration of the stratosphere, *Geophys. Res. Lett., 28*, 2799-2802.

Holton, J. R., P. H. Haynes, M. E. Mcintyre, A. R. Douglass, R. B. Rood, and L. Pfister (1995), Stratosphere-Troposphere Exchange, *Rev Geophys*, *33*(4), 403-439.

IPCC (2007), *Climate Change 2007, Fourth Assessment Report: Synthesis Report,* http://www.ipcc.ch/publications_and_data/ar4/syr/en/contents.html.

Johnson, N., and S.-P. Xie (2010), Changes in the sea surface temperature threshold for tropical convection, *Nature Geoscience, 3*, 842-845.

Jones, A., J. Urban, D. P. Murtagh, P. Eriksson, S. Brohede, C. Haley, D. Degenstein, A. Bourassa, C. von Savigny, T. Sonkaew, A. Rozanov, H. Bovensmann, and J. Burrows (2009), Evolution of stratospheric ozone and water vapour time series studied with satellite measurements, *Atmos. Chem. Phys., 9*, 6055–6075.

Khaykin, S., J.-P. Pommereau, L. Korshunov, V. Yushkov, J. Nielsen, N. Larsen, T. Christensen, A. Garnier, A. Lukyanov, and E.Williams (2009), Hydration of the lower stratosphere by ice crystal geysers over land convective systems, *Atmos. Chem. Phys., 9*, 2275–2287.

Kirk-Davidoff, D. B., E. J. Hintsa, J. G. Anderson, and D. W. Keith (1999), The effect of climate change on ozone depletion through changes in stratospheric water vapour, *Nature*, *402*(6760), 399-401.

Kley, D., J. M. Russell III, and C. Phillips (Eds.) (2000), *SPARC Assessment of Upper Tropospheric and Stratospheric Water Vapour*, World Clim. Res. Prog., Geneva, Switzerland.

Kramer, M., et al. (2009), Ice supersaturations and cirrus cloud crystal numbers, *Atmos Chem Phys*, *9*(11), 3505-3522.

Kurczy, S. (2010), China to mold future world energy use: IEA, in *The Christian Science Monitor*, edited, The Christian Science Monitor.

Lewis, N. S., and D. G. Nocera (2006), Powering the planet: Chemical challenges in solar energy utilization, *P Natl Acad Sci USA*, *103*(43), 15729-15735.

Li, F., J. Austin, and J. Wilson (2007), The Strength of the Brewer–Dobson Circulation in a Changing Climate: Coupled Chemistry–Climate Model Simulations, *J. Climate, 21*, 40-57.

Logan, J. A., I. A. Megretskaia, A. J. Miller, G. C. Tiao, D. Choi, L. Zhang, R. S. Stolarski, G. J. Labow, S. M. Hollandsworth, G. E. Bodeker, H. Claude, D. De Muer, J. B. Kerr, D. W. Tarasick, S. J. Oltmans, B. Johnson, F. Schmidlin, J. Staehelin, P. Viatte, and O. Uchino (1999), Trends in the vertical distribution of ozone: A comparison of two analyses of ozonesonde data, *J. Geophys. Res., 104*, 26373-26399.

Mäder, J. A., J. Staehelin, T. Peter, D. Brunner, H. E. Rieder, and W. A. Stahel (2010), Evidence for the effectiveness of the Montreal Protocol to protect the ozone layer, *Atmos. Chem. Phys., 10*, 12161–12171.

Manney, G. L., M. L. Santee, M. Rex, N. J. Livesey, M. C. Pitts, P. Veefkind, E. R. Nash, I. Wohltmann, R. Lehmann, L. Froidevaux, L. R. Poole, M. R. Schoeberl, D. P. Haffner, J. Davies, V. Dorokhov, H. Gernandt, B. Johnson, R. Kivi, E. Kyro, N. Larsen, P. F. Levelt, A. Makshtas, C. T. McElroy, H. Nakajima, M. C. Parrondo, D. W. Tarasick, P. von der Gathen, K.

A.Walker and N. S. Zinoviev (2011) Unprecedented Arctic ozone loss in 2011, *Nature, 478*, 469-475.

May, R. D. (1998), Open-path, near-infrared tunable diode laser spectrometer for atmospheric measurements of H_2O, *J. Geophys. Res., 103*, D15, 19161-19172.

McKay, N. P., J. T. Overpeck, and B. L. Otto-Bliesner (2011), The role of ocean thermal expansion in Last Interglacial sea level rise, *Geophys. Res. Lett*., 38, L14605.

Mote, P. W., K. H. Rosenlof, M. E. McIntyre, E. S. Carr, J. C. Gille, J. R. Holton, J. S. Kinnersley, H. C. Pumphrey, J. M. Russell, and J. W. Waters (1996), An atmospheric tape recorder: The imprint of tropical tropopause temperatures on stratospheric water vapor, *J Geophys Res-Atmos*, *101*(D2), 3989-4006.

National Cancer Institute (2011), *SEER Stat Fact Sheets: Melanoma of the Skin*, http://seer.cancer.gov/statfacts/html/melan.html

NOAA Earth System Research Laboratory (2012), *Mauna Loa CO2 data*, http://www.esrl.noaa.gov/gmd/ccgg/trends/#mlo_full

Ravishankara, A. R., J. S. Daniel, R. W. Portmann (2009), Nitrous Oxide (N_2O): The dominant ozone-depleting substance emitted in the 21st century, *Science, 326*, 123-125.

Read,W. G., et al. (2007), Aura microwave limb sounder upper tropospheric and lower stratospheric H2O and relative humidity with respect to ice validation, *J. Geophys. Res., 112*, D24S35, doi:10.1029/2007JD008752.

Rosenlof, K. H., and G. C. Reid (2008), Trends in the temperature and water vapor content of the tropical lower stratosphere: Sea surface connection, *J. Geophys. Res.-Atmos.*, *113*(D6).

Sayres, D., E. J. Moyer, T. F. Hanisco, J. M. St. Clair, F. N. Keutsch, A. O'Brien, N. T. Allen, L. Lapson, J. N. Demusz, M. Rivero, T. Martin, M. Greenberg, C. Tuozzolo, G. S. Engel, J. H. Kroll, J. B. Paul, and J. G. Anderson (2009), A new cavity based absorption instrument for detection of water isotopologues in the upper troposphere and lower stratosphere, *Review of Scientific Instruments, 80*, 044102.

Sayres, D. S., L. Pfister, T. F. Hanisco, E. J. Moyer, J. B. Smith, J. M. St. Clair, A. S. O'Brien, M. F. Witinski, M. Legg, and J. G. Anderson (2010), Influence of convection on the water isotopic composition of the tropical tropopause layer and tropical stratosphere, *J. Geophys. Res., 115*, D00J20, doi:10.1029/2009JD013100.

Seidel, D. J., and W. J. Randel (2006), Variability and trends in the global tropopause estimated from radiosonde data, *J Geophys Res-Atmos*, *111*(D21).

Scherer, M., H. Vomel, S. Fueglistaler, S. J. Oltmans, and J. Staehelin (2008), Trends and variability of midlatitude stratospheric water vapour deduced from the re-evaluated Boulder balloon series and HALOE, *Atmos Chem Phys*, *8*(5), 1391-1402.

Shindell, D. T. (2001), Climate and ozone response to increased stratospheric water vapor, *Geophys. Res. Lett., 28*, 1551-1554.

Solomon, S., D. W. J. Thompson, R. W. Portmann, S. J. Oltmans, and A. M. Thompson (2005), On the distribution and variability of ozone in the tropical upper troposphere: Implications for tropical deep convection and chemical-dynamical coupling, *Geophys. Res. Lett., 32*, L23813.

Solomon, S., G.-K. Plattner, R. Knutti, and P. Friedlingstein (2009), Irreversible climate change due to carbon dioxide emissions, *Proc. Natl Acad. Sci. USA.*, *106*, 1704-1709.

Solomon, S., K. H. Rosenlof, R. W. Portmann, J. S. Daniel, S. M. Davis, T. J. Sanford, and G. K. Plattner (2010), Contributions of Stratospheric Water Vapor to Decadal Changes in the Rate of Global Warming, *Science*, *327*(5970), 1219-1223.

Spiro, T., and W. Stigliani (2003), *Chemistry of the Environment*, 2nd edition ed., Prentice Hall, New Jersey.

St. Clair, J. M., T. F. Hanisco, E. M. Weinstock, E. J. Moyer, D. S. Sayres, F. N. Keutsch, J. H. Kroll, J. N. Demusz, N. T. Allen, J. B. Smith, J. R. Spackman, and J. G. Anderson (2008), A new photolysis laser-induced fluorescence instrument for the detection of H_2O and HDO in the lower stratosphere, *Review of Scientific Instruments, 79*, 064101.

Thompson, D. W. J., and S. Solomon (2005), Recent stratospheric climate trends as evidenced in radiosonde data: Global structure and tropospheric linkages, *J. Climate, 18*, 4785-4795.

Tilmes, S., R. Muller, and R. Salawitch (2008), The sensitivity of polar ozone depletion to proposed geoengineering schemes, *Science*, *320*(5880), 1201-1204.

Trapp, R. J., N. S. Diffenbaugh, and A. Gluhovsky (2009), Transient response of severe thunderstorm forcing to elevated greenhouse gas concentrations, *Geophys. Res. Lett*., 36, L01703.

United Nations Population Division, Department of Economic and Social Affairs (2011), *World Population Prospects: the 2010 Revision*, CD-ROM Edition.

Van Klooster, S. L. and P. J. Roebber (2009), Surface-Based Convective Potential in the Contiguous United States in a Business-as-Usual Future Climate, *J. Climate, 22*, 3317-3330.

Vömel, H., D. E. David, and K. Smith (2007), Accuracy of tropospheric and stratospheric water vapor measurements by the cryogenic frost point hygrometer: Instrumental details and observations, *J. Geophys. Res., 112*, D08305, doi:10.1029/2006JD007224.

Wang, J. S., D. J. Seidel, and M. Free (2012), How well do we know recent climate trends at the tropical tropopause*?, J. Geophys. Res., 117*, D09118.

Webster, C. R., R. D. May, C. A. Trimble, R. G. Chave, and J. Kendall (1994), Aircraft laser infrared absorption spectrometer (ALIAS) for in situ atmospheric measurements of HCl, N2O, CH4, NO2, and HNO3, *Appl. Opt*., 33, 454–472.

Weinstock, E. M., E. J. Hintsa, A. E. Dessler, J. F. Oliver, N. L. Hazen, J. N. Desmusz, N. T. Allen, L. B. Lapson, and J. G. Anderson (1994), New fast response photofragment fluorescence hygrometer for use on the NASA ER-2 and the Perseus remotely piloted aircraft, *Rev. Sci. Instrum., 65*, 3544–3554.

Weinstock, E. M., J. B. Smith, D. Sayres, J. R. Spackman, J. V. Pittman, N. Allen, J. Demusz, M. Greenberg, M. Rivero, L. Solomon, and J. G. Anderson (2006), Measurements of the Total Water Content of Cirrus Clouds. Part I: Instrument Details and Calibration, *J. Atmos. Ocean Technol., 23*, 1397-1409.

Weinstock, E. M., J. B. Smith, D. S. Sayres, J. V. Pittman, J. R. Spackman, E. J. Hintsa, T. F. Hanisco, E. J. Moyer, J. M. St. Clair, M. R. Sargent, and J. G. Anderson (2009), Validation of the Harvard Lyman-a in situ water vapor instrument: Implications for the mechanisms that control stratospheric water vapor, *J. Geophys. Res., 114*, D23301, doi:10.1029/2009JD012427.

The World Bank (2012), *World Bank national accounts data, and OECD National Accounts data files*, http://data.worldbank.org/topic/climate-change.

World Energy Outlook (2010), International Energy Agency, http://www.iea.org/weo/2010.asp.

WMO (2003), *Scientific Assessment of Ozone Depletion: 2002*, World Meteorological Organization, Global Ozone Research and Monitoring Project – Report No. 47, Geneva, Switzerland.

Zhou, X.-L., M. A. Geller, and M. Zhang (2001), Cooling trend of the tropical cold point tropopause temperatures and its implications, *J. Geophys. Res., 106*, 1511-1522.

Chapter 2

The Harvard Lyman-α Hygrometer

2.1 Introduction

The Harvard Lyman-α hygrometer, in various forms, has been used to measure water vapor in the upper troposphere and lower stratosphere (UT/LS) for the last twenty years. The hygrometer utilizes a technique called photofragment fluorescence, in which water vapor is photolyzed by Lyman-α (121.6 nm) radiation, and the resulting fluorescence of excited OH is detected. The instrument was originally designed for deployment on stratospheric balloons, on which it flew four flights from 1987-1989 [Schwab et al., 1990]. It was subsequently adapted for the nosecone of NASA's ER-2 aircraft, where it was deployed in several research campaigns from 1992-2000 [Weinstock et al., 1994]. The current version of the instrument, known as Harvard Water Vapor (HWV), was designed for the spearpod of NASA's WB-57 aircraft, where it has flown from 2001 to the present. In the WB-57 water vapor instrument, the previous 3 in square duct was replaced with a 2 in square duct, with the optical system essentially unchanged. In this chapter, we provide a detailed description of the Lyman-α instrument in its present form and discuss its performance during the Mid-latitude Airborne Cirrus Properties Experiment (MACPEX) in 2011.

2.2 Photo-fragment Fluorescence Detection

The Lyman-α photofragment fluorescence technique is well-suited to aircraft-based stratospheric water vapor measurements because of its molecular specificity, high signal to noise, short response time, and ability to measure water over a wide range of concentrations relevant to the UT/LS. In the technique, Lyman-α (121.6 nm) radiation generated by a radiofrequency plasma discharge lamp is used to photo-dissociate water vapor in the instrument duct:

$$\mathrm{H_2O} + h\nu(121.6\ \mathrm{nm}) \rightarrow \mathrm{OH}(A\,^2\Sigma^+) + \mathrm{H} \tag{2.1}$$

$$\mathrm{OH}(A\,^2\Sigma^+) \rightarrow \mathrm{OH}(X\,^2\Pi) + h\nu(305 - 325\ \mathrm{nm}) \tag{2.2}$$

$$\mathrm{OH}(A\,^2\Sigma^+) + \mathrm{M} \rightarrow \mathrm{OH}(X\,^2\Pi) \tag{2.3}$$

Approximately 10% of absorbed photons produce OH fragments in the first excited electronic state, $A\,^2\Sigma^+$, and ν'=1 vibrational level, which quickly relaxes to ν'=0 (Equation 2.1). The excited OH can either fluoresce (Equation 2.2) or be quenched by collisions with nitrogen or oxygen (Equation 2.3). The strongest fluorescence is from the highly excited rotational levels (N'=20-22) of the ν'=0 level of the $A\,^2\Sigma^+$ state to the ground electronic state, $X\,^2\Pi$, resulting in emission from 305-325 nm, with a fluorescence lifetime of ~10^{-6} sec.

The normalized fluorescence signal, S_{norm}, is related to the number density of water vapor by the proportionality constant C_{flr} [(counts/s)/(molecules/cm^3)], which is a function of the axis sensitivity to H_2O at zero air density, C_o, an empirically derived quenching factor, q_{air} [cm^3/molecule], and the number density of air, [M]:

$$S_{norm} = C_{flr}[\mathrm{H_2O}] = C_o\left(\frac{1}{1 + q_{air}[\mathrm{M}]}\right)[\mathrm{H_2O}] \tag{2.4}$$

C_o implicitly includes the absorption cross section of H_2O at 121.6 nm, the OH($A\,^2\Sigma^+$) quantum yield, and the collection efficiency at the detection axis. q_{air} is a product of τ, the lifetime of OH($A\,^2\Sigma^+$), and k_{qair}, the weighted sum of the quenching coefficients for N_2 and O_2: $q_{air} = \tau * k_{qair}$. At the pressures of the upper troposphere and lower stratosphere, the quenching term, q_{air}[M], is much greater than 1, meaning that Equation 2.4 reduces to:

$$S \sim \frac{C_o}{q_{air}[\mathrm{M}]}[\mathrm{H_2O}] \tag{2.5}$$

and the fluorescence signal is directly proportional to the number density of H_2O. The constants C_o and q_{air} are empirically determined in the laboratory as a function of the air density [M] by calibration to an external water vapor standard.

2.3 The Harvard Lyman-α Hygrometer

2.3.1 Detection Axis

The optical and mechanical components of the Lyman-α instrument's detection axis are shown in Figure 2.1. The vacuum UV (VUV) lamp illuminates the flow tube with 121.6 nm radiation and fluorescence is detected at a right angle to the lamp flux by a photomultiplier tube (PMT), while VUV flux is monitored by a photodiode directly across from the lamp. The region sampled by the photocathode of the PMT is indicated with a circle in the right panel.

Lamp

The excitation wavelength is generated by sealed, low pressure, radiofrequency plasma discharge lamp. The lamp body is a high-purity quartz tube which is sealed at the transmission

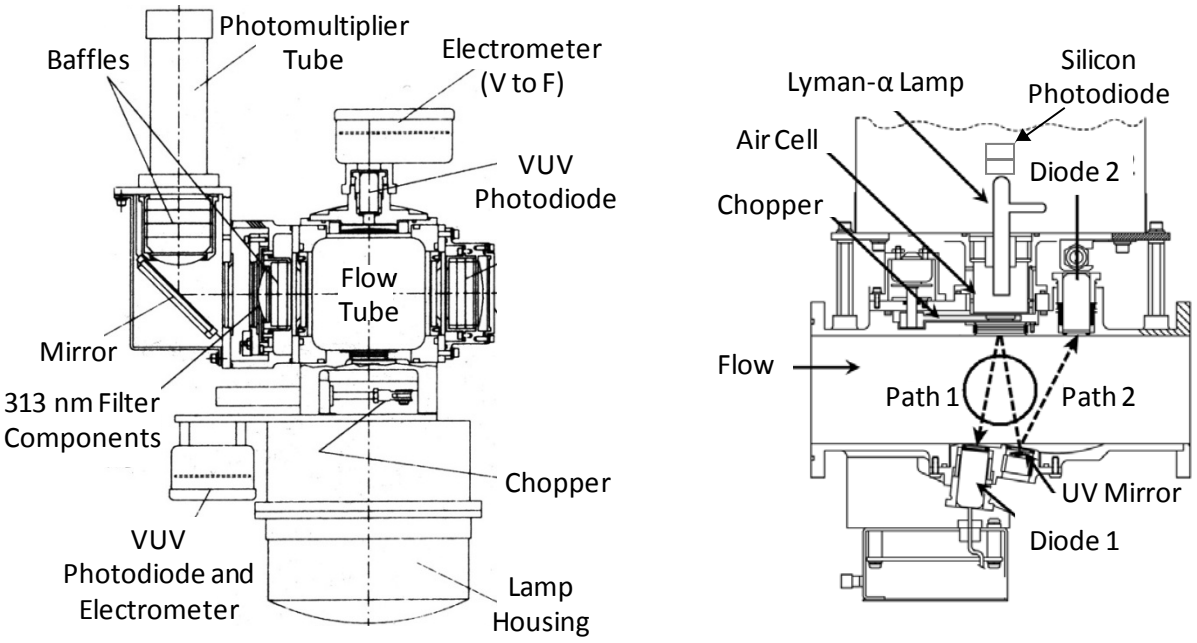

Figure 2.1: Diagram of the Lyman-α detection axis. Left: Cross section of the flow tube with the detection optics indicated. Right: Top-down view of the flow tube including optical details of the lamp module, air filter cell, and absorption measurement. In this configuration, the PMT is located above the plane of the page; the circle indicates the detection region imaged onto the PMT.

end with a MgF_2 window and filled with high-purity neon to support the discharge. A sidearm of the lamp holds uranium hydride which serves as a source of hydrogen as well as an efficient chemical getter for impurities in the lamp. The lamp maintains a small amount of H_2 in equilibrium with the hot uranium hydride, with the discharge stabilized by a feedback loop which controls the amount of heat applied to the lamp sidearm. A silicon photodiode is placed at the end of the lamp opposite from the transmission window, which selectively monitors the 486.1 nm hydrogen Balmer line through a narrow band (~1 nm) interference filter and a 10 nm bandpass filter. The diode signal is fed to a circuit which controls the heat on the uranium hydride source, in a feedback loop which maintains a stable Lyman-α output to within 1%.

Lamp Filters

The emission spectrum of the lamp from 115-150 nm is made up of >90% Lyman-α radiation at 121.6 nm, with the remaining fraction emitted by the O_2 triplet at 130.4 nm and the Lyman bands of H_2 around 150 nm. This impurity radiation, which can vary from lamp to lamp, has a different photofragment fluorescence efficiency than that of Lyman-α, and can lead to uncertainty in the measurement. O_2 serves as an excellent filter for Lyman-α radiation because it has a significant absorption cross section throughout the VUV, with a notable exception from 121.0-122.5 nm where the cross section drops by more than an order of magnitude. To take advantage of this property of O_2, a 2.5 cm flowing air cell is mounted between the end of the lamp and the instrument duct; a stainless-steel flow-reducing frit is used to flow air through the cell at a pressure ~1 atm above ambient. Continual flow is important to prevent the buildup of ozone in the cell, which is a significant absorber of Lyman-α. The air cell eliminates essentially all VUV radiation at wavelengths other than Lyman-α to produce a monochromatic light source.

In addition to the VUV impurities, the lamp emits a small fraction of its radiation in the near UV, within the range of the PMT collection optics at 305-325 nm. To eliminate this radiation, a Lyman-α filter is used as the window between the flowing air cell and the sampling duct of the instrument. The filter was added to the instrument in 2008, and was used during the NOVICE and MACPEX campaigns; prior to that time a MgF_2 window was used, which is transparent in the UV. The filter minimizes transmission of light outside of its bandpass from 106.6-136.6 nm (full-width half-maximum), removing >95% of the near-UV lamp output. Because the filter also reduces the Lyman-α signal, and the near-UV signal can be accounted for as background using the quartz chopper described below, it does not appreciably improve the signal-to-noise (S/N) of the instrument. However, removing near-UV lamp output prevents

changes in scattering due to the presence of cloud or dust particles from compromising the S/N of the instrument, and significantly reduces the background signal to allow for a cleaner measurement.

Quartz Window Chopper

A quartz window is periodically inserted between the lamp and the duct in order to quantify the radiation in the PMT collection region that does not arise from fluorescence of OH. This background radiation is composed of both the small amount of near-UV lamp flux which passes through the filter and scatter of solar radiation off of detection axis surfaces. The quartz chopper is an anti-reflection coated window which transmits ~98% of radiation in the near UV, but effectively blocks all VUV radiation, eliminating the water vapor fluorescence signal. Thus, when the quartz chopper is between the lamp and the duct ("in") the only sources of radiation in the PMT collection window are near-UV lamp scatter and solar scatter, and when the chopper is "out" the PMT detects the sum of OH fluorescence, near-UV lamp scatter, and solar scatter. By subtracting the PMT signal with the chopper in place from that without the chopper, we calculate the signal due to OH fluorescence alone. The background signal is composed of ~100 counts due to solar scatter and ~5 counts from near-UV lamp output; without the Lyman-α filter the near-UV lamp background is on the order of 360 counts. For comparison, the fluorescence signal produces ~700 counts at 4 ppmv H_2O and ~15,000 counts at 100 ppmv H_2O.

VUV Photodiodes

The VUV lamp flux is monitored by two VUV photodiodes to both account for changes in lamp flux over time and provide a secondary method for measuring water vapor in situ. One

photodiode is positioned directly across the duct from the lamp as shown in Figure 2.1 (right). Next to that diode is a VUV-coated mirror which directs some of the lamp flux across the duct again to the second diode, which is positioned next to the lamp. Each photodiode current is directed to a PC board with an electrometer and voltage-to-frequency converter. The surfaces of the diode and mirror mounts are painted with flat black paint to reduce scatter in the duct. Each diode signal can be used to normalize the fluorescence signal observed at the PMT in order to account for changes in fluorescence due to fluctuations in lamp flux. The diodes are also used to measure water vapor via direct absorption using Beer's law over the pathlength between the lamp and each diode. Although the pathlengh is not long enough to provide precise measurements at the lowest H_2O values encountered, short-term changes in water on the order of 100-600 ppmv can be measured accurately. This technique provides a valuable check for the fluorescence measurement and verifies the fluorescence calibration in situ; the measurement is described in greater detail in Section 2.6.1.

PMT and Collection Optics

The PMT assembly collects photons from a ~1 cm^3 volume in the core of the flow tube. Baffles are placed between the flow tube and PMT to narrow the field of view of the PMT and to reduce lamp and solar scatter. The fluorescence signal is first collimated by an anti-reflection coated quartz condensing lens and then passed through a series of filters designed to selectively detect OH fluorescence at 305-325 nm while excluding all other radiation including the excitation wavelength at 121.6 nm. A bandpass interference filter rejects all light from 200-420 nm outside of a window centered on 312 nm with half-width half-maximum of ~10-20 nm, and an AR-coated UG11 visible filter blocks radiation from 410-650 nm. After these filters, the

signal is turned 90^{o} by a mirror which is 99% reflective at 300-320 nm and >95% transmissive in the red and near infrared. Finally, it is passed through a dielectric filter which rejects light from 650-750 nm, and focused by a lens into the photocathode of the PMT. Together this assembly allows for PMT detection of only a narrow wavelength band from ~300-325 nm, in which the only sources of radiation are fluorescence of OH, scatter of near-UV lamp flux, and solar scatter. The filter assembly and PMT are both maintained at temperatures above ~15 ^{o}C by thermostatted heaters to prevent changes in the filter transmission and to ensure proper operation of the PMT.

2.3.2 Inlet and Flow System

The Harvard Lyman-α hygrometer has flown in a spearpod beneath the left wing of NASA's WB-57 aircraft in 9 science missions from 2001 to the present. The instrument and ducting as flown on the WB-57 are shown in Figure 2.2. The Harvard Water Vapor (HWV) instrument consisted of the Lyman-α hygrometer alone from 2001-2008; in this version of the instrument, ram-fed air is sampled through a 4.5" diameter round inlet which extends forward of the spearpod so as to sample air unperturbed by the aircraft or wing. In 2011 the HWV instrument was redesigned to incorporate both Lyman-α and the newly-designed Harvard Herriott Hygrometer (HHH) as independent water vapor measurements in a common duct. HHH uses a tunable diode laser (TDL) to measure water vapor via direct absorption in the infrared, and is described in detail in Chapter 3. In the instrument flown in 2011, the 4.5" round primary inlet was replaced with a 3.5x4" rectangular inlet with two 3" mirrors embedded in the walls to serve as the optical cell for the HHH measurement.

The region downstream of the primary inlet, including the secondary inlet and duct and Lyman-α detection axis, has remained unchanged from 2001 to the present. A 2" square

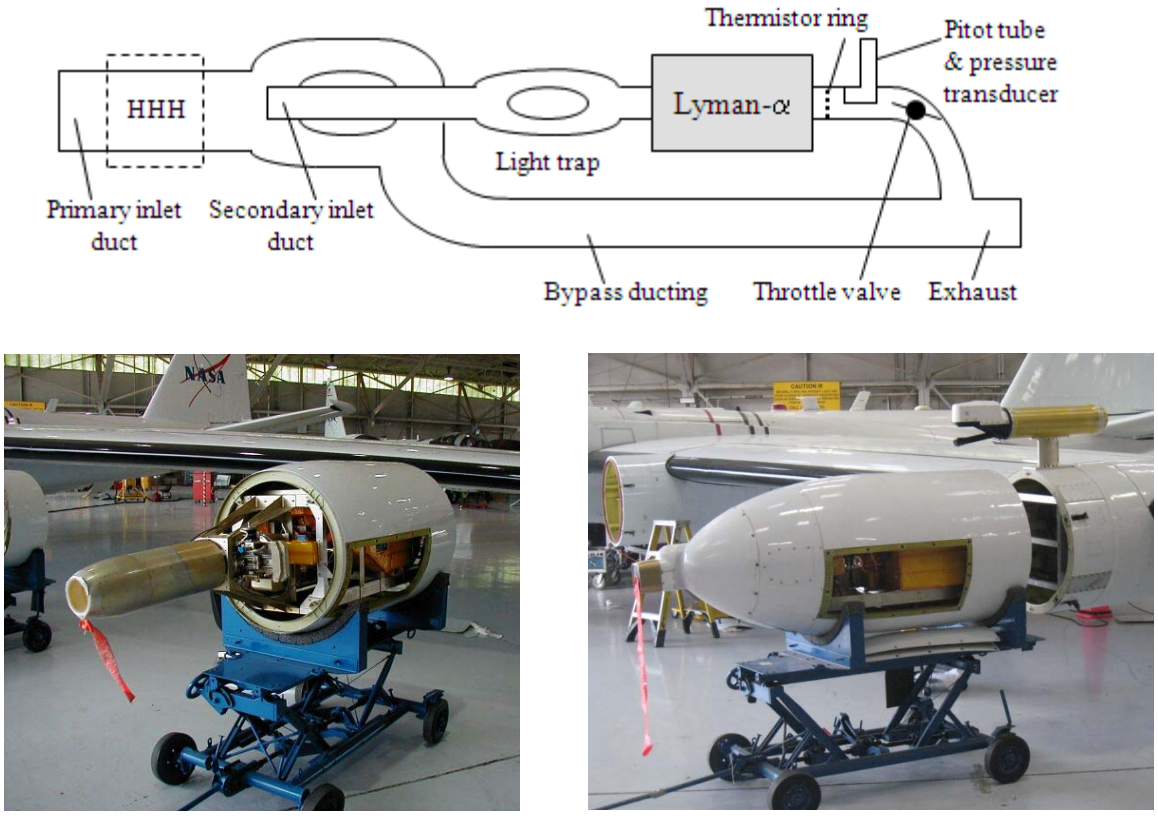

Figure 2.2: Top: A schematic of the HWV instrument. The Lyman-α detection axis and the subsystems that measure temperature and pressure and control the velocity through the instrument duct are labeled; the location of the HHH detection axis, which was included in the payload for the first time in the 2011 MACPEX campaign, is also indicated. Bottom left: The HWV instrument loaded in the spearpod of the WB-57 as it was flown from 2001-2008 using a 4.5" diameter round primary inlet. Bottom right: The HWV instrument as it was flown in 2011 using a 3.5x4" rectangular primary inlet which incorporates the HHH detection axis.

secondary inlet samples the core of the primary duct flow, while a bypass duct brings the remainder of the flow to the exhaust port. A throttle valve controlled by a stepper motor determines the flow in the secondary duct, throttling the flow from the typical aircraft velocity of ~200 m/s to ~100 m/s. The valve is adjustable to allow for periodic variation of the flow velocity from ~20 to 100 m/s, which is used to check for potential outgassing of water vapor from the duct walls. The secondary inlet transitions to an aerodynamic light trap designed to exclude solar scatter, and then to the Lyman-α detection axis. In addition to the light trap, black paint on the duct walls minimizes scatter of solar radiation into the PMT optics. Baffles in front

of the lamp limit scattering of near-UV radiation, and baffles in front of the PMT collection optics minimize the collection of both lamp and solar scatter. Directly after the detection region, three 1 kΩ thermistors positioned across the duct measure the temperature, and a pitot tube connected to a baratron measures the static pressure and mass flow rate. The secondary flow then combines with the bypass duct at the exhaust port, where the air exits the pod.

2.4 Determination of Water Vapor Mixing Ratio

The water vapor mixing ratio in the duct is calculated according to Equation 2.4 from the fluorescence signal measured by the PMT and the empirically derived calibration constant, C_{flr}. The directly measured PMT signal, *S*, is adjusted prior to this calculation to subtract the background signal and normalize it to the VUV lamp flux. The progression from measured PMT and VUV photodiode counts to normalized PMT counts, S_{norm}, is shown for laboratory data in Figure 2.3. The PMT signal is first adjusted to isolate the signal due to fluorescence from OH* from those due to solar scatter and lamp scatter. This is accomplished by subtracting the signal with the chopper in front of the lamp from the signal without the chopper:

$$\Delta S = S_{chopper\ out} - S_{chopper\ in}$$
$$= \left(S_{fluorescence} + S_{solar\ scatter} + S_{lamp\ scatter}\right) - \left(S_{solar\ scatter} + S_{lamp\ scatter}\right) \quad (2.6)$$

to determine ΔS, which represents the PMT signal due to fluorescence alone. Panels (a) and (b) of Figure 2.3 show the raw PMT and VUV counts; the chopper cycles are evident in both signals, with signal counts when the chopper is out indicated in red, and background counts when the chopper is in, interpolated in time, shown in blue.

Recall that the VUV diode is positioned directly across the flow tube from the lamp and monitors the flux of VUV photons from the lamp. To determine S_{norm}, we divide the difference

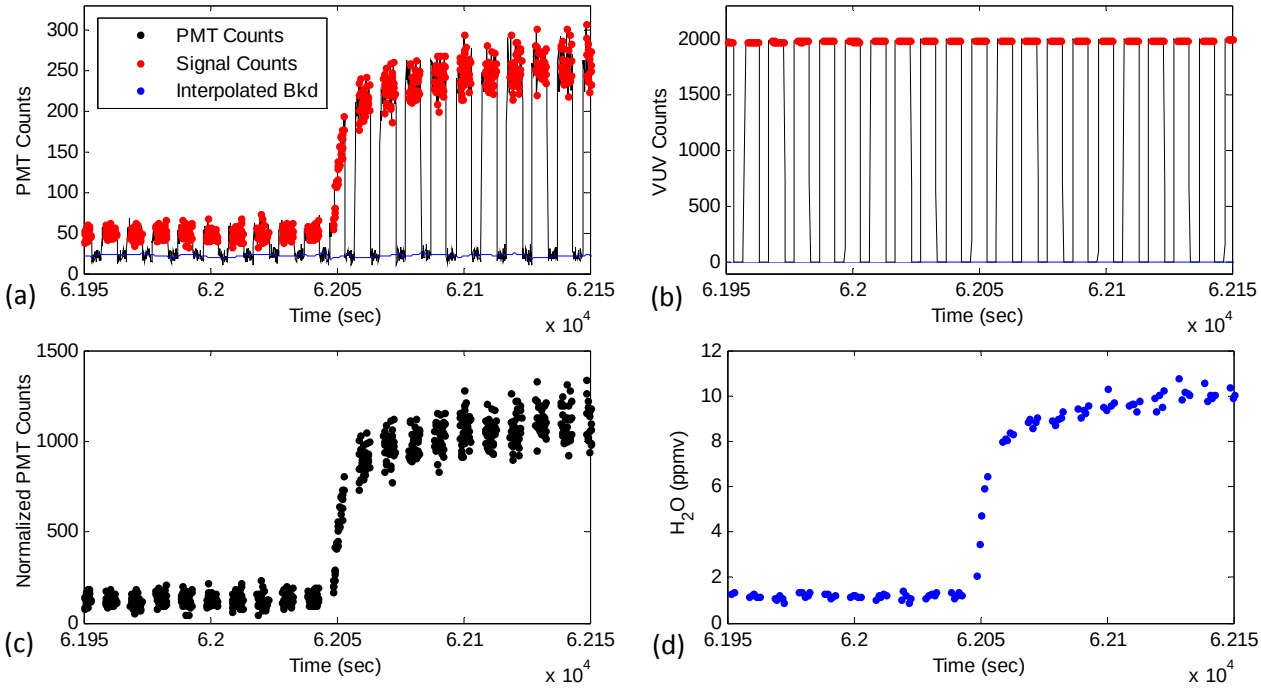

Figure 2.3: Progression from raw PMT and VUV counts to normalized PMT counts and water vapor mixing ratio. (a) Raw PMT counts (black), with signal counts (chopper out) in red and background counts (chopper in), interpolated in time, in blue. (b) As for (a) but for raw VUV diode counts. (c) Normalized PMT counts calculated from the raw PMT and VUV counts according to Equation 2.7. (d) Corresponding H_2O mixing ratio.

PMT signal by the difference signal from the diode ($\Delta VUV = VUV_{chopper\ out} - VUV_{chopper\ in}$) to account for fluctuations in lamp power over time:

$$S_{norm} = \frac{\Delta S}{\Delta VUV * \exp\left(\sum_x \sigma_x[x] l\right)} * 10^4 \tag{2.7}$$

The exponential term accounts for attenuation of the VUV flux along the path of length, l, from the center of the flow tube (the fluorescence region) to the front of the photodiode. The sum over the species, x, in the exponential includes absorption by O_2, CO_2, CH_4, and H_2O, where the correction for H_2O is determined iteratively as the water vapor concentration is calculated and the concentration of O_2 is determined from the pressure and temperature measurements in the instrument duct. In the UT/LS, the H_2O correction typically alters the determined concentration

by less than 3%, and the total correction is typically less than 5%. The normalized PMT signal calculated for these data is shown in Figure 2.3(c).

The normalized PTM signal is converted to water vapor mixing ratio by the following equation, which is simply a rearrangement of Equation 2.4:

$$[\mathrm{H_2O}] = S_{norm} * \frac{1}{C_{flr}} = S_{norm}\left(\frac{1}{C_o} + \frac{q_{air}}{C_o}[\mathrm{M}]\right) \tag{2.8}$$

where C_o and q_{air} are determined empirically as a function of the number density of air, [M], via laboratory calibrations tied to an external water vapor standard. The calculated water vapor concentration for this example is shown in Figure 2.3(d).

2.5 Calibration of the Instrument

The accuracy of the Lyman-α technique depends on accurate determination of the calibration constants, C_o and q_{air}, which link the fluorescence counts measured at the PMT to the water vapor mixing ratio via Equation 2.8. To determine these calibration constants as a function of the number density of air, [M], water vapor titrations are performed at several different duct pressures and PMT fluorescence counts are compared to an external reference water vapor measurement.

2.5.1 Calibration Standards

We use two independent water vapor standards in the laboratory which are each tied to different fundamental properties of the compound: the vapor pressure over liquid water over a bubbler and VUV absorption at 121.6 nm. Because these two standards utilize different

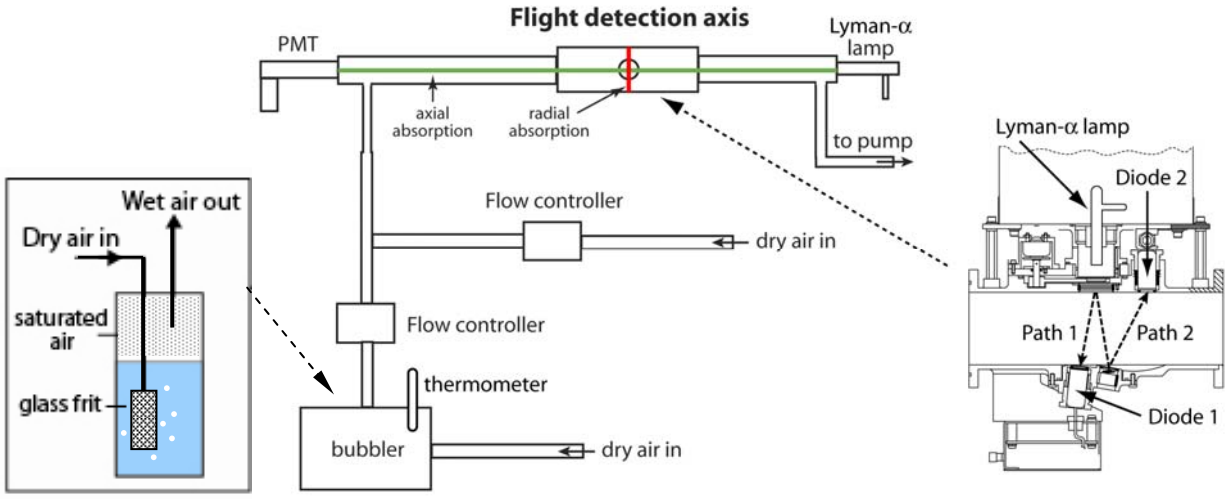

Figure 2.4: Schematic of Lyman-α calibration bench. Controlled quantities of saturated air from the bubbler (the primary calibration standard) are combined with a flow of dry air which is directed to the Lyman-α detection axis. The secondary calibration standard utilizes UV absorption along the length of the flow tube with the indicated Lyman-α lamp and PMT.

properties of water vapor, sources of random and systematic errors related to their implementation should be uncorrelated; therefore, agreement of the two standards serves to verify the accuracy of the system.

A two-stage bubbler is used as both a water addition system and a primary standard for the calibration of Lyman-α; it is shown in Figure 2.4. The water vapor measurement by the bubbler system is based on knowledge of the vapor pressure over liquid water at a given temperature and pressure [*Murphy and Koop*, 2005]. A small flow of air is brought to water vapor saturation by bubbling it through a glass frit immersed in distilled water in two stages; this flow is combined with a main flow of dry air to produce air with known water vapor concentrations of 1-600 ppmv. The carrier gas is either ultra zero air from AirGas which typically contains 1-3 ppmv H_2O, or nitrogen blowoff from a liquid nitrogen tank with ~0.35 ppmv H_2O. The main flow is set using a 50 standard liter per minute (SLM) MFC flow controller; the saturated air flow is set using a 100 standard cubic centimeter per second (SCCM) MFC flow controller. The output of the bubbler is plumbed to the detection axis flow tube and

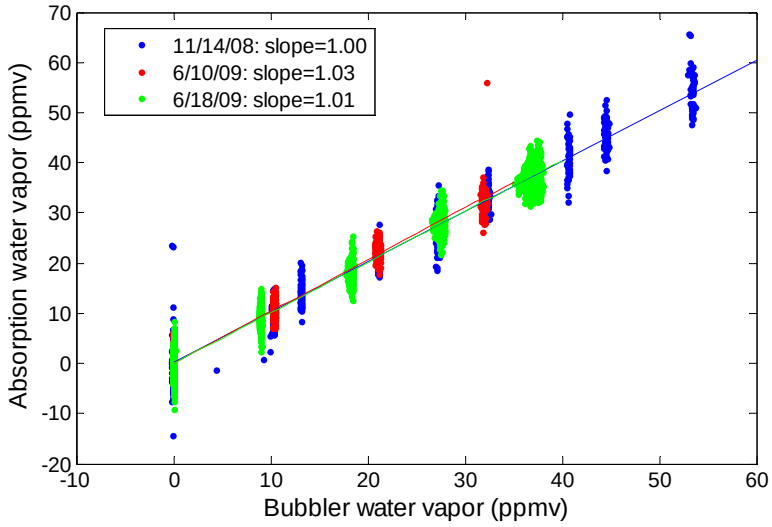

Figure 2.5: Comparison between the water vapor measurements by the bubbler and the long-path absorption technique at 121.6 nm.

then output to a large vacuum pump. The added water vapor concentration is known to within 3% based on the uncertainty in the temperature and pressure at the bubbler, the flow rates of the two flow controllers adding dry and saturated air, and achievement of 100% saturation of air after the bubbler.

As a secondary water vapor standard, we use absorption at 121.6 nm over a ~1 m pathlength along the axis of the duct as shown in Figure 2.4 (green line). An additional Lyman-α lamp is positioned at one end of the calibration duct and a PMT which is selective for VUV radiation is placed at the other end, and water vapor is calculated directly from Beer's law using the well-established absorption cross-section at 121.6 nm [*Lewis et al.*, 1983; *Kley*, 1984]. The bubbler and absorption methods consistently agree to within 3% from 3 to 300 ppmv H_2O; a comparison of the two techniques is shown in Figure 2.5.

The bubbler system has also been compared to two different NIST traceable MBW frostpoint hygrometers with stated accuracy down to a frostpoint of -95°C. The bubbler was compared with the MBW used to calibrate the German Fast In-situ Stratospheric Hygrometer

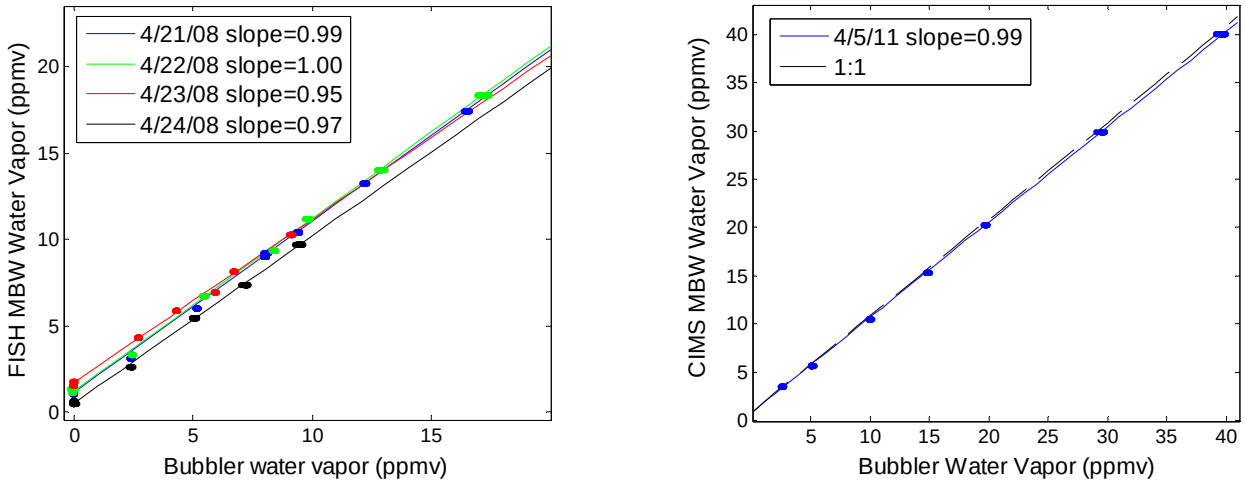

Figure 2.6: Comparison between the bubbler water vapor measurement used as a primary standard for the Lyman-α instrument and the MBW frostpoint hygrometers used by the FISH instrument (left) and the CIMS instrument (right).

(FISH) in 2008, and the two techniques on average agreed to within 2%, and at worst to within 5%. The bubbler was also compared with the MBW used to calibrate the NOAA Chemical Ionization Mass Spectrometer (CIMS) in 2011, and they agreed to within 2%. These comparisons are shown in Figure 2.6; non-zero intercepts in the comparisons arise because the bubbler measures water vapor added to the main flow of "dry" air, which contains a variable 1-2 ppmv H_2O, while the MBWs measure total water in the sample. The agreement of the bubbler with both direct absorption at 121.6 nm and these commercial frostpoint hygrometers verifies the accuracy of both the technique and its implementation in the laboratory.

2.5.2 Determination of Calibration Constants

The calibration constants C_o and q_{air} are determined empirically in the laboratory by sampling known quantities of water vapor from the bubbler system over a range of temperatures and pressures. In the calibration of a flight instrument, it is essential to mimic field sampling conditions as closely as possible in order to be assured that laboratory results are applicable to flight data. A key benefit of our ducted sampling design is that the instrument and its duct can be

integrated into a laboratory calibration system with no changes to the axis itself and under conditions very close to those in flight. The two-inch square detection axis flow tube is plumbed to receive an input of air from the bubbler and output to a large vacuum pump which pulls air through the duct at speeds of up to 40 m/s. Pressures observed in the field are easily achieved by varying the input air flow and throttling the exit valve to the vacuum pump to vary the velocity of air in the duct. UT/LS temperatures are produced in the lab by placing the instrument and ducting within a box of insulating foam that is cooled with liquid nitrogen blowoff. We are able to run the instrument in the lab at temperatures down to -50 ^{o}C.

A calibration run consists of varying the amount of saturated air added from the bubbler system while measuring water vapor with Lyman-α at several different pressures. The observed PMT counts and water vapor added by the bubbler during a typical calibration run are shown in Figure 2.7, panel (a). First the pressure is held constant while the added water vapor concentration is varied in a step-wise fashion; the pressure is then changed and water vapor titrated again, at several different pressures between 40 torr and 250 torr. At each pressure, normalized PMT counts (calculated from observed PMT and VUV diode counts via Equation 2.7) are plotted vs. added water vapor concentration as shown in panel (b); a linear fit to the data gives the slope, C_{flr}, which represents the sensitivity of the detection axis to H_2O at each pressure. $1/C_{flr}$ is then plotted vs. the air number density associated with each pressure as shown in panel (c). Recall from Equation 2.8 that:

$$\frac{1}{C_{flr}} = \frac{1}{C_o} + \frac{q_{air}}{C_o}[\mathrm{M}] \tag{2.9}$$

Therefore, the linear best fit to $1/C_{flr}$ vs. [M] has slope q_{air}/C_o and intercept $1/C_o$. In this way, the calibration constants q_{air} and C_o are determined such that the mixing ratio of water vapor can be

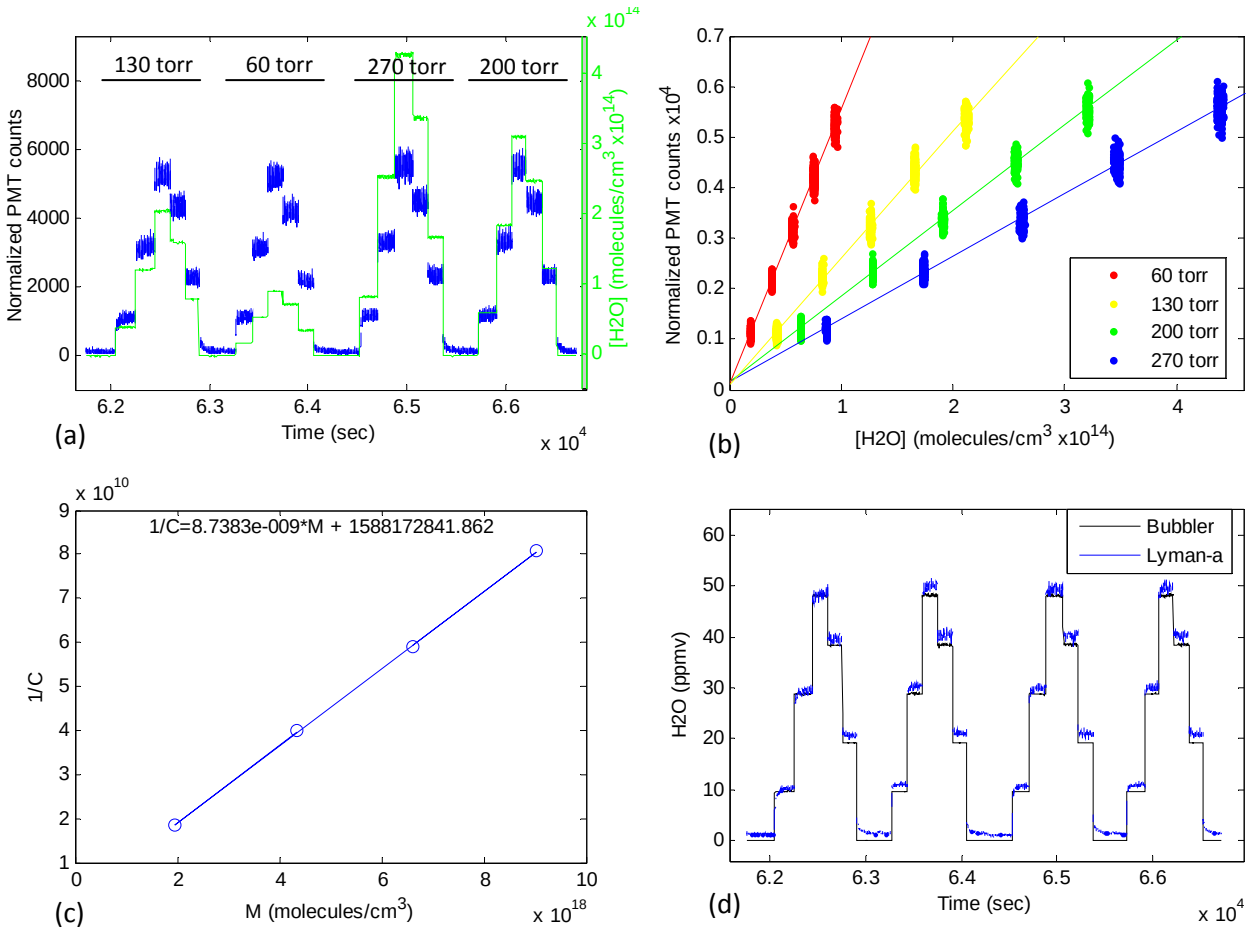

Figure 2.7: Sample calibration analysis. (a) Normalized PMT counts (blue) and water vapor concentration added by the bubbler (green) vs. time. (b) Normalized PMT counts vs. water vapor added, with titrations at each pressure indicated by color. The slope of the fit through each titration is equal to C_{flr}. (c) $1/C_{flr}$ vs. the number density of air, [M], at which the data were obtained. The best fit to the data is a line of slope q_{air}/C_o and intercept $1/C_o$. (d) Water vapor mixing ratio measured by Lyman-α based on the calibration constants determined in panel (c), compared to the water vapor added by the bubbler.

calculated from the observed fluorescence signal at any pressure. Panel (d) shows the final water vapor mixing ratio measured by the instrument based on the calibration constants determined through this process, along with the water vapor mixing ratio added by the bubbler.

Notice in panel (d) that the water vapor measured by the Lyman-α axis is consistently ~1 ppmv higher than that added by the bubbler. This additional water vapor is attributed mainly to residual water in the carrier flow of "dry air", and to a lesser extent to any water desorbed from the walls of the duct upstream of the detection axis. However, notice that the calibration procedure above uses only the *slope* of the relationship between normalized PMT counts and added water vapor; therefore the uncertain amount of residual water vapor does not factor into the calibration. The change in water vapor concentration at each point in the titration, which is known precisely, is the only value necessary to determine the calibration constants. As the relationship between C_{flr} and $[H_2O]$ is linear, we can extrapolate to determine the fluorescence counts at zero water vapor. Where Lyman-α measures 1 ppmv and the bubbler adds no water, it constitutes a measurement of the residual water in the carrier gas. Therefore, in the absence of additive instrument artifacts, the calibration allows for establishing an absolute relationship between fluorescence counts and water vapor.

To verify that no additive artifacts (i.e. uncorrelated with water vapor concentration) impact the system, we sample extremely dry (<0.35 ppmv) nitrogen blowoff from a liquid nitrogen dewar. In these tests, Lyman-α measured as low as 0.3 ppmv, constraining the maximum possible offset in the measurement. In fact, when the liquid nitrogen blowoff was sampled with the Harvard Herriott Hygrometer (HHH), a clear water vapor absorption line was observed, confirming the presence of some water in the nitrogen, and demonstrating that any offset in the Lyman-α measurement is likely much less than 0.3 ppmv. Although we have no

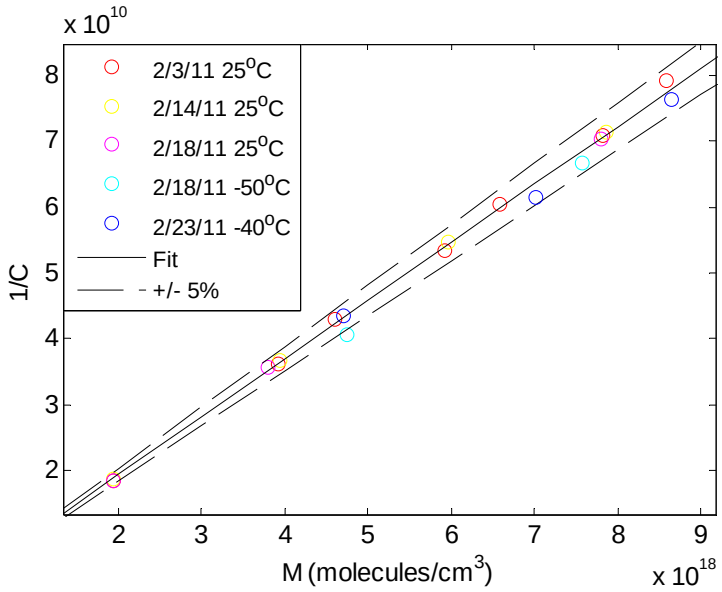

Figure 2.8: $1/C_{flr}$ vs. the number density of air, [M], for calibrations over several days and at varying temperatures. The best fit to the data is shown as a black line whose slope and intercept represent the calibrations constants, q_{air}/C_o and $1/C_o$, respectively.

reason to believe a positive or negative bias exists, in addition to the calibration uncertainty associated with the instrument, we include -0.3 ppmv uncertainty in our error bars to account for this possibility.

Although the calibration example shown above was performed at room temperature, calibrations have been performed at temperatures down to -50 ^{o}C to demonstrate that the calibration constants and instrument performance remain stable at the low temperatures encountered in the UT/LS. Figure 2.8 shows a plot of $1/C_{flr}$ vs. [M] for calibrations performed over several days and at temperatures ranging from 25 to -50 ^{o}C. Notice that the cold temperature calibrations fall within 5% of the room temperature calibrations, verifying that calibration is not temperature dependant.

2.6 In-flight Diagnostic Tests

2.6.1 Calibration Assessment: In situ Absorption Measurement

During flight measurements, absorption of VUV lamp radiation along the pathlength from the center of the duct to each of the two VUV photodiodes is used as a secondary measurement of water vapor to verify the laboratory calibration for flight conditions. The fluorescence and absorption measurements are two independent methods which each have independent sources of error; agreement of the two techniques under flight sampling conditions constrains the possible errors in the technique as well as the potential for drift of the calibration since it was established in the laboratory.

The locations of the VUV diodes and the relevant absorption pathlengths are shown in Figure 2.1. The water vapor concentration is calculated according to Beer's law:

$$\Delta[\mathrm{H_2O}] = \frac{-1}{\sigma_{H2O} * l} \ln\left(\frac{I_{VUV}}{I_{VUV,o}}\right) \tag{2.10}$$

where σ_{H2O} is the absorption cross section for water vapor and *l* is the pathlength from the center of the duct to the second photodiode. Alternatively, we could use the ratio of the signals from the two diodes in order to account for changes in the VUV lamp flux, which would sacrifice precision by using a shorter pathlength; however, because we look at water vapor changes over a short period of time, we expect the lamp flux to remain quite constant and use the longer pathlength. In Equation 2.10, $I_{VUV} = \Delta VUV / \exp\left(\sum_x \sigma_x[x]l\right)$, where ΔVUV refers to the difference between the VUV signal with the chopper "out" and that with the chopper "in", and the exponential accounts for absorption by O_2, CO_2, and CH_4. By accounting for absorption by O_2 based on measured temperature and pressure in the duct, changes in pressure do not impact the water vapor absorption measurement. Notice that this method is capable of determining the

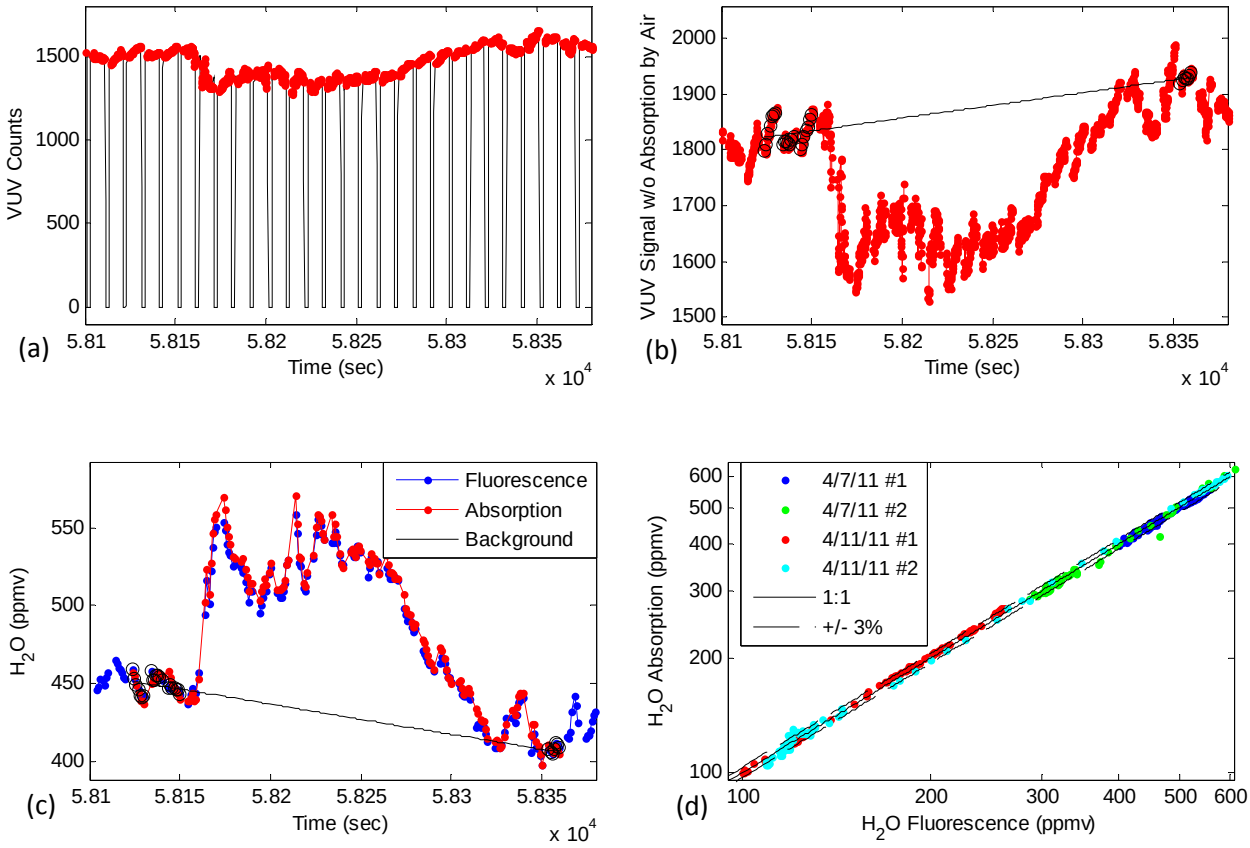

Figure 2.9: Left: Comparison of the fluorescence and radial absorption measurements of water vapor during the 4/7/11 flight during the MACPEX mission. The black line indicates the background water vapor concentration used for the absorption measurement. Right: Comparison of fluorescence and absorption measurements for two distinct segments of the 4/5/11 flight and two segments of the 4/11/11 flight.

magnitude of a change in water vapor concentration, but not the absolute water vapor concentration. $I_{VUV,o}$ represents the VUV diode counts (adjusted for absorption by air) associated with a baseline water vapor concentration to which changes in water vapor are compared. We prefer to apply the absorption measurement to periods in which water changes by at least 100 ppmv in a short period of time before returning to its initial value, such that a background value can be obtained at the start and end of the period.

Figure 2.9 (a) shows the raw VUV diode counts for a water vapor excursion during the flight of 4/7/11 in the MACPEX campaign. Panel (b) shows the difference counts (signal minus background) corrected for absorption by air; the points chosen as background are indicated with

black circles and the interpolated background ($I_{VUV,o}$) is shown as a black line. The corresponding water vapor concentrations measured by both fluorescence and absorption are shown in panel (c); the background points are again indicated with black circles and the interpolated background with a black line. For the absorption method, the absolute water vapor mixing ratio is determined by assuming that the concentration for the background points is equal to that measured via fluorescence, and for all other points is equal to the interpolated background value plus the $\Delta[H_2O]$ calcualted according to Equation 2.10 above. Water vapor as measured by the fluorescence and absorption techniques are compared for several flight segments in Figure 2.9 (d). The change in water vapor during an excursion as measured by the two techniques typically agrees to within 3%, verifying the accuracy of the laboratory calibration and its efficacy under flight conditions.

2.6.2 Contamination Assessment: Velocity Scan

A primary concern facing any in situ water vapor instrument is the effect of water outgassing off of duct surfaces into the detection volume. As instruments travel from the surface where water vapor is typically 1% of air to the UT/LS where water vapor is on the order of 10s of ppmv, water can easily adsorb onto surfaces and then desorb during flight to contaminate the measurement. In the Lyman-α instrument, the very fast flow rates on the order of ~100 m/s allow for fast drying of duct surfaces and minimal contamination of the measurement. To verify this, a throttle valve in the secondary duct is used to periodically vary the duct flow from ~40-100 m/s during flight. Assuming that outgassing produces a small constant flux of water vapor into the duct, if the duct flow speed is reduced by half, the amount of spurious water from outgassing which reaches the detection volume should double. The results of a typical velocity

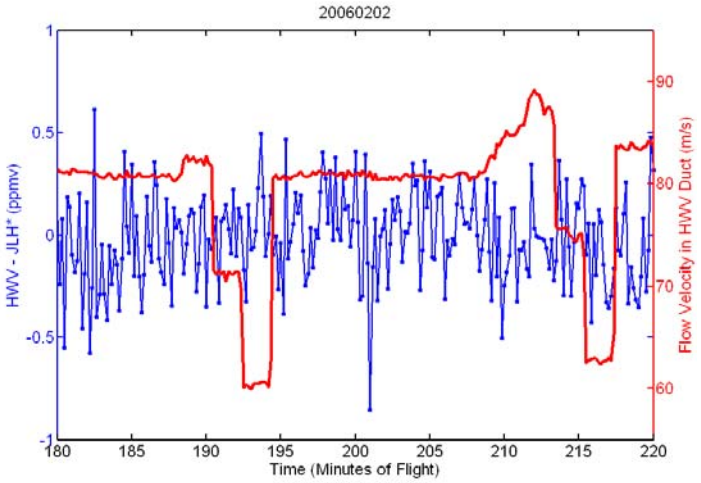

Figure 2.10: In situ diagnostic velocity scan from the flight on 2/2/06. The difference between water vapor measured by Lyman-α and the open-path JLH instrument is shown as a function of time; the velocity in the duct is overlain in red, which is periodically changed during flight via a throttle valve [*Smith*, 2011].

scan are shown in Figure 2.10. The difference between water vapor measured by Lyman-α and by the JPL Laser Hygrometer (JLH), which measures in an open-path cell beneath the wing, is shown with time, in addition to the duct flow velocity. There is no discernible change in the difference between the two instruments as the duct velocity changes from 60 to 90 m/s, indicating that the contribution to the Lyman-α measurement from outgassing is negligible.

2.7 Flight Performance

Table 2.1: Lyman-α instrument performance during the MACPEX mission for 1-second data.

	1-10 ppmv	10-100 ppmv	>100 ppmv
Precision	0.1 ppmv	1-3%	1%
Accuracy	±5-10%	±5%	±5%
Offset	<0.3 ppmv	<0.3 ppmv	<0.3 ppmv

The Lyman-α instrument was designed to obtain accurate and precise water vapor measurements with fast time-response at mixing ratios from 1-600 ppmv. The instrument's precision and accuracy over a range of water vapor mixing ratios are shown in Table 2.1; all

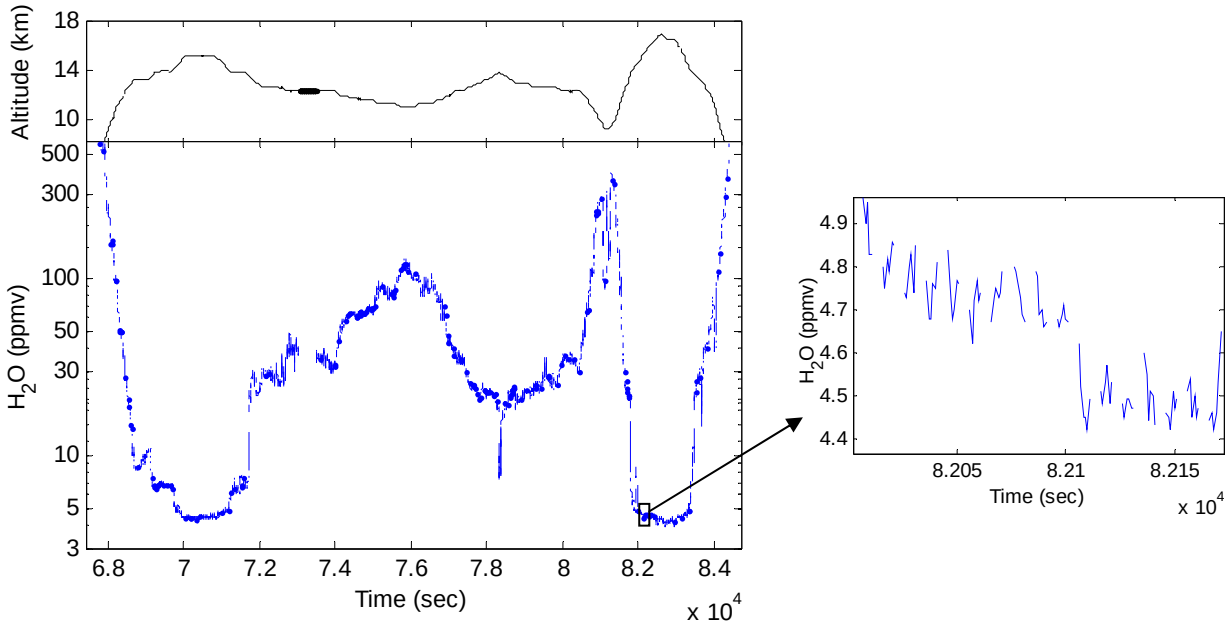

Figure 2.11: Flight measurements of H_2O by the Lyman-α instrument during the flight of 4/25/11 in the MACPEX campaign. Left: H_2O measurements over the full scale of operation shown on a logarithmic scale. The altitude along the flight path is shown in the top panel. Right: Zoom in on a low water flight segment to demonstrate instrument precision.

values correspond to 1-second data. At the lowest water vapor concentrations encountered, the instrument has ~0.1 ppmv or 3% precision in 1 second, while at higher water vapor concentrations the precision improves to ~1%. Based on the calibration uncertainty of ±3%, the observed precision, and lowest water vapor concentrations measured in the laboratory, we estimate total uncertainty to be ±5% - 0.3 ppmv, except where precision limitations at the lowest mixing ratios lead to ±10% - 0.3 ppmv uncertainty. Figure 2.11 shows sample water vapor measurements by Lyman-α during the 4/25/11 flight in the MACPEX campaign. The left panel illustrates the high precision obtained over a wide range of concentrations, while the right panel zooms in on a low water segment to demonstrate the ~0.1 ppmv precision at 4 ppmv H_2O. Further analysis of the MACPEX flight results including comparisons with other water vapor instruments is discussed in Chapter 3.5.

References

Kley, D., and E. J. Stone (1978), Measurement of Water Vapor in Stratosphere by Photo-Dissociation with Ly-Alpha (1216 Å) Light, *Rev Sci Instrum*, *49*(6), 691-697.

Kley, D. (1984), Ly(α) Absorption Cross-Section of H_2O and O_2, *J. Atmos. Chem., 2*, 203-210.

Lewis, B. R., I. M. Vardavas, and J. H. Carver (1983), The Aeronomic Dissociation of Water Vapor by Solar H Lyman α Radiation, *J. Geophys. Res., 88*, 4935-4940.

Murphy, D. M. and T. Koop (2005), Review of the vapour pressures of ice and supercooled water for atmospheric applications, *Q. J. R. Meteorol. Soc., 131*, 1539–1565.

Pittman, J. (2005), *Transport in the tropical and subtropical lower stratosphere: insights from in situ measurements of chemical tracers*, Thesis, Harvard University.

Schwab, J. J., E. M. Weinstock, J. B. Nee, and J. G. Anderson (1990), In Situ Measurement of Water Vapor in the Stratosphere with a Cryogenically Cooled Lyman-Alpha Hygrometer, *J Geophys Res-Atmos*, *95*(D9), 13781-13796.

Smith, J. B. (2011), *The Sources and Significance of Stratospheric Water Vapor: Mechanistic Studies from Equator to Pole*, Thesis, Harvard University, Department of Earth and Planetary Sciences.

Weinstock, E. M., E. J. Hintsa, A. E. Dessler, J. F. Oliver, N. L. Hazen, J. N. Demusz, N. T. Allen, L. B. Lapson, and J. G. Anderson (1994), New Fast-Response Photofragment Fluorescence Hygrometer for Use on the NASA ER-2 and the Perseus Remotely Piloted Aircraft, *Rev Sci Instrum*, *65*(11), 3544-3554.

Chapter 3

The Harvard Herriott Hygrometer:

Operation and Flight Results

3.1 Introduction

As we emphasized in Chapter 1, accurate and precise water vapor measurements are essential to predicting future stratospheric water vapor concentrations in the context of a warming climate. However, the suite of water vapor instruments operating in the upper troposphere and lower stratosphere (UT/LS) have continuously shown disagreements on the order of 1-2 ppmv over the last 10 years, which corresponds to 30%-50% uncertainty at the water vapor concentrations of the tropical tropopause [*Weinstock et al*., 2009]. This uncertainty impedes our comprehension of the detailed processes that dictate the distribution and phase of water in the UT/LS, and the mechanisms that transport water from the troposphere to the stratosphere. Furthermore, this measurement uncertainty is too great to support a robust observational dataset from satellite instruments, or to reliably detect trends in water vapor concentrations, particularly at the level of ~1%/year.

Various techniques have been used to measure water vapor in the UT/LS, including balloon-borne frostpoint hygrometers, satellite-borne remote sensors, and aircraft-borne Lyman-α hygrometers and tunable diode lasers (TDLs). The balloon-borne NOAA Cryogenic Frostpoint

Hygrometer (CFH) [*Vömel et al*., 2007] measures water vapor based on the temperature at which a thin layer of frost is maintained on a mirror. One of several satellites that have measured water vapor in the stratosphere, the Microwave Limb Sounder (MLS) on the Aura satellite detects water vapor from the atmosphere's microwave emission spectrum. The Lyman-α technique, which is used in both the aircraft-borne Harvard Water Vapor (HWV) instrument [*Weinstock et al*., 1994] and the German Fast In-situ Stratospheric Hygrometer (FISH) instrument [*Zöger et al*., 1999], is an ultraviolet photofragment fluorescence measurement. The TDL instruments, including the JPL Laser Hygrometer (JLH) [*May*, 1998], the similar UAS Laser Hygrometer (ULH), and the JPL Aircraft Laser Infrared Absorption Spectrometer (ALIAS) [*Webster et al.*, 1994], measure infrared absorption with a tunable laser in a multipass cell. These aircraft-borne instruments have very different sampling conditions in flight; on NASA's WB-57 aircraft, JLH and ULH utilize open-path optical cells mounted under the aircraft wing, ALIAS and FISH each use a closed cell in the aircraft fuselage with an isokinetic inlet, and HWV samples ram-fed air at near-aircraft velocities from a spearpod on the wing. ALIAS and FISH's closed cells and slow flow rates allow for some water contamination due to outgassing from surfaces, with a period of drying typically observed after each aircraft ascent. The open-path method of JLH avoids water contamination from surfaces, but potential gradients beneath the wing impede accurate determination of pressure and temperature at the optical cell, which is critical to water vapor calculations. The HWV open-throated duct's fast flow rate has been shown to be free of wall contamination, and its more controlled duct environment allows for accurate temperature and pressure measurements at the detection axis.

Over the past 10 years, measurements by these instruments have generally fallen into two groups, with CFH, MLS, and FISH typically measuring ~1-2 ppmv lower than HWV and

ALIAS. JLH and HWV agreed well during several field campaigns prior to 2003, after which JLH began to agree well with CFH and MLS. To address these long-standing discrepancies, the CFH, JLH, FISH, and HWV instruments were compared at the AIDA chamber in Karlsruhe, Germany, under controlled laboratory conditions. The comparison showed that all instruments agreed to within 0.3 ppmv in the lab, a stark contrast from past disagreements in flight [*Weinstock et al.*, 2009]. These results indicate that measurement discrepancies are likely due to differences between the laboratory and in-flight sampling environments of one or more instruments rather than calibration differences or intrinsic faults in a given measurement technique.

The continuing disagreement of these instruments in flight thoroughly reinforces the need for measurements with high precision and unassailable accuracy. In order to introduce a new viewpoint to the field with a specific emphasis on accuracy and stability, we have designed a new TDL hygrometer, the Harvard Herriott Hygrometer (HHH). We chose the TDL technique because it allows for a compact, lightweight instrument with high accuracy and precision. Although HHH employs the infrared absorption technique implemented in other TDLs, it is unique among UT/LS instruments in its use of direct absorption rather than second harmonic detection. HHH is also set apart by its integration into a common duct with the heritage Lyman-α instrument, whose accuracy has been validated over 19 years of flights. The two instruments were flown together in the spearpod of NASA's WB-57 aircraft as the new dual-axis Harvard Water Vapor instrument. By observing the same air mass with two independent instruments with independent sources of uncertainty, we remove sampling conditions as a potential factor in instrument agreement, and constrain the accuracy of the measurement more stringently than would be achieved by a single measurement technique.

While JLH and HHH operate in the same spectral region and have similar optical cells, we hope to achieve more verifiable accuracy with HHH by using direct absorption instead of second harmonic detection. Second harmonic detection is a technique designed to improve an instrument's precision via current modulation. In a general TDL, a sawtooth current ramp is applied to the laser output to scan its wavelength across the absorption line of interest; in second harmonic detection, a small-amplitude sinusoidal waveform of frequency f is added to the sawtooth ramp, and the detector signal is demodulated at a frequency 2f [*Reid and Labrie*, 1981]. The resulting second harmonic spectrum allows for increased precision by producing a positive signal on a near-zero baseline, instead of a detecting a small absorption signal subtracted from a large baseline as in direct absorption. However, the use of computer generated match-up matrices adds complexity to the technique, and the relationship between the water vapor concentration and absorption peak height is dependent on knowledge of the laser modulation amplitude, which can drift over time. Second harmonic detection therefore requires repeated calibration to an external standard. Direct absorption, on the other hand, allows for calculating the water vapor concentration directly from the observed spectrum based on spectroscopic parameters in the HITRAN database. Direct absorption also offers greater stability over time as its sensitivity to water vapor is determined by spectroscopy rather than calibration. Therefore, the key trade-off in second harmonic detection is in sacrificing the accuracy of a direct link between line depth and water vapor concentration in favor of increased precision. However, recent advances within our group in the development of data acquisition systems and signal processing have allowed us to achieve precision comparable to that of JLH while utilizing a direct absorption technique. We can therefore avoid the limitations in accuracy associated

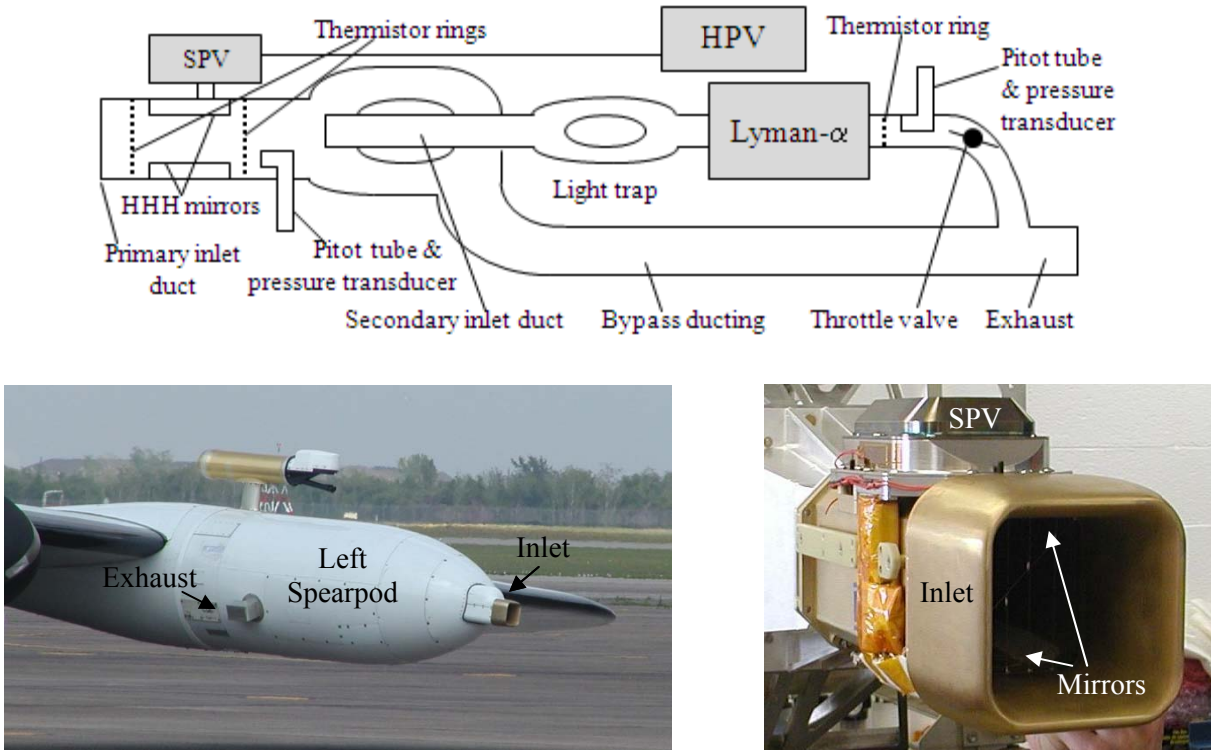

Figure 3.1: Top: A schematic of the newly reconfigured HWV instrument that includes both the Lyman-α and HHH detection axes. The subsystems that measure temperature and pressure, and control the sampling and velocity through the instrument duct are labeled. Bottom left: The HWV instrument loaded in the spearpod of the WB-57 during the MACPEX mission. Bottom right: Looking into the primary inlet of the HWV instrument.

with second harmonic detection while maintaining extremely high precision at 1 Hz. HHH is the first instrument to measure water vapor in the UT/LS using direct absorption spectroscopy.

3.2 The Harvard Herriott Hygrometer (HHH)

The Harvard Herriott Hygrometer was first deployed in the Mid-latitude Airborne Cirrus Properties Experiment (MACPEX) campaign in spring 2011 in the left spearpod of NASA's WB-57 aircraft. The instrument is optimized to measure water vapor in the upper troposphere and lower stratosphere (UT/LS) at concentrations from 1-600 ppmv. Water vapor is measured by scanning the output of a tunable diode laser over a rotational-vibrational water vapor

transition in the infrared at 7181.16 cm^{-1}. The light is directed into a Herriott cell composed of two 7.6 cm mirrors, in which the light passes 92 times, and the water vapor concentration is calculated directly from the depth of the resulting water vapor absorption line. HHH was combined with the Harvard Lyman-α hygrometer in a common duct as shown in Figure 3.1. The HHH optical cell is located directly after the primary inlet at the front of the spearpod, where sampled air passes between the Herriott cell mirrors embedded in the walls of the duct. Farther down the duct, a secondary inlet samples the core of the main flow and directs the air to the Lyman-α detection axis, where water vapor is independently measured before the air leaves the spearpod at the exhaust. In the following discussion, we will divide the instrument into three main subsystems: (1) the laser and optical system; (2) the inlet and flow system; and (3) the data acquisition system.

3.2.1 Laser and optical system

The wavelength of interest is generated by a distributed feedback (DFB) laser from NEL America. It operates at room temperature, has an output power of 30 mW and produces light centered around 1393 nm (7179 cm^{-1}). This laser was chosen because the water line at 7181.16 cm^{-1} is strong enough (10^{-6} cm^{-1} $ppmv^{-1}$ under lower stratospheric pressure and temperature conditions) to allow for the desired accuracy and precision by means of direct absorption detection in a Herriott cell. In addition, because the telecommunication industry operates in the near-IR, there has been significant funding and technological advancement in this spectral region making these lasers commercially available, robust, relatively inexpensive, lightweight, and compact (on the scale of a quarter). Also, the spectroscopy in this wavelength region, including the line strengths and widths, are well studied in the literature. The laser is fiber coupled,

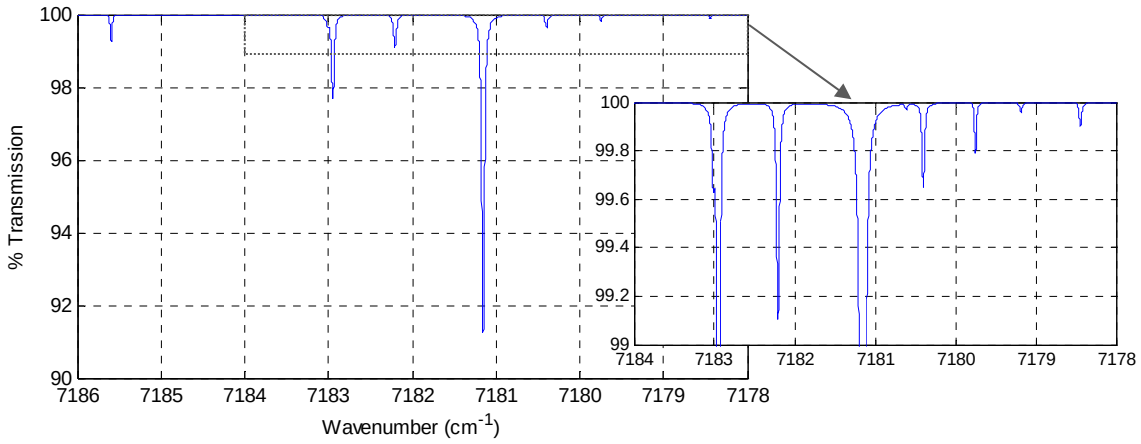

Figure 3.2: Synthetic absorption spectrum for 100 ppmv of H_2O in the region of the laser output calculated based on the HITRAN database [*Rothman et al*., 2009].

allowing for flexibility in the design of a flight instrument because the optical cell can be remotely located from the rest of the instrument components. The laser wavelength is scanned over the line of interest using a current-driven sawtooth waveform produced by a waveform generator designed in-house. The laser wavelength can also be more broadly tuned with temperature adjustment. Figure 3.2 shows a synthetic absorption spectrum in the region of the laser output calculated based on the HITRAN database [*Rothman et al*., 2009]. By broadly tuning the laser output with temperature, we can identify each absorption line based on the line depth and sequence to be assured that we are centered on the correct absorption line for the measurement.

The laser is housed in an enclosed pressure vessel referred to as the HHH pressure vessel (HPV), which is maintained at 1 atm pressure and 20^{o}C, and located remotely from the main Herriott cell (Figure 3.3). The laser beam is split using a fused fiber beam splitter (OzOptics, part FOBS-13P) into three separate axes: 90% of the light is directed to the main Herriott cell, 5% is sent to the background detector, and 5% is sent to a silicon etalon. The spectrum at each axis is detected via an InGaAs photodetector (GPD Optoelectronics Corp, part GAP300) coupled to an in-house pre-amplifier system. The etalon and background axes are also housed in the

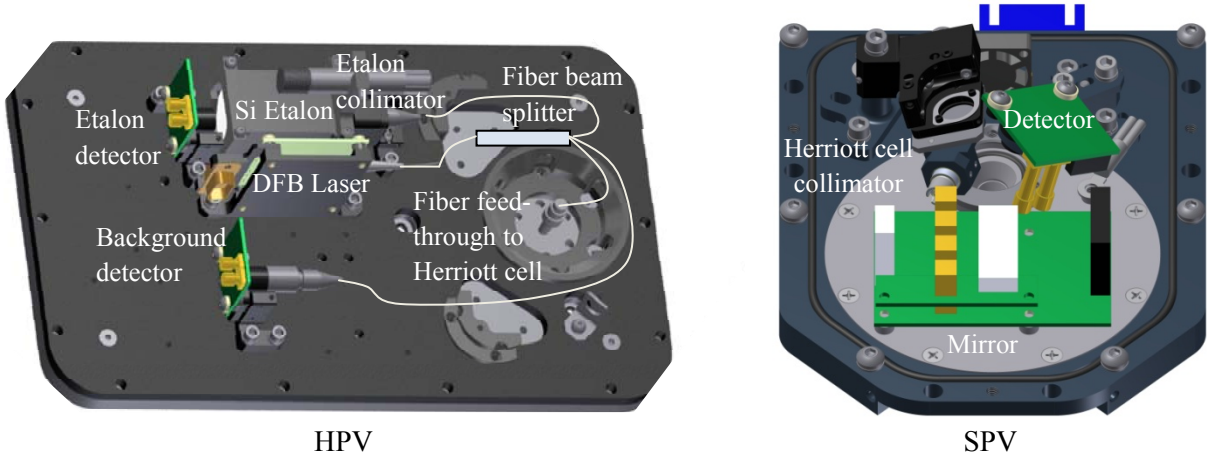

Figure 3.3: Diagram of HHH optical components. Left: HHH pressure vessel. Right: Signal pressure vessel.

HPV; the light reaches the main axis by leaving the HPV and traveling through an armored fiber to the Herriott cell at the forward inlet. At the background axis, the laser output is attached directly to the photodetector to monitor how laser power varies as the wavelength is current-tuned over the absorption line. At the etalon axis, the laser is passed through a single crystal silicon rod of diameter 25.4 mm and length 50.4 mm with flat polished ends (Light Machinery, part OP-2638). Because the laser tuning rate is slightly non-linear, the fringe spacing produced by the etalon is used to determine the wavelength tuning rate.

At the main axis, the laser is collimated with a 2 mm focal length adjustable collimator (ThorLabs, part CFC-2-x) and turned 90^{o} with a single mirror to direct it through a hole in one mirror and into the Herriott cell. The Herriott cell is composed of two 7.62 cm diameter zerodur mirrors with radii of curvature 220 +/- 1 mm. Both mirrors have a protective chromium-gold primary coating with an Al_2O_3 top layer. The front mirror contains a single hole to accommodate both the entrance and exit beams; the hole is 5 mm in diameter and 3.18 cm from the mirror center, drilled at 8.21^{o} vertical to the mirror surface, with an added acceptance angle on the rear side. Mirror spacing is 10.3 cm at the edge (with 10.92 cm slant length that the laser travels per pass), which facilitates a 92-pass pattern, for a total pathlength of 10.05 m. This

pathlength was confirmed in the laboratory by creating the same pattern with a Leica laser distance meter. This mirror spacing was chosen to maximize the total pathlength of the optical cell while maintaining a compact design for in-flight mounting considerations. Upon completion of the multipass pattern within the optical cell, light exits through the same hole as entry and is focused onto the photodetector.

The mirror spacing is fixed in place by two 10.5 x 3.8 cm I-shaped beams on either side of the mirror mounts. The mirror mounts and I-beams are made of Invar, a nickel steel alloy with an extremely low coefficient of thermal expansion, which prevents expansion or contraction over the large temperature gradients the instrument experiences from the ground to the UT/LS. Heat is applied to the mirror mounts and I-beams and their temperature is regulated to further prevent any movement of the mirrors that could affect alignment. The mounts hold the mirrors in place such that the surface of each mirror is flush with the inside of the duct, while silicon O-rings allow the mirror apparatus to float with respect to the duct such that expansion or contraction of the duct walls due to temperature changes will not change the position of the mirrors relative to each other.

The Herriott cell laser collimator, detector, and associated electronics, as well as the mount for the mirror with the hole, are enclosed in a small vessel sitting on top of the duct called the signal pressure vessel (SPV), which is shown in Figure 3.1 (bottom right) and Figure 3.3. The collimator and detector mounts are made of Invar and the vessel is under temperature control to maintain 20^{o}C so that the mounts will not expand or contract and change the laser alignment established on the ground. Inside this vessel, the laser travels 1.3 cm from the collimator through the mirror hole and then 0.9 cm from the mirror hole back to the detector. It is essential to minimize the amount of water in this pathlength within the SPV to avoid adding

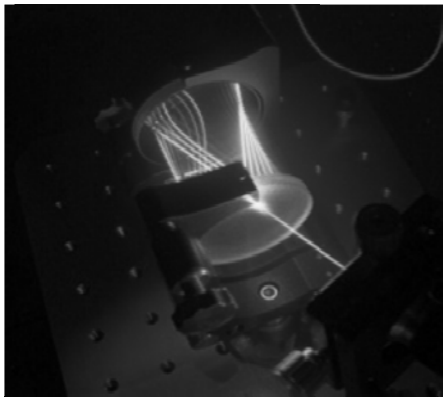

Figure 3.4: Photo of the Harvard Herriott Hygrometer in operation with its red alignment laser.

spurious water to the total absorption measurement. To that end, Drierite was placed in the vessel to remove as much moisture as possible.

The SPV was designed to be sealed and maintain 1 atm pressure so as to prevent moist air from entering the vessel during flight; however during the MACPEX campaign we found a leak in the SPV which caused its pressure to follow atmospheric pressure. This leak allowed moist air to enter the vessel during descent of the aircraft, compromising the accuracy of the HHH measurement during the second half of each flight (this issue is discussed in greater detail in Section 3.5). Additionally, laboratory tests after the mission (which are described in greater detail in Section 3.4) showed that the Drierite did not sufficiently remove water from the SPV and a signal comparable ~0.5 ppmv of H_2O was caused by water in the vessel. We used laboratory calibrations to account for this water signal in the MACPEX flight data. However, we plan to redesign the SPV before the next HHH field campaign to avoid the need for this empirically derived adjustment. An active purge of dry air will be added to the SPV, and it will be made airtight such that it can maintain 1 atm pressure.

The HHH Herriott cell uses a red laser for initial alignment as shown in Figure 3.4; the red laser is fiber-coupled into the cell such that the red and infrared lasers can be interchanged without disturbing the alignment optics. The number of spots produced on the mirrors is counted

both in the red and infrared to be assured of the correct alignment. A key benefit of a Herriott cell that uses a single hole for both input and output beams is that it is insensitive to small misalignments. The cell will only support specific alignments with discrete numbers of passes through the cell. If the alignment were to change in flight (due to contraction of the mirror mounts with temperature, etc.) it could only move from one spot pattern to another by transitioning through a pattern with no exit beam – this would be clearly visible as a zero power output at the detector. Additionally, the new spot pattern would show a discrete change in laser power (at least 6 more or fewer passes between the mirrors). This provides confidence that our water vapor calculation uses the correct number of laser passes in the cell during flight and therefore the correct absorption pathlength.

3.2.2 Inlet and Flow System

During the MACPEX campaign the HHH instrument was flown in the left spearpod of NASA's WB-57 aircraft in combination with the Harvard Lyman-α hygrometer. The combined instrument and ducting are shown in Figure 3.1. An 8.9 x 10.2 cm composite rectangular duct serves as the primary ram air inlet; it extends forward of the spearpod so as to sample air unperturbed by the aircraft or the wing. The HHH mirrors are embedded in and flush with the walls of the primary inlet; a pitot tube connected to a baratron (MKS, part 722A) and two 1 kΩ thermistors are positioned in the flow tube directly behind the mirrors to measure the static pressure and temperature. The region downstream of the HHH axis is unchanged from the design of the previous Lyman-α instrument [*Weinstock et al*., 1994]. A 2" square secondary duct samples the laminar core of the primary flow, while a bypass duct brings the remainder of the primary flow to the exhaust port. The secondary duct directs the flow through an

aerodynamically designed light trap to exclude solar scatter, and on to the Lyman-α detection axis before joining with the bypass duct and exiting through the exhaust port on the lower right side of the spearpod.

In designing the flow system, there are two requirements essential to obtaining accurate water vapor measurements: minimizing potential water sources from surfaces and dead volumes, and maintaining constant pressure and temperature across the Herriott cell. To accomplish the first, the mirrors embedded in the walls of the primary duct were positioned as close to the intake as possible to minimize the upstream surface area which could potentially shed water. The mirror hole is purged lightly with dry air to flush out the dead volume and prevent the accumulation of water. To accomplish the second requirement, the duct design was modeled using fully 3-D computational fluid dynamics (CFD) simulations to examine the temperature and pressure gradients in the duct. The study motivated our choice of inlet profile by demonstrating that a narrow inlet leads to smaller temperature gradients within the duct. The study also showed that gradients of ~1^{o}C/cm and 1.4 mbar/cm exist across the first 11 cm of the duct, but decrease to gradients of only 0.13^{o}C/cm and 0.066 mbar/cm farther than 11 cm down the duct. Therefore, balancing the first and second requirements led to positioning the front edge of the HHH mirrors 11 cm from the front of the duct, as far forward as possible while avoiding the temperature and pressure gradients directly after the inlet. Placed before and after the mirrors are two rings each holding 7 thermistors evenly spaced across duct; in flight these thermistors measured temperature changes of no more than 1^{o}C across the 7.6 cm-diameter mirrors, verifying the above analysis. Such a temperature gradient could produce at most a 0.02 ppmv error in calculated water vapor in the Herriott cell. The thermistor ring in front of the HHH mirrors was removed after the first three flights to eliminate the potential for water shedding from the

thermistors to affect the HHH measurement. We are therefore confident that water shed from surfaces or dead volumes is minimal, and that no temperature or pressure gradients that could interfere with accurate water vapor measurements are present at the HHH mirrors.

3.2.3 Data acquisition system

The primary electrical systems for HHH are the laser driver (waveform generator), detector/pre-amplifier, scalable signal processing (SSP) board, and flight computer. The laser driver is designed and built in house; it produces a voltage waveform which the voltage-to-current (VtoI) converter proportionally transforms to current. The driver has a programmable frequency scan and scan rate, and safeguards that prevent laser over current and over temperature conditions. A constant period sawtooth current ramp is applied to the laser to scan the output region from 60-90 mA at a rate of 1000 scans per second; this corresponds to scanning from 7181.61-7180.92 cm^{-1}. The waveform generator achieves remarkably low noise compared to its commercial counterparts through the use of a pair of digital to analog converters whose outputs are summed to produce a truly analog voltage waveform while maintaining programmability in voltage and time. The duty cycle is 95%, with a zero value acquired before and after each waveform scan, which is necessary for an absolute 0 V reference level.

All laser signals (Herriott cell, etalon, and background) are detected by InGaAs photodetectors, which operate at room temperature. The gain is adjustable and the size is on the scale of a quarter. Pre-amplification of each signal is achieved via in-house design; the detector and pre-amp are mounted together on a 1 x 1 in PC board. The Scalable Signal Processing (SSP) board couples a differential 16-bit, 100 MHz analog to digital converter with a field programmable gate array (FPGA) based signal-processing engine, allowing for digitized spectra

to be averaged and reduced before storage on the flight computer. The SSP averages the 52600 points per scan down to 1050 points, then coadds 799 spectra to produce 1 "raw" spectrum which is then recorded by the flight computer every 0.799 sec. This reduces the storage requirements on the flight computer thereby reducing its size and weight while increasing the number of possible recorded channels. The signal processing and Ethernet communication is handled by the onboard Virtex-4 SX35 FPGA using the embedded microblaze microprocessor. The clock on the SSP is used to trigger the waveform generator so that data acquisition is synchronized with the tuning of the laser.

3.3 Data Analysis and Spectral Fitting Algorithm

The water vapor concentration is calculated from the Herriott cell spectrum by applying the Beer-Lambert law relating the transmitted light intensity to the concentration of the absorbing species:

$$-\ln\left(I/I_o\right) = c * k(\nu) * l \tag{3.1}$$

where I and I_o represent the transmitted and incident light intensity, k is the absorption coefficient, l is the pathlength, and c is the water vapor number density. The background spectrum, I_o, is determined from a polynomial fit to the Herriott cell baseline. The absorption coefficient, k, is a function of the spectral line intensity, $S_{\eta\eta'}$, the Voigt lineshape function, V, and the Lorentizian and Doppler half-widths, γ_L and γ_d:

$$k(\nu) = \frac{S_{\eta\eta'}}{\gamma_d}\sqrt{\frac{ln2}{\pi}}V\left(\nu, \nu_{\eta\eta'}, \gamma_L/\gamma_d\right) \tag{3.2}$$

The Voigt lineshape function, *V*, is calculated by an empirical convolution of the Gaussian and Lorentzian lineshapes [*Shippony and Read*, 2003; *Liu et al*., 2001]. Because the sample is at low pressure and low mixing ratio, we ignore the effect of self-broadening on the Lorentzian width. The line intensity, $S_{\eta\eta'}$, is temperature dependent and is given by:

$$S_{\eta\eta'}(T) = S_{\eta\eta'}(T_{ref})\frac{Q(T_{ref})}{Q(T)}\frac{\exp(-c_2E_\eta/T)}{\exp(-c_2E_\eta/T_{ref})}\frac{\left[1-\exp(-c_2\nu_{\eta\eta'}/T)\right]}{\left[1-\exp(-c_2\nu_{\eta\eta'}/T_{ref})\right]} \tag{3.3}$$

and γ_L and γ_d are defined as:

$$\gamma_L(p,T) = \left(\frac{T_{ref}}{T}\right)^n \gamma_{air}p \tag{3.4}$$

$$\gamma_d = \nu_{\eta\eta'}\sqrt{\frac{2kT\ln(2)}{mc^2}} \tag{3.5}$$

The pressure and temperature used in these calculations are measured by the pitot tube and two thermistors located directly behind the HHH mirrors in the flow. The spectral parameters $S_{\eta\eta'}(T_{ref}), E_\eta, \nu_{\eta\eta'}, \gamma_{air},$ and n are obtained from the HITRAN database [*Rothman et al.*, 2009]. c_2 is the second radiation constant (hc/k), $Q(T)$ is the total internal partition sum, k is Boltzmann's constant, and c is the speed of light.

The fitting algorithm developed in house uses the empirically fit baseline, observed temperature and pressure, and spectroscopic parameters from HITRAN to fit the measured absorption line to Equation 3.1 and determine the water vapor concentration. The engine of the fitting algorithm uses the Levenberg–Marquardt method from Numerical Recipes in C, modified for C++, in which the concentration and baseline are the only floating parameters.

An example of the fitting process is shown in Figure 3.5 for the flight on 4/20/11 during the MACPEX mission; this spectrum was obtained at 120 torr, -45°C, and 4.8 ppmv H_2O. The

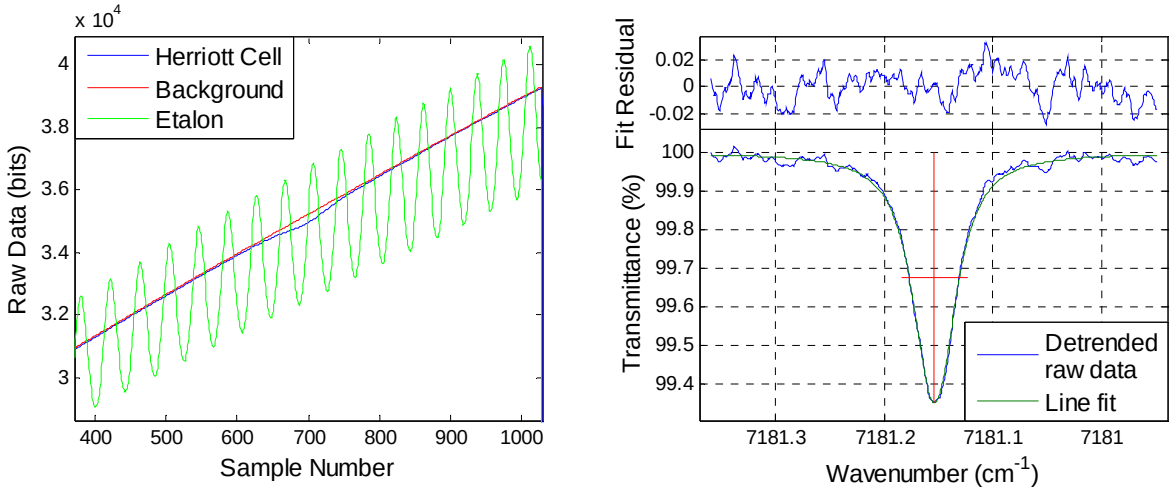

Figure 3.5: Left: A typical spectrum acquired by HHH. Right: The same data as shown to the left, now de-trended from the baseline power curve and fit using a voigt lineshape. The upper plot shows the residual between the raw and fit data.

raw spectra from the Herriott cell, etalon, and background axes are shown in the left panel. Taking the line center to be 7181.1558 cm^{-1}, the fringe spacing of the etalon spectrum along with its free spectral range (FSR) are used to convert the x-axis from sample number to frequency space. The FSR of the etalon (the spacing in wavenumbers of the interference fringes shown in Figure 3.5) is related to the size of the silicon crystal atomic spacing according to:

$$FSR = \frac{1}{2NL} \tag{3.6}$$

where N is the index of refraction of silicon and L is the length of the etalon.

The baseline of the Herriott cell spectrum, with the absorption line removed, is fit with a 3rd order polynomial to obtain the incident light intensity. The right panel of Figure 3.5 shows in blue the absorption line, detrended from the baseline curve and converted to frequency space. The empirical fit to the line is shown in green and the residuals between the observed and fit data are shown in the top panel. As a check, the baseline can also be fit with polynomials of different orders, or by combining a linear fit to the baseline with the background cell spectrum (which accounts for laser power fluctuations). Figure 3.6 (left) shows empirical fits to the line using 3rd

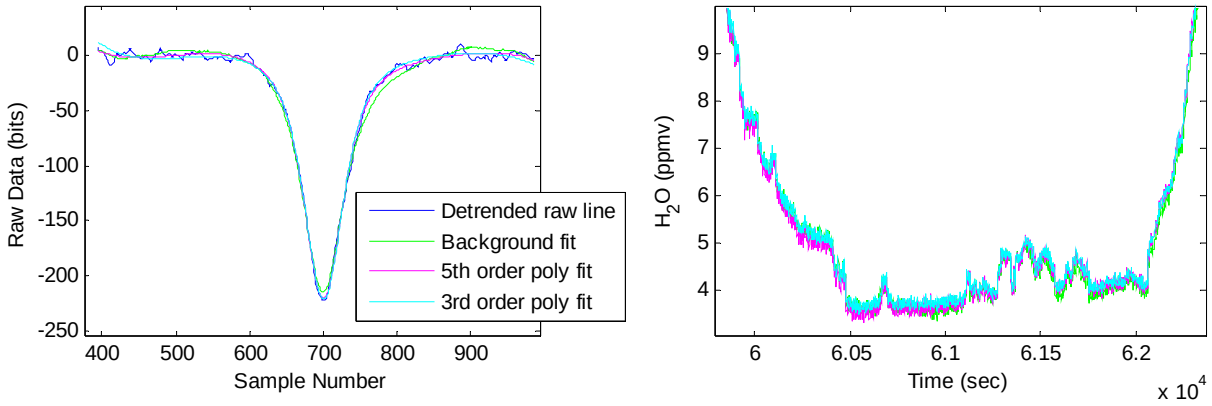

Figure 3.6: Left: A typical spectrum fit using the background cell, and using a 5th and 3rd order polynomial fit to the Herriott cell baseline. Right: Water vapor mixing ratio calculated for the flight of 4/20/11 using the above baseline fits.

and 5th order polynomials to fit the baseline, as well as the sum of the observed background cell spectrum and a linear fit to the baseline. These methods typically agree to within 1%; the water vapor concentration calculated using each method for the flight of 4/20/11 is shown in Figure 3.6 (right).

3.4 Calibration of the Instrument

The HHH instrument is calibrated in the laboratory by comparison with multiple standards under conditions which replicate the flight environment as closely as possible. Though the accuracy of the HHH instrument is theoretically tied only to spectroscopic parameters from the HITRAN database, in practice any complex field instrument must be validated in the laboratory to constrain possible instrumental artifacts that could affect the measurement. We seek to constrain uncertainties in the HHH measurement which arise from: i) errors in the HITRAN database, ii) uncertainties in the instrument function such as distortion of absorption features due to current noise, iii) nonwhite components in the baseline noise, and iv) the unknown water concentration in the laser pathlength outside the Herriott cell. The calibration

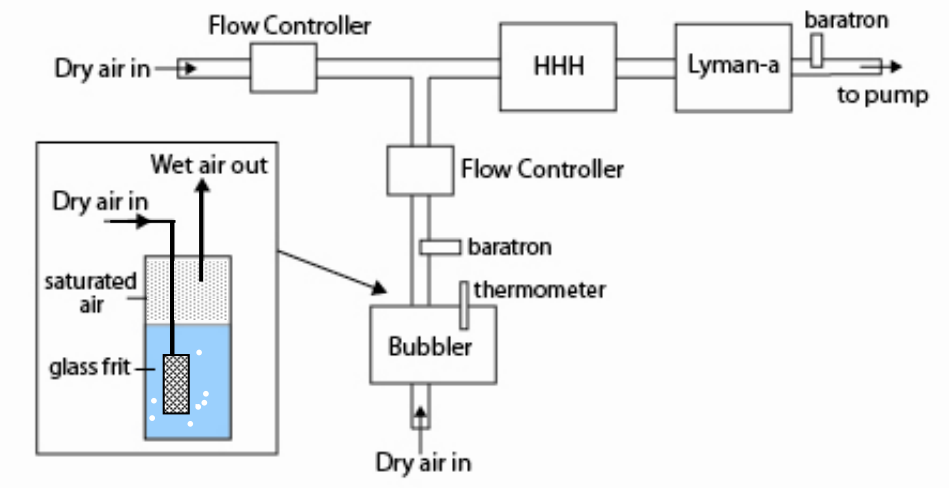

Figure 3.7: Schematic of HWV calibration bench. Controlled quantities of saturated air are combined with a flow of dry air which is directed to both the HHH and Lyman-α detection axes.

of HHH differs from that of instruments such as Lyman-α and JLH in that its sensitivity to water vapor is set by spectroscopic parameters, and calibration serves to verify that spectroscopy. On the other hand, the sensitivity of Lyman-α and JLH to water vapor can only be determined empirically via calibration and is more likely to drift over time.

In the calibration of a flight instrument, it is essential to mimic field sampling conditions as closely as possible in order to be assured that laboratory results are applicable to flight data. A key benefit of our ducted sampling design is that the instrument and its duct can be integrated into a laboratory calibration system with no changes to the axis itself and under conditions very close to those in flight. The instrument and its duct are adapted to a two-inch square flow tube with a dry air input and an output to a large vacuum pump as shown in Figure 3.7. While it is not possible to reproduce the in-flight flow speeds of ~140-160 m/s in the laboratory, we do produce flow speeds of up to 40 m/s. As a check, we vary the flow speed in the lab to demonstrate that water vapor measured by the instrument is not dependant on flow speed. Pressures observed in the field are easily achieved by varying the input air flow and throttling the exit valve to the vacuum pump to vary the velocity of air in the duct. UT/LS temperatures are

produced in the lab by placing the instrument and ducting within a box of insulating foam that is cooled with liquid nitrogen blowoff. We are able to run the instrument in the lab at temperatures down to -50^{o}C.

A two-stage bubbler is used as both a water addition system and a primary standard for comparison with HHH. A small flow of air is brought to water vapor saturation by bubbling it through a glass frit immersed in distilled water in two stages; this flow is combined with a main flow of dry air to produce air with known water vapor concentrations of 1-600 ppmv. The carrier gas is either ultra zero air from AirGas which typically contains 1-3 ppmv H_2O, or nitrogen blowoff from a liquid nitrogen tank with ~0.35 ppmv H_2O. The main flow is set using a 50 standard liter per minute (SLM) MFC flow controller (MKS Instruments); the saturated air flow is set using a 100 standard cubic centimeter per second (SCCM) MFC flow controller. The added water vapor concentration is known to within 5% based on the uncertainty in the temperature and pressure at the bubbler, the flow rates of the two flow controllers adding dry and saturated air, and achievement of 100% saturation of air after the bubbler. As a check, the bubbler system was compared with an absorption measurement at 121.6 nm, where the absorption cross-section has been accurately determined [*Lewis et al*., 1983; *Kley*, 1984] over a ~1 m pathlength along the axis of the duct; they agreed to within 3% from 3 to 300 ppmv H_2O. The bubbler system was also compared with the MBW frostpoint hygrometer (model 373LX, accurate down to a frostpoint of -95°C) used to calibrate the NOAA CIMS instrument, and they agreed to within 2%.

The output of the bubbler is fed to both the HHH and Lyman-α axes and then output to the vacuum pump. HHH was calibrated in combination with Lyman-α both as a secondary check on accuracy and to demonstrate that in-flight agreement is consistent with laboratory

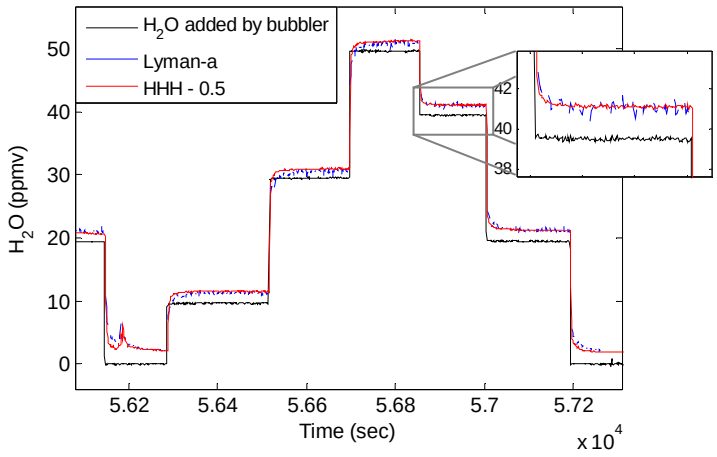

Figure 3.8: Low water laboratory intercomparison between the bubbler, Lyman-α, and HHH.

agreement. HHH and Lyman-α were operated in series so as to provide maximum air flow to the instruments, and were also operated in parallel in order to be assured that no contamination from the front axis affected the rear axis when in series. A calibration run consists of varying the amount of saturated air added from the bubbler system while measuring water vapor with both HHH and Lyman-α. Calibrations were performed at various pressures from 40 torr to 250 torr.

Figure 3.8 shows a comparison of water added from the bubbler to water measured by both instruments. We consistently observed a linear relationship between the water vapor measured by the bubbler and that measured by each instrument, with a slope equal to 1±0.03. This agreement between HHH and the bubbler constrains the potential impact of instrument artifacts or HITRAN uncertainties on the instrument's response to changes in water vapor.

A nonzero intercept between the instruments and the bubbler, in this case an offset with the HHH and Lyman-α measuring higher than the bubbler, is attributed to residual water in the main flow of "dry air" and any water desorbed from the walls of the duct upstream of the detection axis. Because this "dry air" typically contained 1-3 ppmv of water, it was unsuitable for validating the absolute measurement of HHH at low water. Instead, extremely dry (<0.35 ppmv) nitrogen blowoff from a liquid nitrogen dewar was used as a carrier gas to investigate the

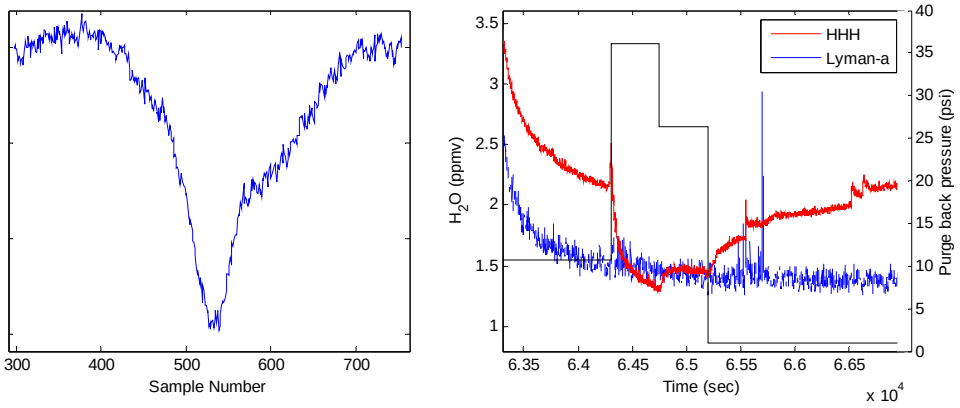

Figure 3.9: Left: HHH spectrum obtained in the laboratory with ~0.4 ppmv H_2O in the duct, showing the superposition of a narrow low-pressure water vapor line from the duct and a broad high-pressure line from the SPV. Right: Water vapor as measured by Lyman-α and HHH with a varying strength purge on the HHH SPV.

possibility of a positive or negative offset. In these tests, Lyman-α measured as low as 0.3 ppmv, constraining the maximum possible offset in that measurement, which is included in the instrument uncertainty for flight measurements. However, HHH showed a distinct water vapor absorption line from the liquid nitrogen blowoff (Figure 3.9, left), indicating that there is non-negligible water in the flow, and the -0.3 ppmv uncertainty is an overestimate.

In these tests at ~0.3 ppmv H_2O, HHH measured 0.5-1 ppmv more water vapor than Lyman-α. Further examination of the spectra obtained by HHH at low water showed that with the flow tube at reduced pressure (~100 torr), the narrow low pressure absorption line had superimposed on it a pressure-broadened absorption line as shown in Figure 3.9 (left). Recall that the laser travels a short path within the signal pressure vessel (SPV) at room pressure before entering the Herriott cell; water in the vessel is the only possible source of a pressure broadened water line. As a further test, a dry N_2 purge of varying strength was applied to the SPV with constant water vapor in the HHH axis; the strength of this purge was correlated with the water vapor concentration measured at the HHH axis as shown in Figure 3.9 (right). These tests clearly demonstrate that the 0.5-1 ppmv positive offset in water vapor measured by HHH

compared to Lyman-α is due to the presence of water in the SPV. Though this effect was slightly variable, our tests concluded that the offset caused by this problem accounts for 0.5±0.5 ppmv of the observed water signal. This result was incorporated into our reported flight data for the MACPEX campaign, with water vapor measured by HHH adjusted by –0.5 ppmv and the uncertainty in this correction factor included in our reported error bars. As stated above, we plan to redesign the SPV before the next flight series of HHH by making it air-tight and adding a purge to dry the vessel. These changes should remove the need for this empirical correction so that in the future the HHH measurement is tied solely to spectroscopic parameters.

The uncertainty in the spectroscopic parameters used from the HITRAN database lead to a combined uncertainty in water vapor concentration of ±10%. The uncertainty in our laboratory calibration system is ±5% in slope based on the parameters outlined above, with a maximum potential offset of -0.3 ppmv based on the lowest water vapor mixing ratio achieved in the lab. The calibrations also showed the need for adjustment of the HHH measurements by -0.5 ±0.5 ppmv. Therefore the accuracy of HHH is constrained more stringently by the laboratory calibration than by the HITRAN parameters, leading to a combined instrument uncertainty of +5% + 0.5 ppmv / -5% - 0.8 ppmv.

3.5 Recent Flight Results

HHH obtained science-quality flight data for the first time in the Mid-latitude Airborne Cirrus Properties Experiment (MACPEX) campaign from Houston, TX, during the spring of 2011. The campaign consisted of two test flights and 14 science flights from 3/27/11 to 4/26/11, with extensive sampling at altitudes from 8.4 to 18.4 km over the southern and midwestern United States and the Gulf of Mexico. HHH obtained water vapor data during the last six

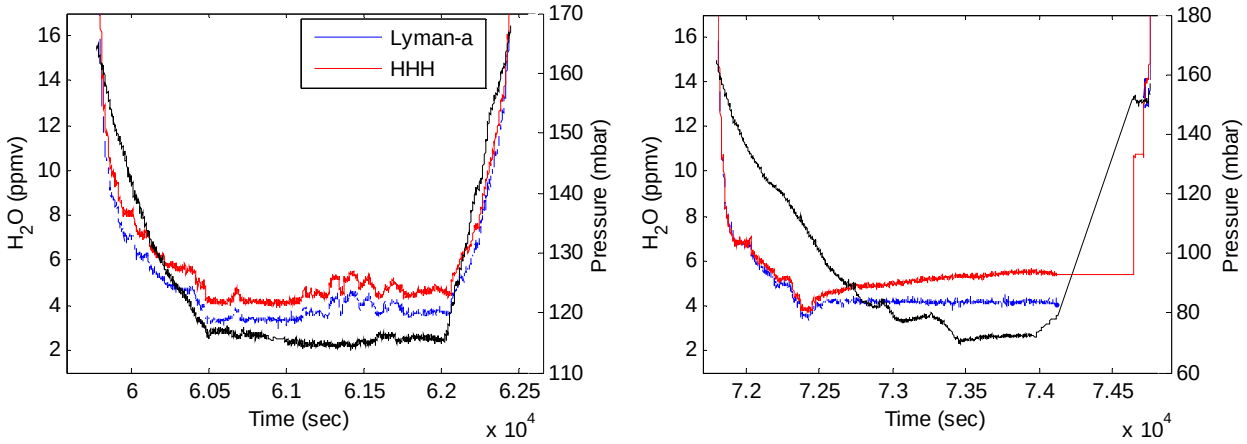

Figure 3.10: Water vapor (blue, red) and atmospheric pressure (black) measured during the 4/20/11 flight. Left: First high altitude leg; notice the consistent offset between Lyman-α and HHH. Right: Second high altitude leg; notice the varying offset between Lyman-α and HHH which correlates with pressure.

science flights from 4/18/11 to 4/26/11. Measurement precision during the MACPEX campaign was 0.1 ppmv for a 1 sec measurement. This is on the order of the precision achieved by the Lyman-α instrument as well as that of JLH, which utilizes second harmonic detection. Reported water vapor concentrations include the –0.5 ppmv adjustment calculated based on the laboratory calibrations described above.

As mentioned in the above, the signal pressure vessel (SPV) was designed to maintain 1 atm pressure, but during the mission, it contained a leak causing it to follow atmospheric pressure. The vessel was sealed containing Drierite the night before each flight, minimizing the water vapor inside at takeoff. During the first ascent of the aircraft and the first high-altitude leg, air would leak out of the vessel to the lower-pressure surroundings, and the SPV would remain dry. However, after the first descent of the aircraft in each flight, ambient air would flow into the vessel and cause the relative humidity in the SPV to change with altitude, such that water vapor as measured by HHH varied with pressure. Figure 3.10 shows that HHH data from the 1st high altitude leg on 4/20/11 has a consistent 0.3 ppmv offset with respect to Lyman-α, while data from the 2nd high altitude leg show a variable 0-1.2 ppmv offset that is correlated with

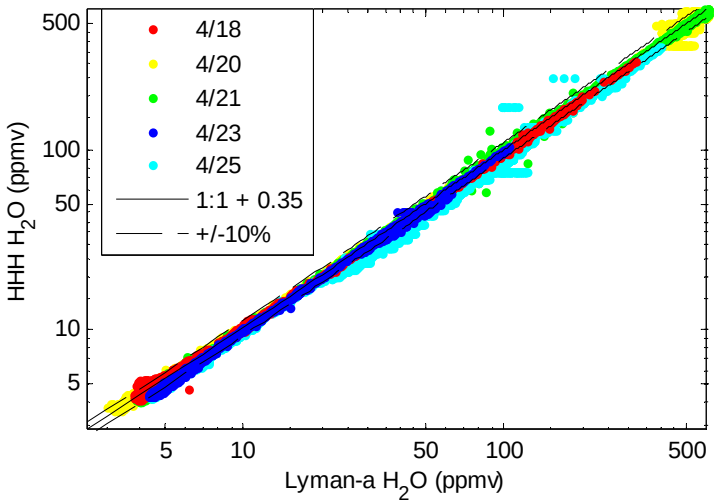

Figure 3.11: H_2O as measured by HHH compared to that measured by Lyman-α for each day that HHH acquired data. Also shown is a 1:1 fit with a 0.35 ppmv offset and ±10% range.

atmospheric pressure. Therefore, only HHH data for the first leg of the flight including the climb and first high altitude portion are reported here, as they do not show this adverse response to pressure changes. However, the very consistent relationship between HHH and Lyman-α during the first leg of each flight provides confidence that the SPV leak did not affect those data.

During the campaign, 8 independent in situ water vapor instruments logged data on board the WB-57. Of these, Lyman-α, ALIAS, ULH, FISH, and the NOAA Chemical Ionization Mass Spectrometer (CIMS) [*Thornberry et al.*, 2011] measured simultaneously with HHH over a similar range of water vapor concentrations. Additionally, the CFH and FPH balloon-borne frostpoint hygrometers were alternately flown near the WB-57 flight path on six of the flights, with three balloon flights coinciding with HHH measurements. This extensive water vapor inter-comparison provided the opportunity to both validate the accuracy of HHH against other tested field instruments and to address long-standing discrepancies among in situ water vapor instruments. Figure 3.11 shows HHH vs. Lyman-α water vapor for the flights of 4/18, 4/20, 4/21, 4/23, and 4/25. HHH agreed with Lyman-α to within 1% on average, with the relationship HHH=0.99*Lyman-α + 0.3 ppmv. Nearly all flight data fell within ±10% agreement. Note that

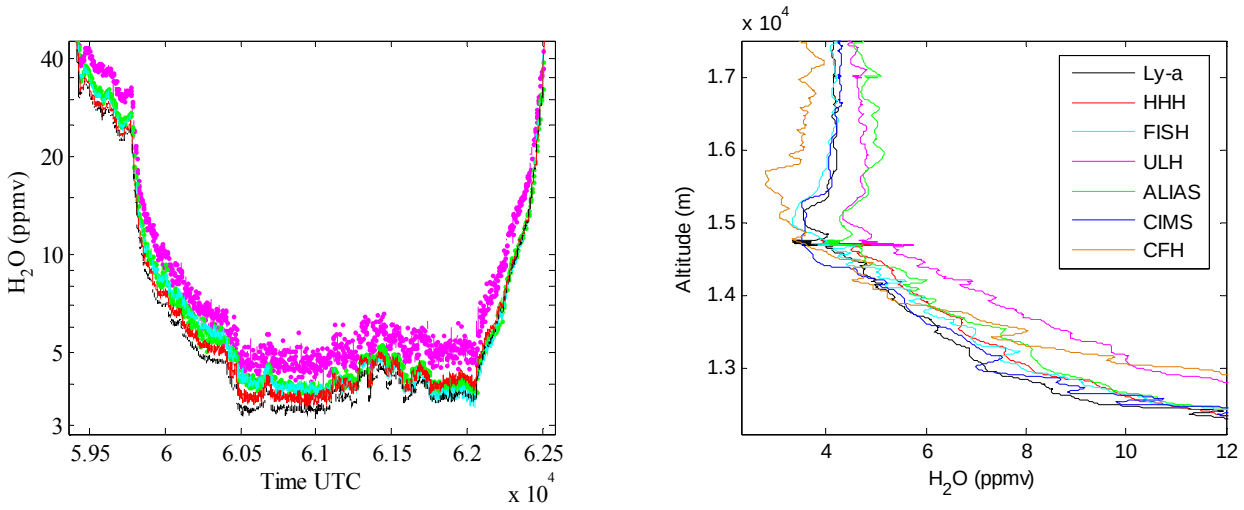

Figure 3.12: H_2O as measured by all available instruments on 4/20/11. Left: H_2O as a function of time for all WB-57 instruments. Right: H_2O as a function of altitude for all WB-57 instruments and the CFH balloon-borne frostpoint hygrometer.

HHH samples across the entire duct in the space between the mirrors, while Lyman-α samples only the core of the flow; therefore the agreement between Lyman-α and HHH limits the potential impact that water desorbing from the duct walls could have had on HHH.

Figure 3.12 (left) shows a time series of water vapor measurements on 4/20/11 for Lyman-α, HHH, FISH, ULH, and ALIAS. Note that water vapor measured by FISH and ALIAS, pallet total water instruments, decreases with respect to the other instruments over time after the primary ascent due to outgassing from surfaces. Figure 3.12 (right) shows water vapor as measured by all water vapor instruments with altitude including the balloon-borne CFH, while Table 3.1 lists the agreement among the instruments over the entire mission along with their uncertainties. CFH and FISH continue to measure slightly lower than the other instruments at low water, but differed from Lyman-α by only ~0.4 ppmv, compared to the 1-2 ppmv differences that had been observed in past flight comparisons. Lyman-α, HHH, FISH, CIMS, and CFH agreed within their stated error bars for >80% of the MACPEX data. The agreement of ALIAS and ULH with Lyman-α was outside the combined uncertainty of the instruments, with

Table 3.1: Average agreement of water vapor instruments during the MACPEX campaign.

	Agreement: Slope	Low Water Offset	Uncertainty	Precision
Lyman-α	-	-	5% - 0.3 ppmv	2%
HHH	0.99	+0.35	5% + .5 ppmv - .8 ppmv	2%
FISH	1.06	-0.32	6% ± .15 ppmv	2%
ULH	0.66	+0.2	15%	5%
ALIAS	1.16	+0.84	5% + 1 ppmv	3%
CIMS	1.03	+0.14	10%	2%
CFH/FPH	-	-0.4	10%	4%/0.5%

ALIAS differing by 16% + 0.84 ppmv, and ULH differing by 44%. Overall, the agreement of 5 out of 7 instruments in measured water vapor to within 6% and 0.7 ppmv at low water shows marked improvement from past campaigns which consistently showed 1-2 ppmv differences.

As each instrument was somehow altered or at least re-calibrated between deployments, it is not possible to attribute this improvement to any specific changes in one or more instruments. However, because the changes made in each instrument were the result of work to better understand their operation and sources of uncertainty, we expect that the agreement is representative of improvement in instrument accuracy across the field as a whole. Although these results cannot improve our knowledge of past stratospheric water vapor levels, they represent an improvement in the assessment of current and hopefully future stratospheric water vapor concentration.

3.6 Conclusions

Water vapor measurements in the upper troposphere and lower stratosphere have historically shown disagreements of up to 2 ppmv, well outside the stated uncertainty of each instrument and the accuracy necessary to understand water vapor transport mechanisms and trends. These discrepancies have prompted the need for new hygrometers with improved

accuracy and high precision; to that end our lab has developed the Harvard Herriott Hygrometer, the first direct absorption tunable diode laser (TDL) instrument to measure water vapor in the UT/LS. HHH measures water vapor via infrared absorption in a multi-pass Herriott cell at concentrations from 1-600 ppmv. The measured absorption line is fit using a Voigt lineshape, and the absorption depth compared to the baseline is used to calculate water vapor number density. The instrument achieves high precision of 0.1 ppmv for 1 sec data, while its direct absorption technique avoids the limitations in accuracy associated with second harmonic detection and allows for water vapor to be calculated solely based on spectroscopic parameters in the HITRAN database.

Laboratory calibrations with two independent standards, the vapor pressure of liquid water over a bubbler, and UV absorption at 121.6 nm, were used to validate the accuracy the instrument and constrain the impact of possible instrument artifacts; both methods showed agreement with HHH to within 3%. A positive bias of ~0.5 ppmv was demonstrated in laboratory calibrations due to water in the laser path outside of the Herriott cell, and has been accounted for in the flight data. Modifications to the instrument prior to its next flight campaign should remove this bias and the need for a laboratory correction. Based on the laboratory calibration, we calculate 1-sigma uncertainty associated with the HHH measurement to be +5% + 0.5 ppmv / -5% - 0.8 ppmv. Our planned improvements to the instrument should notably reduce this uncertainty in its next field campaign.

HHH flew its first science mission as part of the MACPEX campaign in April, 2011, in combination with the Harvard Lyman-α hygrometer in the left spearpod of NASA's WB-57 aircraft. In the future, HHH could also be operated independently from Lyman-α as a smaller, lighter instrument for use on other aircraft platforms such as the Global Hawk. During

MACPEX, HHH successfully measured water vapor at concentrations from 3.5-600 ppmv in the upper troposphere and lower stratosphere. HHH and Lyman-α, measuring independently but under the same sampling conditions, agreed to within 1% + 0.3 ppmv on average over the entire campaign. Unlike the past disagreement of Harvard Water Vapor and JLH by up to 1.5 ppmv, HHH has shown that the Lyman-α and TDL techniques can agree well in flight. Additionally, the Lyman-α, HHH, FISH, CIMS, and CFH instruments all agreed to within their stated uncertainties during the campaign, and to within 0.7 ppmv at low water. This much improved agreement among the suite of water vapor instruments will enhance the ability of the field to detect stratospheric water vapor trends and to understand the mechanisms that dictate the phase and distribution of stratospheric water.

References

Kley, D. (1984), Ly(α) Absorption Cross-Section of H_2O and O_2, *J. Atmos. Chem., 2*, 203-210.

Lewis, B. R., I. M. Vardavas, and J. H. Carver (1983), The Aeronomic Dissociation of Water Vapor by Solar H Lyman α Radiation, J. Geophys. Res., 88, 4935-4940.

Liu, Y. Y., J. L. Lin, G. M. Huang, Y. Q. Guo, and C. X. Duan (2001), Simple empirical analytical approximation to the Voigt profile, *J. Opt. Soc. Am. B, 18*, 666-672.

May, R. D. (1998), Open-path, near-infrared tunable diode laser spectrometer for atmospheric measurements of H_2O, *J. Geophys. Res., 103*, D15, 19161-19172.

Reid, J. and D. Labrie (1981), Second-harmonic detection with tunable diode lasers – Comparison of experiment and theory, *Appl. Phys. B., 26*, 203-210.

Rothman, L. S., I. E. Gordon, A. Barbe, D. C. Benner, P. F. Bernath, M. Birk, V. Boudon, L. R. Brown, A. Campargue, J.-P. Champion, K. Chance, et al. (2009), The HITRAN 2008 molecular spectroscopic database, *J. Quant. Spectrosc. Radiat. Transf., 110*, 533-572.

Shippony, Z. and W. G. Read (2003), A correction to a highly accurate Voigt function algorithm, *J. Quant. Spectrosc. Radiat. Transfer, 78*, 255-255.

Solomon, S., K. H. Rosenlof, R. W. Portmann, J. S. Daniel, S. M. Davis, T. J. Sanford, and G. K. Plattner (2010), Contributions of Stratospheric Water Vapor to Decadal Changes in the Rate of Global Warming, *Science*, *327*(5970), 1219-1223.

Thornberry, T., A. W. Rollins, R.-S. Gao, D. W. Fahey, L. A.Watts (2011), NOAA ESRL Chemical Sciences Division, NOAA Water Vapor CIMS (CIMS-H2O), unpublished results.

Webster, C. R., R. D. May, C. A. Trimble, R. G. Chave, and J. Kendall (1994), Aircraft laser infrared absorption spectrometer (ALIAS) for in situ atmospheric measurements of HCl, N2O, CH4, NO2, and HNO3, Appl. Opt., 33, 454–472.

Weinstock, E. M., E. J. Hintsa, A. E. Dessler, J. F. Oliver, N. L. Hazen, J. N. Desmusz, N. T. Allen, L. B. Lapson, and J. G. Anderson (1994), New fast response photofragment fluorescence hygrometer for use on the NASA ER-2 and the Perseus remotely piloted aircraft, *Rev. Sci. Instrum., 65*, 3544–3554.

Weinstock, E. M., J. B. Smith, D. S. Sayres, J. V. Pittman, J. R. Spackman, E. J. Hintsa, T. F. Hanisco, E. J. Moyer, J. M. St. Clair, M. R. Sargent, and J. G. Anderson (2009), Validation of the Harvard Lyman-a in situ water vapor instrument: Implications for the mechanisms that control stratospheric water vapor, *J. Geophys. Res., 114*, D23301, doi:10.1029/2009JD012427.

Zöger, M., A. Afchine, N. Eicke, M.-T. Gerhards, E. Klein, D. S. McKenna, U. Mörschel, U. Schmidt, V. Tan, F. Tuitjer, T. Woyke, and C. Schiller: Fast in situ stratospheric hygrometers: A new family of balloonborne and airborne Lyman-α photofragment fluorescence hygrometers, J. Geophys. Res., 104, 1807–1816, 1999.

Chapter 4

Transport in the Tropical Tropopause Layer: An In Situ Measurement Perspective

4.1 Introduction

Stratospheric water vapor plays a key role in the climate system, both as a strong greenhouse gas contributing to radiative forcing, and through its role in stratospheric ozone destruction. In order to predict future stratospheric humidity in the context of a warming climate, it is critical to understand the complex processes which control the amount of water entering the stratosphere. Recall from Chapter 1 that the concentration of water vapor in the stratosphere is set by both the temperature history of air parcels crossing the tropical tropopause and presence of convection above the tropopause, which can moisten the stratosphere through the evaporation of lofted ice particles. Transport pathways in the tropical tropopause layer (TTL) are therefore key to understanding how water enters the stratosphere, and how that transport may change in the future.

We define the TTL as the region in the tropics between the level of main convective outflow at ~355 K (150 hPa) and the highest level at which convection has been observed, ~425 K (70 hPa). The cold point tropopause is located within the layer at ~380 K (100 hPa). This

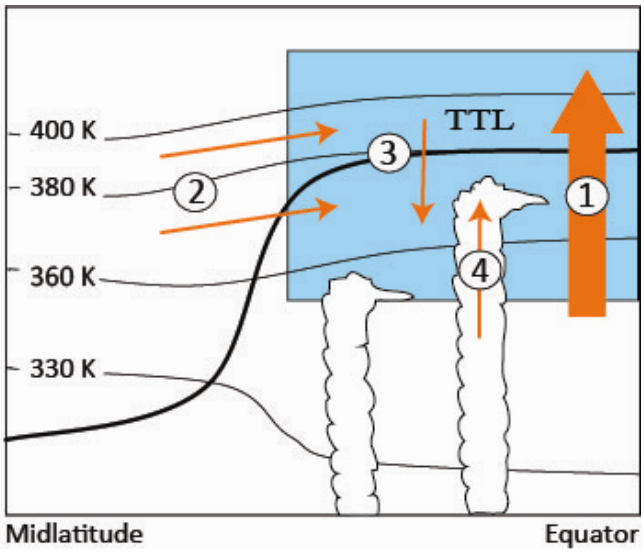

Figure 4.1: Isentropic surfaces in the TTL as a function of latitude and altitude. The transport pathways considered in this study are indicated: (1) Slow Ascent; (2) Midlatitude Stratosphere; (3) Descent; (4) Convection.

work will focus on four specific pathways that transport air into the TTL (Figure 4.1): (1) Slow ascent of tropical tropospheric air; (2) Equatorward isentropic transport from the midlatitude lowermost stratosphere; (3) Descent within the TTL coupled to convection; (4) Convective injection from the tropical troposphere. Slow ascent of free tropospheric air from the level of main convective outflow at 355 K into the stratosphere is driven by radiative heating in combination with the wave-driven Brewer-Dobson circulation, and has long been considered the dominant transport mode in the TTL [*Fuegistaler et al*., 2009]. Isentropic transport from the midlatitude lowermost stratosphere has also been shown to be a significant source of air in the TTL; air masses with high stratospheric content have been identified in the TTL based on elevated levels of O_3 and HCl [*Folkins et al*., 1999; *Durry et al*., 2006; *Marcy et al*., 2007]. Convection also has the potential to strongly impact tracer concentrations in the TTL. Although the majority of convection detrains below the TTL, convection penetrating into the TTL and occasionally above the tropopause has been repeatedly observed [*Khaykin et al*., 2009; de *Reus et al*., 2009]. Convection can lead to descent of air in the TTL when cold convective outflow

mixes with surrounding air before descending back to its level of neutral buoyancy [*Sherwood and Dessler*, 2001]. Descent can also accompany convection due to gravitational loading and evaporative cooling of condensed water. *Donner et al*. [2007] showed that convective parameterizations which include these mesoscale updrafts and downdrafts better reproduce profiles of Radon-222 and CH_3I, tracers of convective mass transport, in a coupled climate model.

Determining the relative importance of these transport pathways is essential to understanding the control of stratospheric humidity and its response to a changing climate. The amount of convection which penetrates above the tropopause determines the impact of ice lofting on hydrating the tropical stratosphere. In addition, the temperature structure of the TTL is very sensitive to the concentration of ozone, which is highly affected by the amount of isentropic transport from the midlatitude stratosphere. Ozone strongly absorbs short-wave radiation to warm the TTL and tropopause, playing an important role in determining the amount of dehydration which takes place in the TTL [*Marcy et al*., 2007]. However, the large variations in O_3 concentrations at tropopause levels are not simulated well in climate models, preventing them from reproducing trends in tropopause temperatures [*Gettelman et al*., 2009]. Changes in the transport of ozone-rich air from the extra-tropics into the TTL, or changes in the composition of the extra-tropical lowermost stratosphere, will affect the thermal structure of the TTL and therefore the amount of water vapor entering the stratosphere.

Many past studies have demonstrated the importance of the above transport pathways, but fewer have attempted to quantify the relative impact each has on the composition of the TTL. Studies examining the influence of convection on the composition of the TTL show that its impact is significant, though they disagree on the magnitude of convective influence, particularly

Table 4.1: Summary of literature quantifying the impact of convection in the TTL as a function of altitude and season.

	Park et al.	*Dessler et al.*	*Hong et al.*	*Massie et al.*
Method	Back trajectory model	CO/O_3 obs. / Transport model	MODIS cloud obs.	CALIPSO cloud obs.
Convection 370 K	30%	60%	6-8%	-
Convection 380 K	15%	<5%	0%	15-20%
Convection 400 K	10%	-	0%	0-10%
Seasonal max	< 380 K: Summer > 380 K: Equal	-	-	Equal

Table 4.2: Summary of literature quantifying the impact of transport from the midlatitude stratosphere as a function of altitude and season.

	Ploeger et al.	*Homan et al.*	*Konopka et al.*	*Sayres et al.*
Stratospheric input	TTL ave: 50% JJA 25% DJF	JJA: 15%, 380 K 30%, 390 K	-	-
Seasonal max	Summer		Summer	Winter

as a function of altitude; past results on the subject are summarized in Table 4.1. *Dessler* [2002] used simultaneous in situ measurements of CO and O_3 with a 1-dimensional transport model to determine the convective influence below 380 K in the wintertime TTL, finding that 60% of the air at the 380 K surface detrained above 370 K, and that 30% of the air detrained above 375 K. *Hong et al*. [2007] used data from the MODIS instruments aboard the *Terra* and *Aqua* satellites to show that 6-8% of the tropics by area has convection penetrating the TTL; they observed convection in the lower TTL only, with no convection above 380K. The HIRDLS and CALIPSO satellite-borne experiments observed on average 15-20% cloud frequency at 380 K and 5-10% cloud frequency at 390 K in the tropics [*Massie et al*., 2010]. *Park et al*. [2007, 2010] used a back trajectory analysis with a convective influence model to quantify the impact of convection on the air sampled during the TC4 and CR-AVE campaigns. They found that 30% of the air was convectively influenced at 370 K, with up to 15% convectively influenced at 400 K. Seasonal differences in convection are also of interest. CALIPSO cloud observations show greater cloud frequency at 90 hPa in the winter than in the summer [*Massie et al*., 2010].

However, after converting from pressure coordinates to potential temperature, CALIPSO data show approximately equal convection at 380 K (near the tropopause) in both seasons. The back trajectory analysis of *Park et al*. [2007, 2010] shows more convection below the tropopause in the summer, and similar amounts of convection above the tropopause in both seasons. Overall, there is little agreement on the extent of convective influence in the TTL, and comparison of various studies is complicated by the large geographical and temporal variations in convection.

The extent of transport into the TTL from the midlatitude stratosphere is also a source of debate. *Marcy et al.* [2007] determined that 60-90% of HCl at the top of the TTL is stratospheric in origin based on in situ observations in the wintertime TTL. *Homan et al*. [2010] used summertime N_2O measurements over Africa to calculate that 30% of air at 390K and 10-20% of air from 370-380 K is of stratospheric origin. A back trajectory analysis performed by *Ploeger et al*. [2010] showed that 20-25% of TTL trajectories reach poleward of 30^o in the winter, compared to 35-50% in the summer. *Konopka et al*. [2010] used a chemical Lagrangian model of the stratosphere to show that global average mixing from midlatitudes above 380 K is greatest during the northern hemisphere summer, with the difference driven by the Asian monsoon anticyclone. On the other hand, back trajectory analyses by *Sayres et al*. [2010] and *James and Legras* [2009] initiated over Costa Rica indicated that mixing from midlatitudes is greater in the winter than in the summer. These results are summarized in Table 4.2.

Most of the studies discussed above model either slow ascent plus convection or slow ascent plus in-mixing from the midlatitude stratosphere, but not all three together. Here, we use simultaneous in situ measurements over Costa Rica of six chemical tracers, O_3, CO_2, CO, HCl, H_2O, and HDO, in the framework of a simple box model to quantify the contributions of each of these pathways to transport in the TTL. The primary goals of this work are to identify and

quantify the dominant sources of air in the tropical tropopause layer during winter and summer, and to quantify the impact of convection and in-mixing from the stratosphere as a function of altitude.

4.2 Observations

Tracer mixing ratios were measured in situ aboard NASA's WB-57 research aircraft in the upper troposphere and lower stratosphere during the Costa Rica Aura Validation Experiment (CR-AVE) in January-February 2006, and the Tropical Composition, Cloud and Climate Coupling (TC4) campaign in August, 2007. Both campaigns were based out of Alajuela, Costa Rica, at 9.9 ^{o}N latitude, and sampled the TTL from 2 ^{o}S – 11 ^{o}N latitude and from 78 – 92 ^{o}W longitude. In order to quantitatively differentiate between slow ascending, stratospheric, convective, and descending air, we chose to model six measured tracers, O_3, CO_2, CO, HCl, H_2O, and HDO, which each have signatures correlating with specific transport pathways. During these campaigns, O_3 was measured with the NOAA dual-beam UV photometer with an accuracy of ±5% [*Proffitt et al*., 1983]; CO_2 was measured with the Harvard nondispersive infrared absorption analyzer with an accuracy of ±0.2 ppmv [*Daube et al*, 2002]; CO was measured with the NASA/Ames Argus tunable diode laser spectrometer with ±10-15% accuracy [*Loewenstein et al*., 2002] in both missions and with the JPL Aircraft Laser Infrared Absorption Spectrometer (ALIAS) with ± 3% accuracy [*Webster et al.,* 1994] during CR-AVE; HCl was measured with the NOAA chemical ionization mass spectrometer (CIMS) with an accuracy of ± 20% [*Marcy et al*., 2005]; H_2O was measured with the Harvard Lyman-α hygrometer with ±5% accuracy [*Weinstock et al*., 1994]; and HDO was measured with the Harvard ICOS isotope instrument with ±7% accuracy [*Sayres et al*., 2009] in both missions and with the Harvard Hoxotope

instrument with ±15% accuracy [*St. Clair et al*., 2008] during TC4. Rather than the concentration of HDO, the more relevant quantity to this work is the deviation of the water vapor isotopologue ratio from the standard, usually expressed as δD:

$$\delta D = \left[\frac{(HDO/H_2O)_{sample}}{(HDO/H_2O)_{VSMOW}} - 1\right] * 1000$$

Vertical profiles of tracer mixing ratios measured during these campaigns are shown in Figure 4.2.

We chose to include these six tracers in the model because each provides a distinct signature which can help identify the origin of a measured air mass. O_3 and HCl are sensitive to stratospheric input because of the strong contrast between their tropospheric and stratospheric concentrations. The long lifetime and tropospheric seasonal cycle of CO_2 produces a distinct slow ascent profile, deviations from which provide information about both convective and stratospheric air sources. The relatively short chemical lifetime of CO makes it an excellent indicator of convection. H_2O and δD are also sensitive to convective input; cold convective outflow can dehydrate the lower TTL and it can bring enhanced water vapor above the tropopause, particularly in the summer when tropopause temperatures are warmer. During the condensation of liquid water or ice, HDO is preferentially removed into the solid phase, which then sediments out of ascending air. δD is therefore a good tracer of convection, as it decreases when condensation occurs in slowly ascending air, but increases when isotopically heavy ice transported by convection is evaporated into unsaturated air [*Dessler and Sherwood*, 2003]. The transport pathway that most perturbs the concentration of each tracer, along with tracer measurement uncertainty, are shown in Table 4.3.

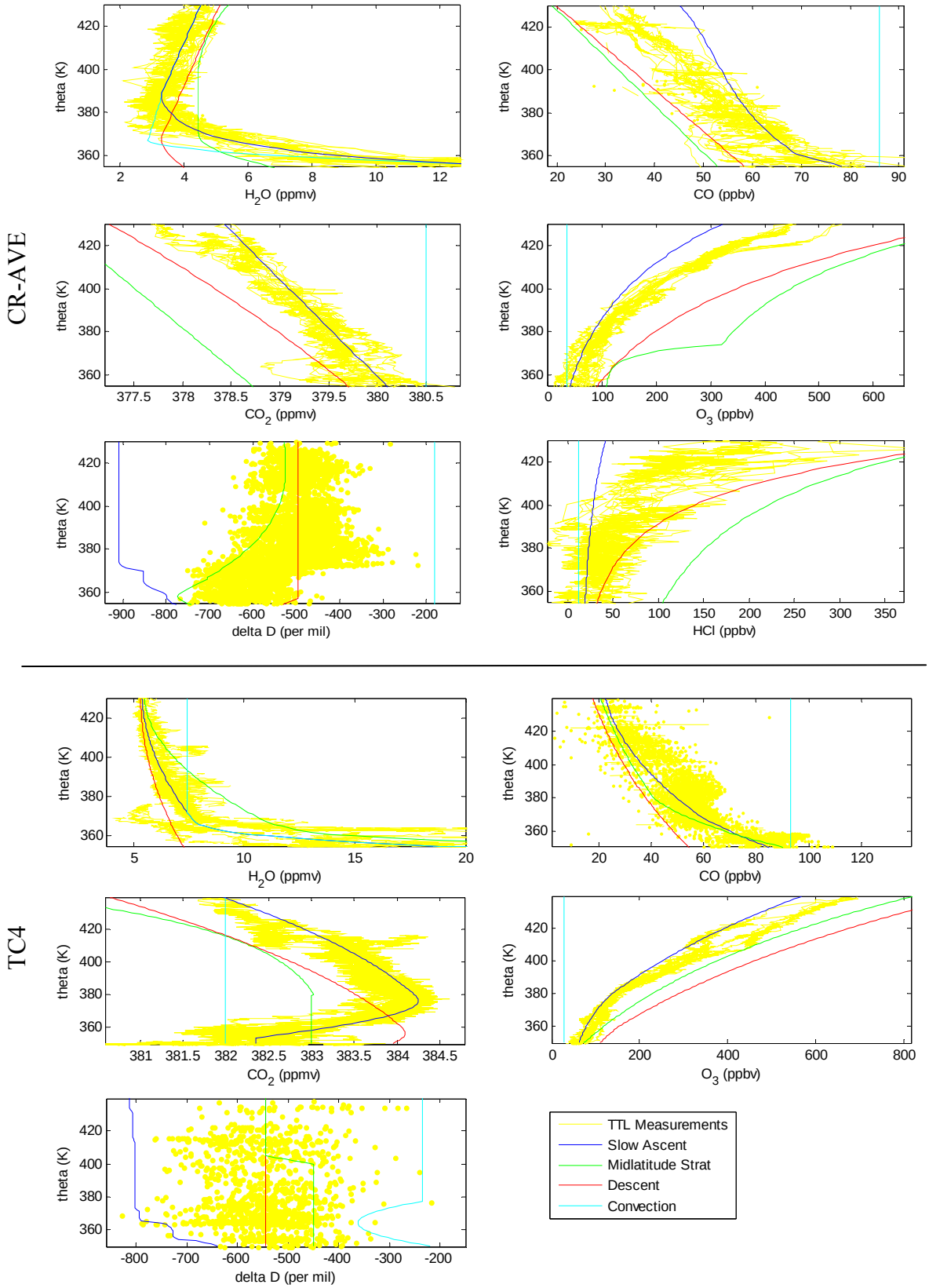

Figure 4.2: Tracer concentration profiles attributed to each source region in the mixing model. Top: winter-time CR-AVE mission. Bottom: summer-time TC4 mission.

Table 4.3: For each tracer used in the model, the transport pathway which most perturbs its concentration, its model and measurement uncertainty, model weight, and measurement availability during CR-AVE (1/30/06-2/9/06) and TC4 (8/5/07, 8/6/07, 8/8/07).

Tracer	*Most Relevant Pathway*	*Measurement Uncertainty*	*Model Uncertainty*	*Weight*	*Availability*
O_3	Midlatitude Strat	5%	Low	4	All
CO_2	Convec/Strat	0.2 ppmv	Med	3	All
CO	Convection	CR-AVE: 3% TC4: 15%	Low	CR-AVE: 4 TC4: 3	CR-AVE, 8/5/07, 8/6/07
HCl	Midlatitude Strat	20%	Low	2	CR-AVE only
H_2O	Convection	5%	TC4 ↑380 K: Low All Other: High	TC4 ↑380 K: 3 All Other: 1	All
HDO	Convection	CR-AVE: 7% TC4: 15%	High	1	CR-AVE, 8/6/07, 8/8/07

4.3 Mixing Model

4.3.1 Source Region Profiles

In order to determine the relative influence of the transport pathways of interest in the TTL, it is first critical to determine the tracer profile that would be observed if each pathway were to act independently. The tracer profiles based on each transport pathway for CR-AVE and TC4 are shown in Figure 4.2; the tracer profile associated with slow ascent is shown in blue, the midlatitude stratosphere in green, descent in red, and convection in cyan. The tracer concentrations measured in the TTL during TC4 and CR-AVE are shown in yellow for comparison. Below, we describe in detail how each of these profiles was determined. We relied where possible on in situ tracer measurements to develop these profiles, and on simple chemical models or studies from the literature when necessary.

The midlatitude stratosphere source profiles were based on observations from the WB-57 aircraft at latitudes higher than 30 ^{o}N during each mission. During both the CR-AVE and TC4 missions, flights near Houston, TX, and ferry flights from Houston to Costa Rica provided midlatitude measurements of the relevant tracers. During TC4, no CO data was obtained above

30°N, so its stratospheric profile was based on MLS satellite observations during the TC4 mission period (http://mls.jpl.nasa.gov/data/v3-3_data_quality_document.pdf) as well as in situ measurements from the Argus instrument during the Crystal-FACE mission in summer, 2002. The tracer profiles associated with descent (as coupled to convection) were determined by shifting the observed TTL profile of each tracer downwards by 20 K in potential temperature. This is consistent with analysis by *Konopka et al.* [2007], which found that convection in the TTL produces mixing on the scale of 20 K.

The convective source profiles for CO, CO_2, O_3, and HCl were based on in situ observations in the troposphere around Costa Rica; the average tropospheric concentration of these species as measured from the DC8 aircraft (during TC4) or during ascent and descent of the WB-57 (during CR-AVE) was assumed to be injected into the TTL at all levels. During TC4, tropospheric CO was measured with the NASA DACOM instrument [*Sachse et al*., 1987], CO_2 with the NASA MACDONNA instrument [*Vay et al.*, 2003], and O_3 was measured with the NASA FastOZ instrument [*Pearson and Stedman*, 1980].

The water vapor and δD convective input profiles are more complex as they are influenced by the atmospheric temperature profile and the history of condensation and evaporation in an air parcel. To determine the H_2O and δD convective profiles, we ran a convective influence model with a simple parameterized model of dehydration along back trajectories, which is described in greater detail by *Sayres et al*. [2010]. Back trajectories are initiated along the flight track during each mission, and driven by GEOS-4 analysis and radiative heating rates. If an air parcel cools along its trajectory, it is assumed that ice is removed to maintain 100% relative humidity, and water vapor and δD are adjusted accordingly; when an air parcel encounters convection, the model hydrates the air to saturation with evaporated ice with a

δD of -100$^{o}/_{oo}$. The model output for the H_2O concentration and δD right after a convective event as a function of altitude was fit to obtain an average convective profile for each season. This profile was used at all potential temperatures for δD and below 380 K for H_2O. Above the cold point tropopause (>380 K), the air is unsaturated in water vapor, meaning that the amount of water injected by convection is determined by both the temperature of the convective outflow and the amount of ice that is lofted into the air parcel. During the summer, the seasonal cycle of tropopause temperatures produces decreasing water vapor above the cold point (the tape recorder signal), such that air injected into the stratosphere at the saturation mixing ratio of the cold point has more water vapor than the surrounding air (Figure 4.2). Therefore, in the summertime TC4 mission we set the water vapor input from convection to be the saturation mixing ratio at the cold point for all levels above 380 K, balancing the competing effects of cold overshooting convection which may inject drier air parcels, and ice lofting which may produce wetter parcels. Though we cannot assume that significant evaporation of ice occurs in every convective plume, we explore the potential impact of ice lofting in Section 4.4 below. During the winter, the tape recorder signal causes the ambient TTL water vapor profile to increase above 380 K. Air injected above 380 K in the winter at the saturation mixing ratio of the cold point would be drier than the surrounding air, while ice lofted above 380 K would bring increased water vapor. These two opposing results of wintertime convection mean that water vapor concentrations do not provide any useful information to the model during CR-AVE regarding convection above 380 K.

The water vapor slow ascent profile was also calculated based on the back trajectory model described above [*Sayres et al*., 2010]. Below 380 K, the slow ascent profile was produced by running the back trajectory model without convection. Above 380 K, the water vapor concentration was determined by the saturation mixing ratio at the tropopause temperature when

the air crossed into the stratosphere. The tropopause temperature history from the previous six months was obtained from *Gettelman et al.* [2009], and we used TTL ascent rates from *Park et al.* [2007; 2010]. The δD slow ascent profile was based on a simple model which takes the δD measured in the free troposphere at 350 K and then follows a Rayleigh distillation for the observed temperature profile, assuming that ice is formed and removed to maintain 100% saturation at temperatures less than 210 K, 120% saturation from 200 – 210 K, and 130% saturation below 200 K [*Smith,* 2011].

The CO slow ascent profile was calculated using a simple chemical model. The main reaction affecting CO concentration in the TTL is chemical loss by reaction with OH:

$$CO + OH \rightarrow prod$$

The model also considered production of CO from CH_4:

$$CH_4 + OH \rightarrow CO + prod$$

Considering the reactions above, the change in concentration of CO at each level was calculated according to:

$$\Delta[CO] = k_{CH4+OH}[OH][CH_4]\Delta t - k_{CO+OH}[OH][CO]\Delta t$$

The average concentration of OH in the TTL was taken to be 7.2×10^5 molecules/cm^3 [*Spavanovsky et al.*, 2000; *Wennberg et al.*, 1998], rate constants were obtained from the JPL 2006 compendium [*Sander et al*., 2006], and the concentration of CH_4 during the mission was measured by the whole air sampler [*Flocke et al.,* 1999]. Initial concentrations of CO at the base of the TTL were determined based on the seasonal cycle in tropospheric CO [*Folkins et al*., 2006], and the ascent rate through the TTL was based on calculations by *Konopka et al*. [2009] and *Park et al*. [2007; 2010]. Notice that the much slower ascent rates during the summer

produce a CO profile with much lower concentrations in the upper TTL during TC4 than during CR-AVE (Figure 4.2).

The HCl slow ascent profile for CR-AVE was also calculated based on a simple chemical model (HCl was not measured during TC4). The only significant chemical source of HCl is:

$$CH_3Cl + OH \rightarrow HCl + prod$$

The production of HCl as a function of height was calculated according to:

$$\Delta[HCl] = k_{CH3Cl+OH}[OH][CH_3Cl]\Delta t$$

The concentration of CH_3Cl was measured during the mission with the whole air sampler, and we used the concentration of OH and ascent rates described above.

As CO_2 has no significant chemical sources or sinks in the TTL, its slow ascent profile was based solely on tropospheric concentrations, which change seasonally and increase over time, transported upward through the TTL at the seasonal ascent rates described above. CO_2 concentrations at the base of the TTL were determined by averaging measurements in the months before each mission from Mauna Loa, Hawaii, [*Keeling et al*., 2009] and American Samoa [*Keeling et al*., 2008] delayed by 2 months. The O_3 slow ascent profile was based on radiative model calculations [*Folkins et al*., 2006; *Konopka et al*., 2009] that use observed tropospheric O_3 concentrations and O_2 photolysis rates to calculate its photochemical production during ascent through the TTL. The slower ascent rates during the summer allow for more ozone production in the TTL during TC4 than during CR-AVE.

4.3.2 Model Fitting Algorithm

As we have described above, transport into the TTL via slow ascent from the troposphere, transport from the midlatitude stratosphere, convection, and descent, each brings

with it a characteristic trace gas composition. From the tracer profiles associated with each pathway described in the previous section and shown in Figure 4.2, we expect that high convective input leads to high CO, low O_3, and low HCl, and high stratospheric input leads to low CO, high O_3, and high HCl, etc. The contribution of each pathway to the sampled air mass leads to the distinct combinations of tracer mixing ratios that were measured during the TC4 and CR-AVE campaigns. We assume that an air mass sampled between 355 and 430 K during the campaign is a mixture of air masses that followed one of the four described transport pathways. We can therefore describe any measured tracer mixing ratio as a sum of contributions from the four regions:

$$tr_{meas} = tr_{SlowAscent} \bullet fr_{SlowAscent} + tr_{strat} \bullet fr_{strat} + tr_{conv} \bullet fr_{conv} + tr_{descent} \bullet fr_{descent}$$

where tr_{meas} is the measured value of the tracer at a given potential temperature, $tr_{pathway}$ is the concentration of the tracer associated with the particular transport pathway and potential temperature (from the profiles shown in Figure 4.2), and $fr_{pathway}$ is the fraction of air from the transport pathway. An equation of this formula is generated for each of the 5 tracers measured during TC4 and for each of the 6 tracers measured during CR-AVE. At each point in time for which these tracers are observed in the TTL, the model uses a constrained least squares fitting algorithm to find the $fr_{SlowAscent}$, fr_{strat}, fr_{conv}, *and* $fr_{descent}$ that best fit the set of 5 or 6 equations above and the constraint equation:

$$fr_{SlowAscent} + fr_{strat} + fr_{conv} + fr_{descent} = 1$$

In this way, the model solves for the fractional contribution from each transport pathway that best fits all measured tracer concentrations at each point in time.

Recall that we include descent in the model as a consequence of convection; it is therefore not an independent variable, and is constrained by the convective mixing fraction such

that $fr_{descent} \leq \frac{1}{2} * fr_{conv}$. Convective outflow can mix with air at a higher level of the TTL before descending to its level of neutral buoyancy [*Sherwood and Dessler*, 2001], but we expect the resulting air parcel to be of greater convective character than descending character. Indeed, the parcel must consist primarily of cold convective outflow because it is the temperature imbalance which leads to descent of the parcel. Therefore, the fractional contribution of descent is limited to no more than half of the contribution of convection.

The fitting algorithm of the model is also weighted to account for the certainty with which each tracer source profile is known as well as the certainty in the measured tracer concentration. Based on both of these types of uncertainty, the tracers in the model are weighted such that $O_3 > CO = CO_2 > HCl > H_2O = \delta D$. In this way, anomalies in O_3, CO, and CO_2, whose source profiles are best understood, are given more weight than anomalies in H_2O and δD, whose variations are not captured as well by the model profiles. H_2O is weighted less than other tracers because local temperature variations can produce anomalies independent of an air mass' source, which is not accounted for in the model. However, because convection leaves a strong signature in water vapor above the tropopause in the summer, H_2O was weighted strongly above 380 K during TC4. δD is given a low weight because the model is unable to distinguish between convection in which ice particles are lofted and evaporate from convection in which they are not. In addition, there is greater uncertainty in the measurement accuracy of HDO than of the other tracers. However, strong positive anomalies in δD are still important indicators of convection; with our weighted method, this information can be used without smaller anomalies in δD dominating the model. HCl is also not weighted strongly because of the high instrument uncertainty associated with this measurement. The model and measurement uncertainty and

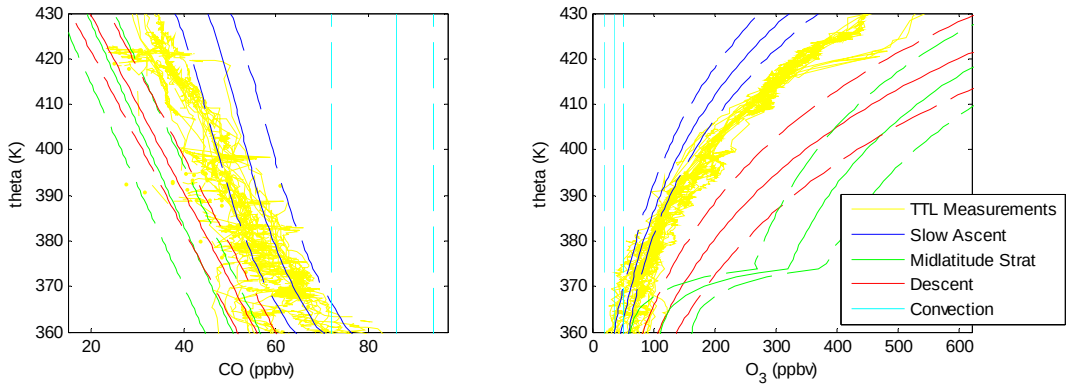

Figure 4.3: Solid lines: tracer profile attributed to each source region for CO and O_3 during CR-AVE; dashed lines: 1-σ uncertainty in each tracer profile.

relative tracer weights are shown in Table 4.3. The tracer weights must be chosen carefully such that natural scatter in the heavily weighted tracers due to variability of tropospheric or stratospheric sources does not significantly alter the model. When tracers are weighted properly, scatter in one tracer that is uncorrelated with changes in other tracers will not appreciably alter the model output.

4.3.3 Error Analysis

Before examining the model results, we first evaluate its sensitivity to the source region profiles determined above. Monte Carlo simulations were performed in which the model inputs – all source region profiles and the relative weights of the tracers – were varied randomly within best estimates of their possible uncertainty for 10,000 trials. Examples of the uncertainty in the CR-AVE CO and O_3 profiles are shown in Figure 4.3. Uncertainties were represented by either a normal or uniform distribution depending on the knowledge of the system. The uncertainty in the stratospheric and convective profiles was based on the spread in observed midlatitude and tropospheric concentrations, respectively. A uniform distribution was used for these profiles due to limited sampling in the troposphere and midlatitude stratosphere during the mission. The

uncertainty in the descending air tracer concentration was based on allowing descent of anywhere from 12-28 K in a uniform distribution, which represents the expected downward mixing produced by convection. The CO slow ascent profile uncertainty was based on running the kinetic model for CO chemical loss with the concentration of OH and the TTL ascent rates, the terms in the model with the largest uncertainty, varied within the likely values found in the literature. The uncertainty in the O_3 slow ascent profile was based on the range of values calculated by various radiative models in the literature [*Folkins et al*., 2006; *Konopka et al*., 2009; *Marcey et al.,* 2007]. Uncertainties in both slow ascent profiles were represented with a normal distribution. The uncertainties in the source region profiles of the other tracers were likewise calculated. The tracer weights were also varied from their original values, from weighting the tracers approximately evenly to strongly skewing the weights in favor of the most trusted tracers.

The model was run 10,000 times with each model input chosen randomly from within its range of uncertainty. As it was not reasonable to run the Monte Carlo simulation for every data point available, it was run for 5-8 air masses at various potential temperatures on each day, with ~4 data points with tracers indicating a common air mass averaged together. Examples of the Monte Carlo output for 365 K on 2/6/06 and for 405 K on 8/5/07 are shown in Figure 4.4. We show the distribution of possible mixing fractions from each source region; for 365 K on 2/6/06, the air mass fraction transported via slow ascent is most likely 18%, with 8-25% falling within the 1-sigma uncertainty. The convective fraction is shown to be 9±9%, and the midlatitude stratospheric fraction is 64±12%. This analysis was used to determine the 1-sigma variance in the air mass fraction attributed to each source region, which is shown as error bars in the results below.

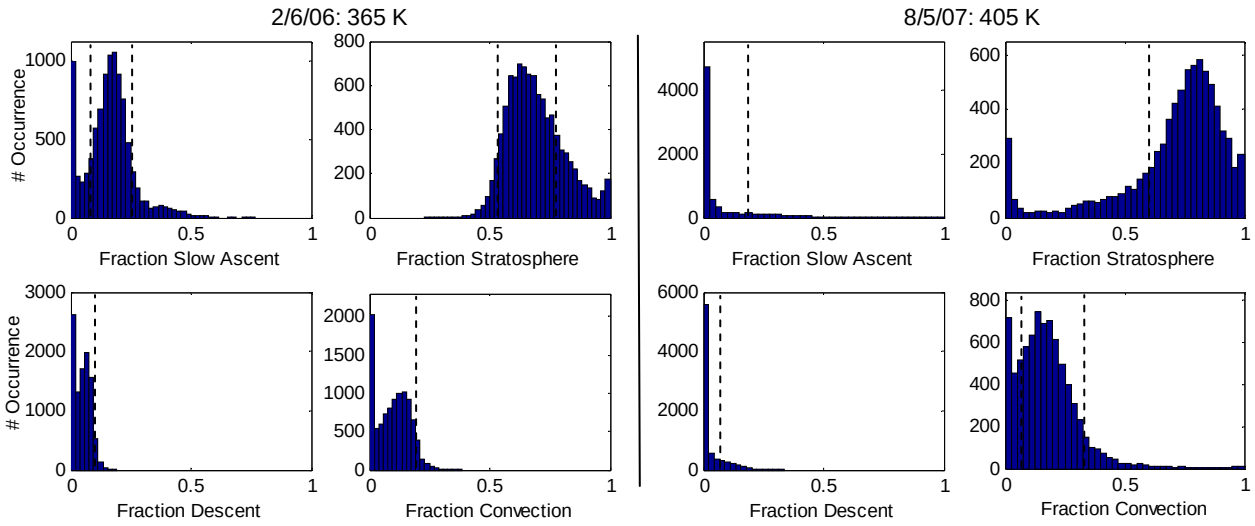

Figure 4.4: Sample Monte Carlo runs showing the distribution of possible results from the mixing model when all inputs are varied randomly within their calculated uncertainty; 1-σ uncertainty falls within the dashed lines. The air fraction from each source region is shown for 365 K on 2/8/06 (left) and for 405 K on 8/5/07 (right).

In addition to the Monte Carlo analysis, sensitivity studies were performed to test specific model assumptions directly. The model was run without each source region – without a midlatitude stratospheric input, without descent, and without convection or descent – and the results compared to the original model. The sensitivity of the stratospheric fraction of air to the inclusion of each source region for 2/6/06 is shown in the left panel of Figure 4.5, and the sensitivity of the convective fraction to each source region for 8/5/07 is shown in the right panel. For both cases, the model output typically changed by less than 10% with the removal of other potential source regions.

The sensitivity of the model to each tracer was also examined to verify that no single tracer disproportionately influenced the output. The fractional convective input calculated excluding each tracer is shown for 2/6/06 and 8/5/07 in Figure 4.6. Notice that the tracers weighted more heavily in the model have a greater impact on the results. Figure 4.5 and Figure 4.6 also include error bars calculated from the Monte Carlo analysis for comparison. The spread

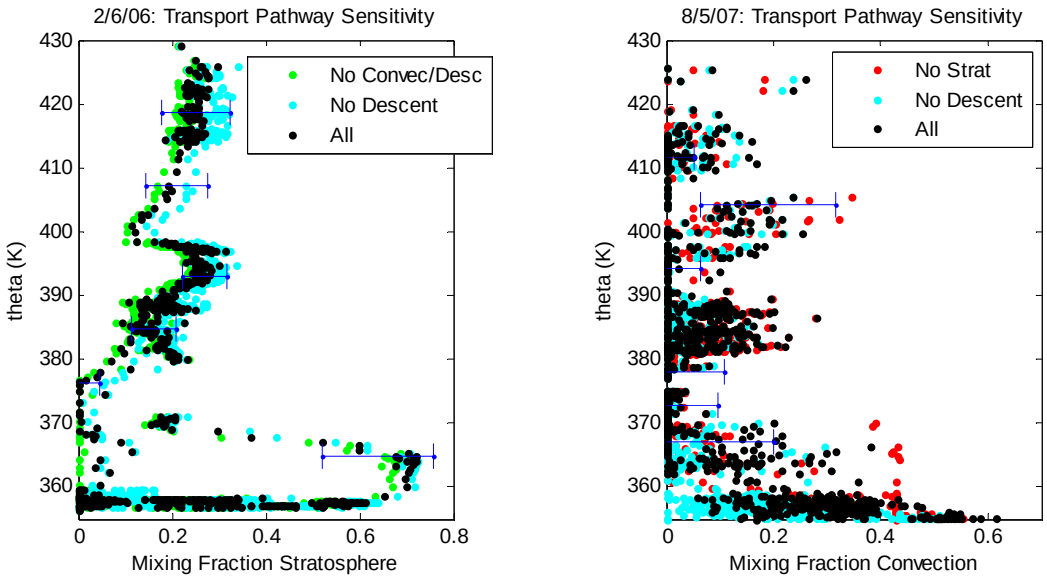

Figure 4.5: Model sensitivity to the inclusion of each transport pathway. Left: the fraction of air from the midlatitude stratosphere for model runs which exclude both convection and descent (green), exclude descent only (cyan), and include all pathways (black). Right: the fraction of air from convection for model runs which exclude midlatitude stratospheric input (red) and descent within the TTL (cyan) as compared to the baseline run including all transport pathways (black). Error bars based on Monte Carlo analysis are also shown in blue for comparison.

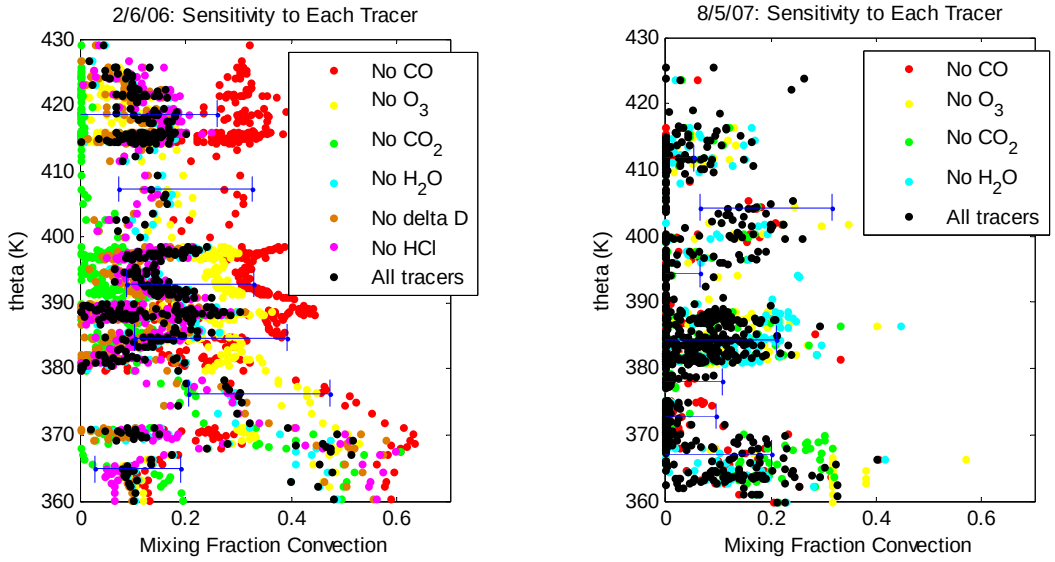

Figure 4.6: Model sensitivity to the inclusion of each tracer. The fraction of air from convection is shown for model runs which exclude each tracer one at a time. Left: flight on 2/6/06 from the CR-AVE campaign. Right: flight on 8/6/07 from the TC4 campaign. Error bars based on Monte Carlo analysis are also shown in blue for comparison.

in results from the sensitivity studies are typically on the order of the Monte Carlo error bars. A notable exception is the left panel of Figure 4.6, in which the convective mixing fraction calculated above 380 K excluding CO or CO_2 varies by significantly more than the Monte Carlo error bars. This is a result of the difference between the CO and CO_2 slow ascent profiles and the tracer measurements. The CO_2 observations fall close to the slow ascent profile and farther from the stratospheric profile, while the CO observations fall closer to the stratospheric profile (see Figure 4.2), which makes it impossible for the model to match both species with the same mixing fractions of air from each source region. Excluding one of these tracers therefore allows the model to fit the other tracer with significantly different mixing fractions. Alternative profiles that could match both tracers simultaneously are within the uncertainty in our calculated profiles; however, we use the profiles as shown because although they cannot both be correct, they represent the best information available. We expect that the Monte Carlo analysis provides a good estimate of this uncertainty because it allows both the CO and CO_2 profiles to vary within their calculated uncertainty, but always includes both tracers to incorporate all available information.

4.4 Results and Discussion

The mixing model was applied to the CR-AVE flights of 1/30/06, 2/1/06, 2/2/06, 2/6/06, 2/7/06, and 2/9/06, as well as to the TC4 flights of 8/5/07, 8/6/07, and 8/8/07. Sample model fits for 2/6/06 and 8/5/07 are shown in Figure 4.7 and Figure 4.8, respectively. Observed tracer concentrations are shown in blue and the model fit concentrations are shown in green, with the tracer profile associated with each transport pathway plotted as well for comparison. The fraction of air from each transport pathway designated by the model is shown in the last panel.

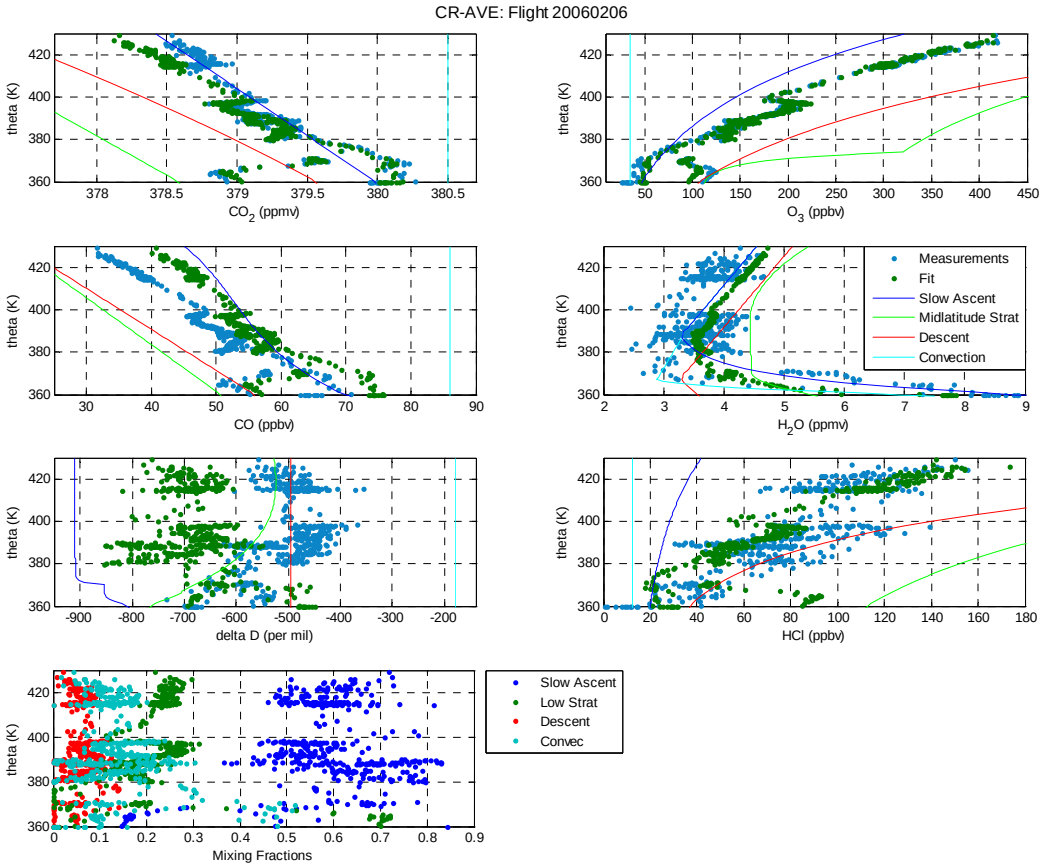

Figure 4.7: Measured and modeled tracer profiles for the flight on Feb. 6, 2006. Also plotted are the source profiles shown in Figure 4.2. Bottom: Mixing fraction from each source region.

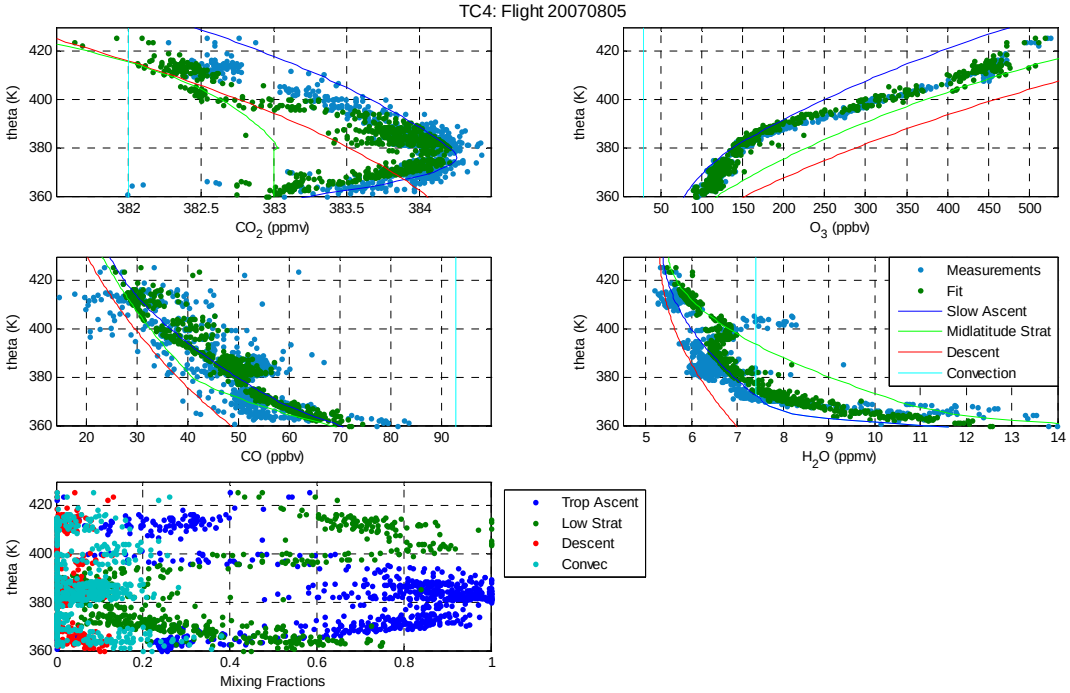

Figure 4.8: As in Figure 4.7, but for Aug. 5, 2007.

Note that when the observed tracer profiles fall closer to the stratospheric profiles, as from 360-365 K or 390-400 K on 2/6/06, the model indicates high fractions of stratospheric air. When the tracer observations fall closer to the convective profiles, as from 380-390K on 8/5/07 or 365-370K on 2/6/06, the model indicates high fractions of convective input.

Let us look in greater detail at several interesting flight segments. On 2/6/06, two distinct air masses were sampled from 360-370 K, one early in the flight with an extremely strong stratospheric signature, and one later in the flight with a distinct convective signature (Figure 4.7). The first air mass contained extremely low CO_2, high O_3, low CO, and slightly high H_2O; the model showed this air mass to be 70% (+6/-18%) stratospheric air, 9% (+10/-6%) convective, 5% (±4%) descent, and 16% (±9%) slow ascent. The second air mass contained elevated CO_2, low O_3, high CO, and slightly low H_2O, and the model indicated that it contained 46% (+18/-11%) convective air, 1% (±8%) descent, 5% (+4/-5%) stratospheric, and 48% (+12/-23%) slow ascent. Two similar distinct air masses were also observed on 2/7/06 from 360-375 K. This is a particularly striking example of how these tracers vary simultaneously to provide evidence for the origin of each air parcel.

8/5/07 presents an interesting convective influence profile. Figure 4.8 shows that convection was high (20%) in the TTL below 365 K, then fell to near zero from 370-380K, as indicated by significantly lower CO. Above the tropopause, two distinct air masses were observed, one with convective input but little stratospheric input from 380-390 K, and the other with both convective and stratospheric input from 395-405 K. From 380-390 K, elevated CO and low O_3 indicated significant convective input (10±10%) and very low stratospheric input (0±7%). From 395-405 K, elevated CO and very high H_2O pointed to high convective input of 19% (±12%), and a large increase in O_3 and decrease in CO_2 indicated a dramatic increase in

stratospheric input to 83% (±20%). The extremely high water vapor concentrations in this air mass were likely due to the lofting and evaporation of ice particles. The model does not fit the high H_2O values observed because it does not include evaporation of ice, but we discuss the impact of ice lofting in greater detail below.

Though the model fits most variations in tracer concentration well, particularly for those tracers weighted heavily in the model, several inconsistencies are worth discussing. During the CR-AVE flights, the model typically produces CO_2 concentrations slightly lower than observations, and CO concentrations slightly higher than observations (Figure 4.7). This is observed because the CO_2 observations fall very close to the slow ascent profile, while the CO observations fall closer to the stratospheric profile. As discussed in Section 4.3.3, this difference prevents both tracers from being fit simultaneously, but lies within our calculated uncertainty in the system. The model also rarely fits δD well. As described above, δD is given a low weight because of the inability of the model to distinguish convection which does or does not transport and evaporate ice particles. However, it is still a useful tracer because large positive anomalies are a good indicator of convection. Notice that although the average profile of δD is not fit well, several positive anomalies are reproduced with the model, such as the high δD excursions from 390-400 K and 410-420 K on 2/6/06.

The mixing fractions of convective input for each flight are shown in the top panels of Figure 4.9. The top right panel compares the convective air fractions for the two missions including error bars from the Monte Carlo analysis described above. These plots show, as expected, that a significant fraction of the air is of convective origin in the lower TTL, often 30-50% of the air mass, and that fraction falls off with increasing altitude. Notice that the model produces slightly more convection below the tropopause for the winter-time CR-AVE mission,

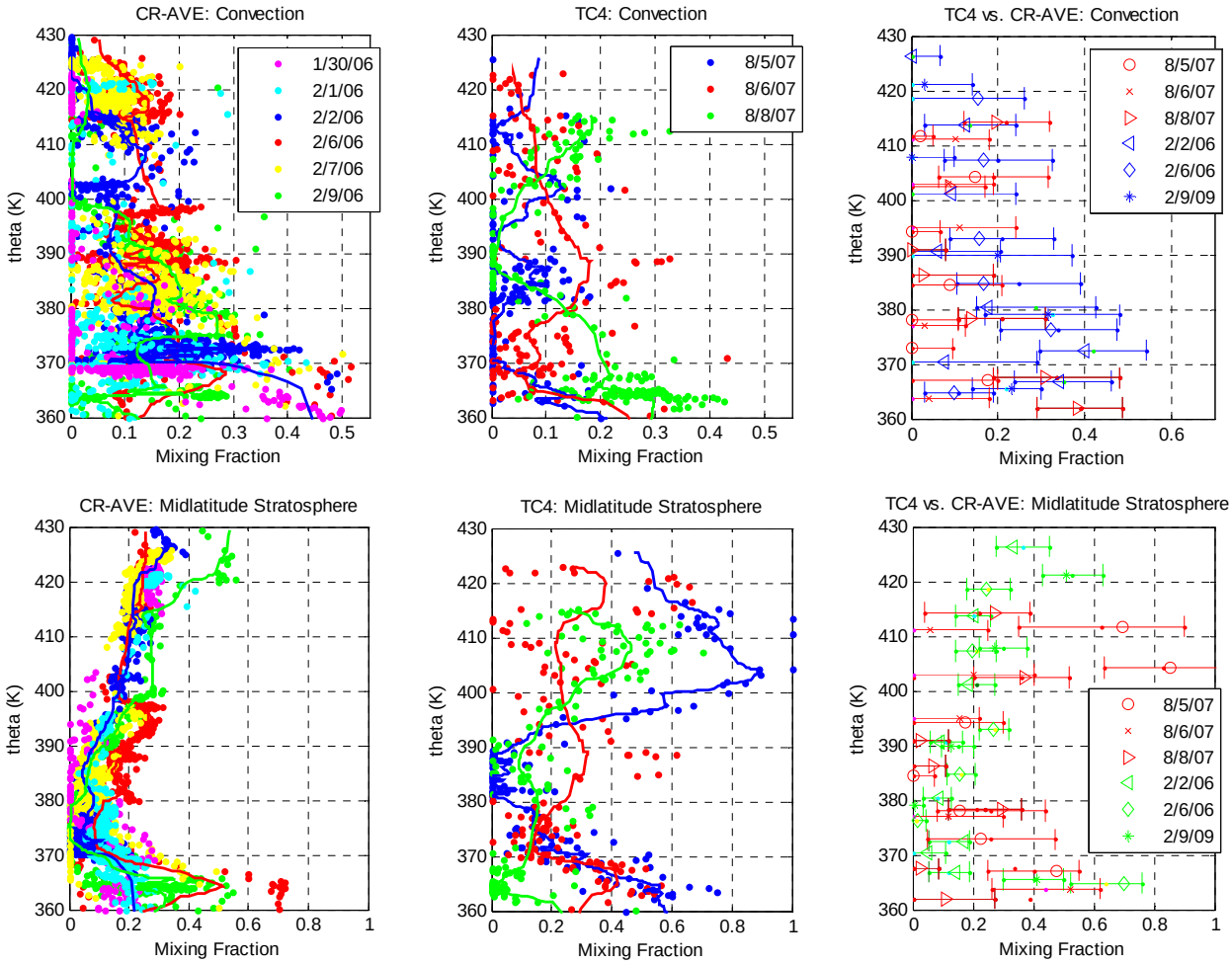

Figure 4.9: Mixing fraction from convection (top) and the midlatitude stratosphere (bottom), for each flight during the CR-AVE (left) and TC4 (middle) missions. Running averages are shown as thick lines. A comparison of TC4 vs. CR-AVE is shown on the right with error bars calculated using the Monte Carlo analysis described in the text.

with up to 40% convective air from 370-375 K, than for the summer-time TC4 mission, with up to 20% from 370-375 K. However, above the tropopause both CR-AVE and TC4 show on average ~10% convective influence, with up to 20% in some air masses up to 420 K. These results agree fairly well with *Park et al.* [2007, 2010], who performed a back-trajectory analysis for the CR-AVE and TC4 missions along the WB-57 flight track. From 370-375 K, they calculated 10% convective influence in the winter and 35% in the summer, which is comparable to our results, but with opposite seasonality. However, above the tropopause, where convective

influence is most important, Park et al. calculated 20% convective influence up to 390 K and 15% up to 410 K in the winter, and 15% convective influence up to 405 K in the summer, which is in excellent agreement with our results. Our analysis also produces a convective plume (15-20% convective influence) at 405-415 K on 8/8/07 which corresponds with a very deep convective event described by *Park et al.* [2010] using the back trajectory analysis. The seasonality of our results is also consistent with CALIPSO satellite data. Though CALIPSO observations over Costa Rica show greater cloud frequency (15-20%) at 90 hPa in the winter than in the summer (0-10%) [*Massie et al*., 2010], converting to potential temperature shows that these results are in fact compatible with ours. 90 hPa corresponds to ~377 K in the winter, where the mixing model calculates 10-25% convective influence, and ~388 K in the summer, where the model calculates 5-15% convection.

The fraction of air from the midlatitude stratosphere for each flight day is shown on the bottom panels of Figure 4.9. We calculate midlatitude stratospheric mixing fractions in the lower TTL of 30% on average, and up to 60% in some air masses, which then falls off somewhat from 380-390 K, before increasing again with altitude. Stratospheric mixing fractions of 20-40% were common in both seasons above the tropopause. Our results are fairly consistent with calculations by *Homan et al.* [2010], who used N_2O measurements over Africa to calculate that 30% of air at 390 K and 10-20% of air from 370-380 K is of stratospheric origin. They also agree fairly well with the magnitude of stratospheric input calculated by *Ploeger et al*. [2010], whose back trajectory model found 25-50% stratospheric input in the TTL on average. However, we differ with *Ploeger et al*. in the location of that mixing, as they found that the potential temperature at which trajectories crossed $\pm 35^{o}$ latitude peaks near 380 K, while we found a minimum in mixing at 380 K. This difference may be partly related do longitudinal

differences, as *Ploeger et al*. considered global average transport, and emphasized the importance of transport related to the Asian monsoon anticyclone, which is less relevant to our measurements near Costa Rica.

Comparing the midlatitude stratospheric input by season is complicated by the large error bars associated with the TC4 stratospheric values. Referring back to the tracer profiles from each source region (Figure 4.2), it is clear that there is a much smaller difference between the slow ascent and stratospheric tracer profiles for O_3, CO, and CO_2 in the summer (TC4) than in the winter (CR-AVE). In addition, HCl, a useful tracer of stratospheric input, was measured during CR-AVE but not during TC4. These factors reduce the model's skill in differentiating slow ascending tropical air from midlatitude stratospheric air during TC4, leading to the large error bars shown in Figure 4.9. Therefore, within the uncertainty of the model, there is no seasonal difference between the two missions, with the exception of 8/5/07 above 395 K, which had very high stratospheric input. The back trajectory model described by *Sayres et al.* [2010] also indicates significantly greater stratospheric input on 8/5/07 than during the other TC4 mission days. This study provides little evidence to resolve the difference between studies which found more transport from the stratosphere during the summer [*Ploeger et al.,* 2010; *Konopka et al.,* 2010], and those which found more transport during the winter [*Sayres et al.,* 2010].

It is also useful to view the model results from the point of view of the impact of each transport pathway on tracer concentrations. As we have seen above, a transport pathway can much more significantly alter the concentration of some tracers than that of others. The left panel of Figure 4.10 shows the fraction of the total concentration of each tracer that was transported into the TTL from the midlatitude stratosphere on 2/6/06, while the right panel shows the same for convective input on 8/5/07. Notice that while convection brings hardly any O_3 into

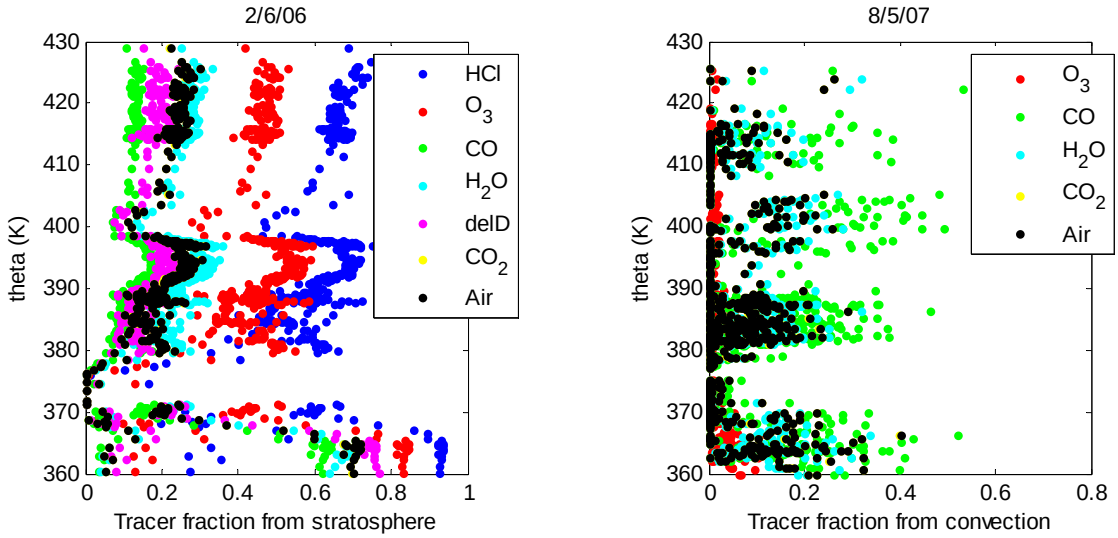

Figure 4.10: The fraction of the total concentration of each tracer that was transported into the TTL from the midlatitude stratosphere on 2/6/06 (left) and via convection on 8/5/07 (right).

the TTL, it is responsible for up to 40% of the CO above 380 K on 8/5/07, although only 20% of the air mass as a whole is of convective origin. Transport from the midlatitude stratosphere also affects tracer concentrations disproportionately, particularly HCl and O_3, which can be dramatically enhanced by stratospheric input. On 2/2/06, 20% of the air at 410 K is stratospheric, but 40% of observed O_3 originated in the stratosphere, as did 65% of the HCl. This result is consistent with the analysis of Marcy et al. [2007], who determined that 60-90% of HCl at the top of the TTL is stratospheric in origin.

To focus in particular on how transport affects O_3 concentrations in the TTL, we plot in Figure 4.11 the O_3 calculated by the model with and without input from the midlatitude stratosphere. In the left two panels, the standard model output is shown in green and the model output where the stratospheric air fraction has been replaced by slowly ascending tropical air is shown in blue. The inclusion of stratospheric air increases O_3 concentrations by 28% on average, and up to 48% in some air masses during CR-AVE (winter), and by 16% on average and up to 33% during TC4 (summer). Increases in O_3 of this magnitude were found both above and below the tropopause, with smaller increases (~18% in CR-AVE, ~10% in TC4) around the

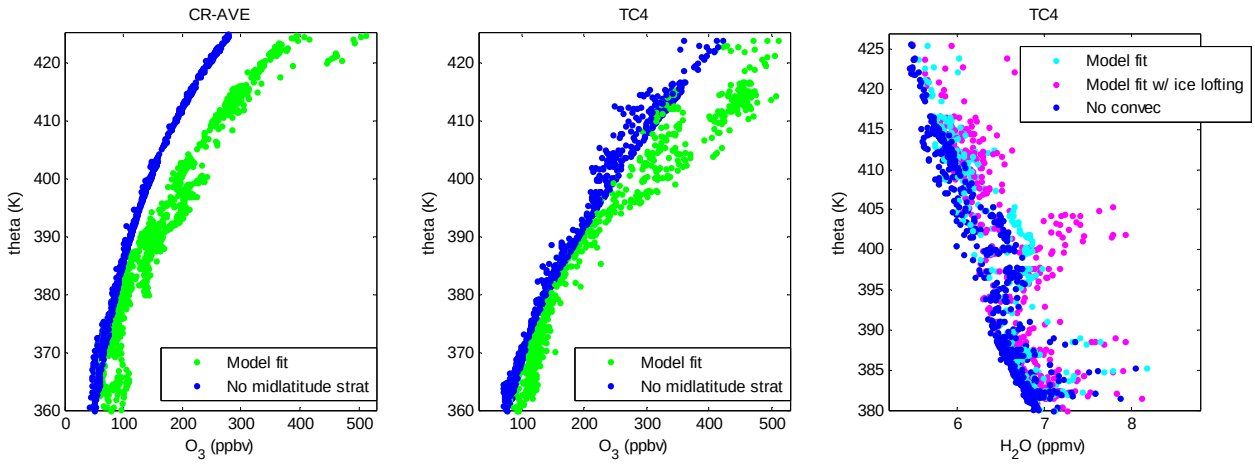

Figure 4.11: Left: O_3 calculated by the baseline model (green) and with the midlatitude stratospheric air fraction replaced by slow ascending tropical air (blue) for the entire CR-AVE mission. Middle: Same as left but for TC4. Right: H_2O calculated by the baseline model (cyan), the model with lofting of ice particles included in the convective water vapor term (pink), and with the convective air fraction replaced by slow ascending tropical air (blue) for the TC4 mission.

tropopause at 380 K. Transport from the midlatitude stratosphere therefore plays an important role in setting ozone concentrations and the thermal structure of the TTL.

A similar analysis was applied to examine the impact of convection on water vapor concentrations above the tropopause during the summertime TC4 mission. The CR-AVE mission was not included because the cold winter tropopause and increasing water vapor profile above the cold point make resolving convective injection very difficult. Recall that for TC4, we set the water vapor input from convection at all levels above 380 K to be 7.4 ppmv, the saturation mixing ratio at the cold point, balancing the competing effects of cold overshooting convection which could inject drier air parcels, and ice lofting which could produce wetter parcels. Because convection above the tropopause will affect tracers other than H_2O and δD equally with or without ice lofting, we did not distinguish such convection in the model. However, several air parcels with high water vapor concentrations above the tropopause clearly showed evidence of the evaporation of ice. A high water plume on 8/5/07 is shown in

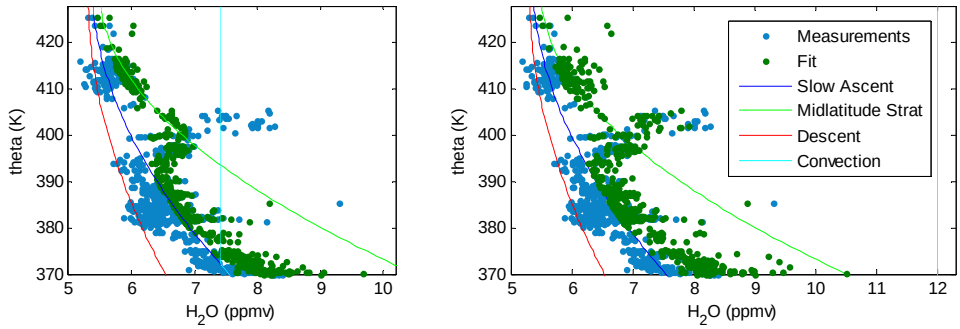

Figure 4.12: High water vapor plume observed on 8/5/07. Measured H_2O concentrations are shown in blue and modeled concentrations in green. Left: Baseline model without convective lofting of ice particles; convection injects air with 7.4 ppmv H_2O. Right: Model including lofting of ice particles; convection injects air with 12 ppmv H_2O.

Figure 4.12, with observations shown in blue and the model fit in green. In the original scenario, shown in the left panel, the model is unable to fit the high water vapor concentrations with convective injection of 7.4 ppmv H_2O. To simulate lofting of ice particles, we ran the model again with convection injecting 12 ppmv H_2O, which is the saturation mixing ratio at the altitude of the high water plume; the results are shown in the right panel. In this case the model produces a much better fit to the high water plume. While this analysis is useful for understanding the impact of ice lofting, we cannot universally assume that convection hydrates the stratosphere to the local saturation mixing ratio because other convective events, such as from 380-390 K on 8/5/07, show strong evidence of convection in CO but little change in water vapor.

We compare the impact of these two convective scenarios in the right panel of Figure 4.12. The standard model output is shown in cyan, the result with convective ice lofting is shown in pink, and the model output where the convective air fraction has been replaced by slow ascending tropical air is shown in blue. Even with the original model, water vapor above the tropopause increased by 0.1-0.4 ppmv when convection was allowed. Convective ice lofting increased water vapor by 0.5 ppmv on average and up to 1.6 ppmv in some air masses. Convection thus has a significant impact on water vapor above the tropopause in the summer,

increasing concentrations by ~5% without the evaporation of ice, and by up to 25% when evaporation occurs.

4.5 Conclusions

The Tropical Tropopause Layer is composed of a mixture of air that has been transported into the region from different sources and via different dynamical mechanisms. In this study, we considered transport into the TTL via slow ascent of tropical air, isentropic transport from the midlatitude lowermost stratosphere, deep tropical convection, and descent within the TTL coupled to convection. Quantifying the impact of these pathways is key to understanding the control of stratospheric water vapor and its response to a changing global climate. We analyzed in situ measurements of O_3, CO_2, CO, HCl, H_2O, and HDO from NASA's WB-57 aircraft during the CR-AVE campaign in the winter of 2006 and the TC4 campaign in the summer of 2007 to quantify the contributions of each of these pathways to transport in the TTL. Each pathway brings with it air with a characteristic trace gas composition, such that anomalies in simultaneously measured tracer concentrations can be used to determine the origins of the air mass. We used a simple 1-D box model with a constrained least squares fitting algorithm to find the fractional contribution of air from each source region that best fits the tracer concentrations measured in the TTL.

The mixing model was able to fit simultaneous local variations in tracer concentrations while attributing the contribution from each source region to the measured air mass. The input from convection and the midlatitude stratosphere determined by the model provide several key insights into the composition of the TTL over Costa Rica: (1) Convection below and above the tropopause was important in both summer and winter, with up to 50% of the air mass below 370

K influenced by convection, and on average 10%, and up to 20% convective influence in air masses up to 420 K. (2) Isentropic transport from the midlatitude lowermost stratosphere accounted for 20-60% of the air in the lower TTL, 10-20% of air near the tropopause, and 20-40% of air above 390 K. Within the uncertainty of the model, there was no seasonal difference in the contribution of this transport pathway. (3) Transport from the midlatitude stratosphere increased O_3 concentrations by 28% in the winter and by 16% in the summer both below and above the tropopause, with smaller increases around the tropopause itself. (4) In the summer, convection above the tropopause increased local water vapor concentrations on average by ~0.3 ppmv, but in air masses with evaporation of convectively lofted ice particles, by up to 1.6 ppmv.

The large impact of isentropic transport from the midlatitude stratosphere on TTL ozone concentrations has important implications for the radiative balance of the TTL and subsequently the amount of water vapor entering the stratosphere. Transport from the midlatitude stratosphere has a greater impact on ozone concentrations than on other species because of the large contrast between the tracer's tropospheric and stratospheric values. Midlatitude ozone concentrations are predicted to increase by up to 30% by the end of the 21st century due to ozone recovery and downwelling from an enhanced Brewer-Dobson circulation [*Gettelman et al., 2010*]. These changes, in addition to possible changes in the amount of in-mixing from midlatitudes into the TTL, could increase tropical ozone levels, thereby warming the TTL and tropopause. Interestingly, in the mixing model the midlatitude stratospheric input is smallest at the tropopause, where changes in absorption of radiation have the greatest impact on the amount of water entering the stratosphere. However, transport from the stratosphere increases tropopause-level O_3 by 18% in the winter and 10% in the summer, which still has a significant impact on temperature at those levels, and changes in temperature below the tropopause due to in-mixing

will also impact the amount of dehydration occurring in the TTL. Because even small changes in TTL temperature have a large impact on dehydration, increases in TTL ozone could have a significant impact on stratospheric water vapor in the future.

Furthermore, we have seen that deep convection penetrating above the tropopause can hydrate air parcels by up to 1.6 ppmv. The impact of convection on water vapor differs from its impact on other tracers, as convection detraining below the tropopause does not typically impact stratospheric water vapor concentrations, though it can influence the concentrations of other tracers, whereas convection above the cold point has the ability to disproportionately alter water vapor. Increasing sea surface temperatures in a warmer climate could lead to increases in such deep convection which could significantly increase stratospheric water vapor.

Long-lived tracer measurements have been used to quantify the importance of convection, in-mixing from the midlatitude stratosphere, slow ascent, and descent in the TTL. It is important to include all of these transport pathways in an analysis in order to understand not only the fractional contributions of each pathway to the TTL composition, but their varying impacts on tracer profiles, radiative budgets, and stratospheric humidity. The analysis presented here is limited to data obtained near Costa Rica and is not necessarily representative of the tropics as a whole. To further quantify the impact of these transport pathways on a global scale, a more detailed sampling of the tropics with simultaneous measurements of various tracers is required.

References

Daube, B., K. Boering, A. Andrews, and S. Wofsy (2002), A high-precision fast-response airborne CO2 analyzer for in situ sampling from the surface to the middle stratosphere, *J. Atmos. Oceanic Technol., 19*(10), 1532–1543.

de Reus, M., S. Borrmann, A. Bansemer, A. J. Heymsfield, R. Weigel, C. Schiller, V. Mitev, W. Frey, D. Kunkel1, A. Kürten, J. Curtius, N. M. Sitnikov, A. Ulanovsky, and F. Ravegnani (2009), Evidence for ice particles in the tropical stratosphere from in-situ measurements, *Atmos. Chem. Phys., 9*, 6775–6792.

Dessler, A.E. (2002), The effect of deep, tropical convection on the tropical tropopause layer, *J. Geophys. Res., 107*(D3), 10.1029/2001JD000511.

Dessler, A. E., and S. C. Sherwood (2003), A model of HDO in the tropical tropopause layer, *Atmos. Chem. Phys.*, *3*, 2173-2181.

Donner, L. J., L. W. Horowitz, A. M. Fiore, C. J. Seman, D. R. Blake, and N. J. Blake (2007), Transport of radon-222 and methyl iodide by deep convection in the GFDL Global Atmospheric Model AM2, *J. Geophys. Res., 112*, D17303, doi:10.1029/2006JD007548.

Durry, G., N. Huret, A. Hauchecorne, V. Marecal, J.-P. Pommereau, R. L. Jones, G. Held, N. Larsen, and J.-B. Renard (2006), Isentropic advection and convective lifting of water vapor in the UT – LS as observed over Brazil (22^{o}S) in February 2004 by in situ high-resolution measurements of H_2O, CH_4, O_3 and temperature, *Atmos. Chem. Phys. Discuss., 6*, 12469–12501.

Flocke, F., R. L. Herman, R. J. Salawitch, E. Atlas, C. R. Webster, S. M. Schauffler, R. A. Lueb, R. D. May, E. J. Moyer, K. H. Rosenlof, D. C. Scott, D. R. Blake, and T. P. Bui (1999), An examination of chemistry and transport processes in the tropical lower stratosphere using observations of long-lived and shortlived compounds obtained during STRAT and POLARIS, *J. Geophys. Res., 104*(D21), 26625–26642.

Folkins, I., M. Loewenstein, J. Podolske, S. Oltmans, M. Proffitt (1999), A barrier to vertical mixing at 14 km in the tropics: Evidence from ozonesondes and aircraft measurements, *J. Geophys. Res., 104* (D18), 22095-22102.

Folkins, I., P. Bernath, C. Boone, G. Lesins, N. Livesey, A. M. Thompson, K. Walker, and J. C. Witte (2006), Seasonal cycles of O_3, CO, and convective outflow at the tropical tropopause, *Geophysical Research Letters, 33*, L16802, doi:10.1029/2006GL026602.

Fueglistaler, S., A. Dessler, T. Dunkerton, I. Folkins, Q. Fu, and P. Mote (2009), Tropical tropopause layer, *Rev. Geophys., 47*, RG1004, doi:10.1029/2008RG000267.

Gettelman, A., M. I. Hegglin, S.-W. Son, J. Kim, M. Fujiwara, T. Birner, S. Kremser, M. Rex, J. A. Añel, H. Akiyoshi, J. Austin, S. Bekki, P. Braesike, C. Brühl, N. Butchart, M. Chipperfield,

M. Dameris, S. Dhomse, H. Garny, S. C. Hardiman, P. Jöckel, D. E. Kinnison, J. F. Lamarque, E. Mancini, M. Marchand, M. Michou, O. Morgenstern, S. Pawson, G. Pitari, D. Plummer, J. A. Pyle, E. Rozanov, J. Scinocca, T. G. Shepherd, K. Shibata, D. Smale, H. Teyssèdre, and W. Tian (2010), Multimodel assessment of the upper troposphere and lower stratosphere: Tropics and global trends, *J. Geophys. Res., 115*, D00M08, doi:10.1029/2009JD013638.

Gettelman, A., T. Birner, V. Eyring, H. Akiyoshi, S. Bekki, C. Brühl, M. Dameris, D. E. Kinnison, F. Lefevre, F. Lott, E. Mancini, G. Pitari, D. A. Plummer, E. Rozanov, K. Shibata, A. Stenke, H. Struthers, and W. Tian (2009), The Tropical Tropopause Layer 1960–2100, *Atmos. Chem. Phys., 9*, 1621–1637.

Homan, C. D., C. M. Volk, A. C. Kuhn, A. Werner, J. Baehr, S. Viciani, A. Ulanovski, and F. Ravegnani (2010), Tracer measurements in the tropical tropopause layer during the AMMA/ SCOUT-O3 aircraft campaign, *Atmos. Chem. Phys., 10*, 3615–3627.

Hong, G., P. Yang, B.-C. Gao, B. Baum, Y. Hu, M. King, and S. Platnick (2007), High Cloud Properties from Three Years of MODIS *Terra* and *Aqua* Collection-4: Data over the Tropics, *Journal of Applied Meteorology and Climatology, 46*, DOI: 10.1175/2007JAMC1583.1.

James, R. and B. Legras (2009), Mixing processes and exchanges in the tropical and the subtropical UT/LS, *Atmos. Chem. Phys., 9*, 25–38.

Keeling, R. F., S. C. Piper, A. F. Bollenbacher, and S. J. Walker (2008), Atmospheric CO2 values (ppmv) derived from in situ air samples collected at Mauna Loa, Hawaii, USA, Carbon Dioxide Research Group, Scripps Institution of Oceanography (SIO).

Keeling, R. F., S. C. Piper, A. F. Bollenbacher, and S. J. Walker (2009), Atmospheric CO2-curve values (ppmv) derived from flask air samples collected at American Samoa, Carbon Dioxide Research Group, Scripps Institution of Oceanography (SIO).

Khaykin, S., J.-P. Pommereau, L. Korshunov, V. Yushkov, J. Nielsen, N. Larsen, T. Christensen, A. Garnier, A. Lukyanov, and E.Williams (2009), Hydration of the lower stratosphere by ice crystal geysers over land convective systems, *Atmos. Chem. Phys., 9*, 2275–2287.

Konopka, P., J.-U. Grooß, G. Günther, F. Ploeger, R. Pommrich, R. Müller, and N. Livesey (2010), Annual cycle of ozone at and above the tropical tropopause: observations versus simulations with the Chemical Lagrangian Model of the Stratosphere (CLaMS), *Atmos. Chem. Phys., 10*, 121–132.

Konopka, P., J.-U. Grooß, F. Plöger, and R. Müller (2009), Annual cycle of horizontal in-mixing into the lower tropical stratosphere, *Journal of Geophysical Research, 114*, D19111, doi:10.1029/2009JD011955.

Konopka, P., G. Günther, R. Müller, F. H. S. dos Santos, C. Schiller, F. Ravegnani, A. Ulanovsky, H. Schlager, C. M. Volk, S. Viciani, L. L. Pan, D.-S. McKenna, and M. Riese

(2007), Contribution of mixing to upward transport across the tropical tropopause layer (TTL), *Atmos. Chem. Phys., 7*, 3285–3308.

Loewenstein, M., H. Jost, J. Grose, J. Eilers, D. Lynch, S. Jensen, and J. Marmie (2002), Argus: A new instrument for the measurement of the stratospheric dynamical tracers, N_2O and CH_4, *Spectrochim. Acta A, 58*(11), 2329 – 2345.

Marcy, T.P., R.S. Gao, M.J. Northway, P.J. Popp, H. Stark, D.W. Fahey (2005), Using chemical ionization mass spectrometry for detection of HNO_3, HCl, and $ClONO_2$ in the atmosphere, *International Journal of Mass Spectrometry, 243*, 63–70.

Marcy, T.P., P.J. Popp, R.S. Gao, D.W. Fahey, E.A. Ray, E.C. Richard, T.L. Thompson, E.L. Atlas, M. Loewenstein, S.C. Wofsy, S. Park, E.M. Weinstock, W.H. Swartz, M.J. Mahoney (2007), Measurements of trace gases in the tropical tropopause layer, *Atmospheric Environment 41,* 7253–7261.

Massie, S. T., J. Gille, C. Craig, R. Khosravi, J. Barnett, W. Read, and D. Winker (2010), HIRDLS and CALIPSO observations of tropical cirrus, *J. Geophys. Res., 115*, D00H11, doi:10.1029/2009JD012100.

Park, S., R. Jiménez, B. C. Daube, L. Pfister, T. J. Conway, E.W. Gottlieb, V. Y. Chow, D. J. Curran, D. M. Matross, A. Bright, E. L. Atlas, T. P. Bui, R.-S. Gao, C. H. Twohy, and S. C. Wofsy (2007), The CO_2 tracer clock for the Tropical Tropopause Layer, *Atmos. Chem. Phys., 7*, 3989–4000.

Park, S., E. L. Atlas, R. Jiménez, B. C. Daube, E.W. Gottlieb, J. Nan, D. B. A. Jones, L. Pfister, T. J. Conway, T. P. Bui, R.-S. Gao, and S. C. Wofsy (2010), Vertical transport rates and concentrations of OH and Cl radicals in the Tropical Tropopause Layer from observations of CO_2 and halocarbons: implications for distributions of long- and short-lived chemical species, *Atmos. Chem. Phys., 10*, 6669–6684.

Pearson, R.W. and D.H. Stedman (1980), Instrumentation for fast response ozone measurements from aircraft, *Atmos. Tech., 12*, 51-55.

Ploeger, F., P. Konopka, G. Günther, J.-U. Grooß, and R. Müller (2010), Impact of the vertical velocity scheme on modeling transport in the tropical tropopause layer, *J. Geophys. Res*., *115*, D03301, doi:10.1029/2009JD012023.

Proffitt, M. H. and R. J. McLaughlin (1983), Fast-response dual-beam UV-absorption ozone photometer suitable for use on stratospheric balloons, *Rev. Sci. Instrum*., 54, 1719 – 1728.

Sachse, G. W., G. F. Hill, L. O. Wade, and M. G. Perry (1987), Fast-response, high-precision carbon monoxide sensor using a tunable diode laser absorption technique, *J. Geophys. Res., 92*, 2071-2081.

Sander, S. P., R. R. Friedl, A. R. Ravishankara, D. M. Golden, C. E. Kolb, M. J. Kurylo, M. J. Molina, G. K. Moortgat, H. Keller-Rudek, B. J.Finlayson-Pitts, P. H. Wine, R. E. Huie, V. L. Orkin (2006), Chemical Kinetics and Photochemical Data for Use in Atmospheric Studies: Evaluation Number 15, *JPL Publication, 06-2.*

Sayres, D., E. J. Moyer, T. F. Hanisco, J. M. St. Clair, F. N. Keutsch, A. O'Brien, N. T. Allen, L. Lapson, J. N. Demusz, M. Rivero, T. Martin, M. Greenberg, C. Tuozzolo, G. S. Engel, J. H. Kroll, J. B. Paul, and J. G. Anderson (2009), A new cavity based absorption instrument for detection of water isotopologues in the upper troposphere and lower stratosphere, *Review of Scientific Instruments, 80*, 044102.

Sayres, D. S., L. Pfister, T. F. Hanisco, E. J. Moyer, J. B. Smith, J. M. St. Clair, A. S. O'Brien, M. F. Witinski, M. Legg, and J. G. Anderson (2010), Influence of convection on the water isotopic composition of the tropical tropopause layer and tropical stratosphere, *J. Geophys. Res., 115*, D00J20, doi:10.1029/2009JD013100.

Sherwood, S., and A. E. Dessler (2001), A model for transport across the tropical tropopause, *J. Atmos. Sci.*, *58*, 765–779.

Smith, J. B. (2011), *The Sources and Significance of Stratospheric Water Vapor: Mechanistic Studies from Equator to Pole*, Thesis, Harvard University, Department of Earth and Planetary Sciences.

Spivakovsk1y, C. M., J. A. Logan, S. A. Montzka, Y. J. Balkansk1i, M. Foreman-Fowler, D. B. A. Jones, L. W. Horowitz , A. C. Fusco, C. A. M. Brenninkmeijer, M. J. Prather, S. C. Wofsy, and M. B. McElroy (2000), Three-dimensional climatological distribution of tropospheric OH: Update and evaluation, *Journal of Geophysical Research, 105*(D7), 8931-8980.

St. Clair, J. M., T. F. Hanisco, E. M. Weinstock, E. J. Moyer, D. S. Sayres, F. N. Keutsch, J. H. Kroll, J. N. Demusz, N. T. Allen, J. B. Smith, J. R. Spackman, and J. G. Anderson (2008), A new photolysis laser-induced fluorescence instrument for the detection of H_2O and HDO in the lower stratosphere, *Review of Scientific Instruments, 79*, 064101.

Vay, S. A., et al. (2003), The influence of regional-scale anthropogenic emissions on CO2 distributions over the western North Pacific, *J. Geophys. Res., 108*(D20), 8801.

Webster, C. R., R. D. May, C. A. Trimble, R. G. Chave, and J. Kendall (1994), Aircraft laser infrared absorption spectrometer (ALIAS) for in situ atmospheric measurements of HCl, N2O, CH4, NO2, and HNO3, Appl. Opt., 33, 454–472.

Weinstock, E. M., E. J. Hintsa, A. E. Dessler, J. F. Oliver, N. L. Hazen, J. N. Desmusz, N. T. Allen, L. B. Lapson, and J. G. Anderson (1994), New fast response photofragment fluorescence hygrometer for use on the NASA ER-2 and the Perseus remotely piloted aircraft, Rev. Sci. Instrum., 65, 3544–3554.

Wennberg, P. O., T. F. Hanisco, L. Jaeglé, D. J. Jacob, E. J. Hintsa, E. J. Lanzendorf, J. G. Anderson, R.-S. Gao, E. R. Keim, S. G. Donnelly, L. A. Del Negro, D. W. Fahey, S. A. McKeen, R. J. Salawitch, C. R. Webster, R. D. May, R. L. Herman, M. H. Proffitt, J. J. Margitan, E. L. Atlas, S. M. Schauffler, F. Flocke, C. T. McElroy, and T. P. Bui (1998), Hydrogen radicals, nitrogen radicals, and the production of O3 in the upper troposphere, *Science, 279*, 49.

Chapter 5

Concluding Remarks

5.1 Mechanisms Which Control Stratospheric Humidity

We conclude by revisiting the various mechanisms which play a role in setting the water vapor concentration of the stratosphere, and examining how this work has contributed to our understanding of those mechanisms. We also explore the continuing gaps in our understanding, and propose future work aimed at resolving those outstanding questions. In Chapter 1.2.3, we examined in detail a number of mechanisms through which stratospheric water vapor may increase or decrease in the future due to a warming climate and changes in stratospheric ozone. Tropical tropopause temperatures, which to first order set the amount of water entering the stratosphere, may change in the future due to increasing tropospheric temperatures, changes in stratospheric ozone, changes in the Brewer-Dobson circulation (BDC), or increasing convective cooling of the tropical tropopause layer (TTL). Moistening of the stratosphere by convection above the tropopause both in the tropics and at midlatitudes, which bypasses the thermal control of the cold point, could also increase in a warmer climate. Here, we attempt to quantify the approximate order of magnitude of the impact that each of these pathways will have on future stratospheric water vapor as a way to synthesize the current understanding of predictions for stratospheric humidity.

Tropical Convective Hydration

Convective injection of ice above the tropical tropopause has the potential to moisten the stratosphere by transporting water in excess of the saturation mixing ratio of the local cold point. Such convection has been demonstrated to play an important role in the stratospheric water vapor budget, with several studies indicating that 10-15% of tropical air from 380-400 K is of convective origin [*Park et al*., 2007; *Park et al*., 2010; *Massie et al*., 2010]. In Chapter 4, we used in situ measurements of O_3, CO_2, CO, HCl, H_2O, and HDO in a simple 1-D mixing model to assess the impact of convection throughout the TTL. From in situ measurements obtained in the winter of 2006 and the summer of 2007 over Costa Rica, we found on average 10%, and up to 20% convective influence in air masses from 380-410 K. We also examined the impact of this convection on stratospheric water vapor concentrations, and found that in the summer, convection increased the amount of water vapor above the tropical tropopause by an average of 0.3-0.4 ppmv above the amount of water in slowly ascending air.

Though past studies disagree as to whether climate change and the associated increase in sea surface temperatures will lead to increasing deep convection in the tropics [*Solomon et al*., 2005; *Gettelman et al.,* 2002; *Johnson and Xie,* 2010], if such convection were to increase in the future, it could have a significant impact on stratospheric water vapor concentrations. As a 1st order estimate we may expect convective hydration to increase on the order of magnitude of its current impact on water vapor. Though the above study is specific to air above Costa Rica in the summer, we estimate that convective hydration may increase stratospheric water vapor by ~ 0.4 ppmv, doubling of the amount of water currently transported through this mechanism. Alternatively, we could estimate the impact of convective hydration by its implication in past water vapor trends. Increasing convection has been identified as a possible cause for the ~0.7

Table 5.1: Order of magnitude analysis of the potential impact of various mechanisms on future stratospheric water vapor concentrations.

Mechanism	*Anthropogenic Forcing*	*Implication in Past Trends*	*Future Water Vapor Impact*
Tropical Convective Hydration	Warming climate	1980-2000: +0.7 ppmv H_2O	+0.4 – +0.7 ppmv
Midlatitude Convective Hydration	Warming climate	1980-2000: +0.7 ppmv H_2O	+2 ppmv locally +0.4 ppmv tropics
Convective Dehydration	Warming climate	1980-2000: -1 K 2000-2004: -1 K, -0.4 ppmv H_2O	-0.4 ppmv
Ozone Radiative Heating	Ozone loss/recovery	1980-2000: -1 K	+0.3 ppmv
Tropospheric Temperatures	Warming climate	-	+0.6 ppmv
Brewer-Dobson Circulation	Warming climate Ozone loss/recovery	1980-2000: -1 K 2000-2004: -1 K, -0.4 ppmv H_2O	-0.2 – -0.4 ppmv

ppmv increase in water vapor observed in some datasets from 1980-2000 [*Dessler et al.*, 2007]. If that trend were to continue into the future, we would expect stratosphere water vapor to increase on the order of 0.7 ppmv over the next several decades. This analysis is summarized in Table 5.1.

Convective Dehydration

If tropical convection increases in the future, it could also have an opposing effect on stratospheric water vapor if cold convective outflow leads to colder temperatures at and below the tropopause and greater dehydration of the TTL. Increased convective dehydration has been proposed to explain both the ~0.5 K/decade cooling trend at the tropical tropopause from 1980-2000, and the more abrupt tropopause cooling of ~1 K from 2000-2004 [*Rosenlof and Reid*, 2008]. Though only the 2000-2004 cooling trend was associated with a decrease in stratospheric water vapor, if the connection between deep convection and stratospheric water vapor continues

into the future, we would expect an impact on the order of past trends, potentially reducing H_2O by ~0.4 ppmv over the next decades.

Midlatitude Convective Hydration

Deep midlatitude convection, which has been observed at potential temperatures up to 410 K [*Hanisco et al*., 2007], plays a significant role in the stratospheric water vapor budget. *Dessler and Sherwood* [2004] calculate that convection increases water vapor by ~40% at 380 K in the summertime northern midlatitudes, or by ~2 ppmv. Summertime continental convective activity at midlatitudes is predicted to increase in a warmer climate, with the potential to inject more moisture into the midlatitude stratosphere, particularly over the United States and Asia [*Trap et al*., 2009; *Van Klooster and Roebber*, 2009]. If convection were to increase on the order of magnitude of its current impact on water vapor, we would expect midlatitude water vapor at 380 K to increase by ~2 ppmv in convectively active regions. This enhanced water vapor would have important local radiative effects, and water injected above 380 K could potentially be transported equatorward and enter the mean circulation, increasing overworld stratospheric water vapor. In the mixing model described in Chapter 4, we found that ~40% of air above 390 K in the summer originated in the midlatitude stratosphere. If midlatitude water vapor concentrations increased by 2 ppmv, tropical water vapor concentrations at 390 K would be expected to increase by ~0.8 ppmv. However, as this deep convection is mainly observed over the United States and Asia in the summer, the global increase in upper TTL water vapor would likely be smaller, averaging the impacts of transport from convective and non-convective midlatitude regions; we estimate the net impact would be on the order of a ~0.4 ppmv increase in water vapor.

Ozone Radiative Heating

Ozone concentrations also impact tropical tropopause temperatures and therefore the amount of water vapor entering the stratosphere. Ozone in the TTL warms the tropopause directly through the absorption of shortwave radiation, while ozone above in the stratosphere warms the tropopause by emitting downwelling longwave radiation. Destruction of stratospheric ozone likely played a role in the observed 0.5 K/decade cooling trend observed from 1980-2000, and if ozone concentrations stabilize or increase due to the removal of stratospheric chlorine over the next decades, it would have a warming effect at the tropopause [*Austin et al*., 2008].

The majority of ozone in the TTL is produced in situ by the photodissociation of oxygen, which is not appreciably affected by stratospheric ozone trends. However, a significant portion is also transported into the TTL from the midlatitude stratosphere, where ozone depletion is important. Past studies have estimated that 25-50% of TTL air originated in the stratosphere [*Ploeger et al*., 2010; *Homan et al.,* 2010], and our mixing model (Chapter 4) found that such transport was the source of 20-60% of the air in the lower TTL, 10-20% of air near the tropopause, and 20-40% of air above 390 K in both summer and winter. In the mixing model, this transport increased TTL ozone concentrations by 28% in the winter and by 16% in the summer both below and above the tropopause, and by 18% in the winter and 10% in the summer around the tropopause itself. Ozone in the TTL and its radiative impact are thus sensitive to both the amount of inmixing from midlatitudes and the midlatitude concentration of ozone.

Satellite and ground-based observations indicate that midlatitude lower stratospheric ozone concentrations decreased by ~15% since 1980 [*Austin and Wilson*, 2006; *Forster et al.,* 2007]. If stratospheric ozone concentrations recover to 1980 levels over the next decades, and transport from midlatitudes into the TTL remains similar to current levels, we would expect an

increase in TTL ozone of ~10 ppbv, which would warm the tropopause by ~0.25 K [*Chae and Sherwood*, 2007]. Based on the resulting change in saturation mixing ratio at the tropopause, we would expect the amount of water vapor entering the stratosphere to increase by ~0.2 ppmv due to this change in TTL ozone alone. The tropopause would also be expected to warm due to increased downwelling longwave radiation from recovering ozone in the stratosphere. In a coupled chemistry-climate model, *Austin et al.* [2008] found that past ozone loss produced a total of 0.7 K cooling from 1970-2000, and ozone recovery would lead to similar warming in the future with a total associated increase in water vapor of 0.3 ppmv.

Increasing Tropospheric Temperatures

Future changes in the atmospheric temperature profile will also be important in setting tropical tropopause temperatures. Warming of the tropical troposphere tends to shift the atmospheric temperature profile towards a warmer, higher tropopause, while stratospheric cooling shifts the tropopause colder and higher. Though past warming of the troposphere has not correlated with any increase in tropopause temperatures, *Austin et al*. [2008] calculate that past surface warming would have warmed the tropopause by only 0.1 K, while future warming will increase temperatures by ~1.2 K by 2100. They predict that as surface warming accelerates over the next decades, it will overwhelm the impact of stratospheric cooling to warm the tropopause and increase stratospheric water vapor by ~0.6 ppmv.

Brewer-Dobson Circulation

The Brewer-Dobson circulation plays a key role in determining the strength of upwelling in the TTL and the associated cooling of the tropical tropopause. The strength of the planetary

waves which drive the BDC is thought to be related to the UT/LS temperature gradient, which increases with both surface warming and ozone depletion, and decreases with ozone recovery. Increase of the BDC has been proposed as a possible cause of past cooling of the tropical tropopause from 1980-2006 and the sharp drop in tropopause temperatures observed from 2000-2004. In particular, the cooling in 2000 is correlated with increased planetary wave activity along with a ~0.4 ppmv drop in water vapor [*Dhomse et al*., 2008]. Based on the combined effects of surface warming and recovering ozone, different models predict increases in the strength of the BDC ranging from continuing at the rate of past trends [*Butchart et al*., 2006] to 40% of past trends [*Li et al*., 2007]. If such changes occur in the future, we would expect water vapor to decrease by 40-100% of the amount of relevant past trends, or 0.15-0.4 ppmv over the next several decades.

Our order of magnitude analysis of the potential impact of these mechanisms on stratospheric humidity is summarized in Table 5.1. We do not speculate that future water vapor trends will equal the sum of the right-hand column, as there is substantial uncertainty in the future evolution of each mechanism, but present these estimates to demonstrate the potential importance of each factor. Changes in stratospheric water vapor on the order of 0.4 ppmv are suggested to alter the rate of surface warming by ~25% [*Solomon et al*., 2010]; therefore any of these changes have to potential to significantly impact the radiative budget of the planet. Note that based on the current understanding of these processes, all are predicted to have a comparable impact on stratospheric water vapor in the future. No one mechanism stands out as irrelevant to or dominating future changes in stratosphere humidity, underscoring the importance of better understanding each process if we are to predict the evolution of stratospheric water vapor.

5.2 Water Vapor Measurement Accuracy

Prior to 2011, water vapor measurements in the upper troposphere and lower stratosphere consistently showed disagreements of 1.5-2 ppmv, well outside the stated uncertainty of each instrument and the accuracy necessary to understand water vapor transport mechanisms and trends. In Chapter 3, we described a new instrument developed by our laboratory to address these accuracy concerns, the Harvard Herriott Hygrometer (HHH). HHH is the first direct absorption tunable diode laser (TDL) instrument to measure water vapor in the UT/LS, and it achieves high precision of 0.1 ppmv in 1 sec with accuracy of 5% ± 0.5 ppmv. The instrument successfully flew in the MACPEX campaign in April, 2011 on NASA's WB-57 aircraft; also measuring water vapor from the WB-57 were the Lyman-α, FISH, CIMS, ULH, and ALIAS instruments, and the CFH frostpoint hygrometer flew on a nearby research balloon. In a significant improvement over past campaigns, HHH, Lyman-α, FISH, CIMS, and CFH consistently agreed to within 6% at high water and to within 0.7 ppmv at low water, which is within the stated uncertainties of each instrument and significantly better than past agreement. Looking to the future, it will be important to continue water vapor comparisons and to return to the wintertime tropics to demonstrate agreement of these instruments over time and at the lowest water vapor concentrations in the atmosphere.

5.3 Outstanding Scientific Questions

The analysis in Section 5.1 demonstrates that significant uncertainty remains in predicting both the sign and the magnitude of the response of stratospheric water vapor to a warming climate and changing stratospheric ozone concentrations. However, the improved accuracy of the suite of in situ water vapor instruments provides an opportunity to better address

these questions through continuing research. Predicting future stratospheric water vapor levels can be addressed through two concurrent pathways: 1) continuing and more accurate measurements of tropopause temperature, UT/LS water vapor, midlatitude stratospheric water vapor, upwelling strength, age of stratospheric air, and convective intensity to observe trends over time; 2) improved understanding of the dominant processes which control stratospheric humidity at the present.

Water vapor trends are typically assessed from monthly measurements by the balloon-borne CFH instrument over Boulder, CO, [*Scherer et al*., 2008] and from satellite instruments whose retrieval algorithms are validated based on in situ measurements. The improved agreement between CFH and other in situ instruments provides increased confidence in CFH and satellite water vapor trends into the future. However, it is important that CFH continues to be compared in situ with other water vapor instruments to demonstrate that this agreement continues, and provide confidence in future observed trends. In the continued analysis of trends in these data, the differing outcomes expected due to climate change and recovering stratospheric ozone present a unique opportunity to disentangle the various mechanisms which control stratospheric humidity. While the trend of surface warming is predicted to accelerate in the future, the trend in stratospheric ozone concentrations should stabilize and potentially reverse as ozone depleting substances are removed from the atmosphere. Trends produced by climate change would therefore be expected to continue and accelerate in the future, while trends produced by ozone depletion may reverse. Observations of tropical tropopause temperature and stratospheric water vapor as ozone concentrations stabilize may therefore help to shed light on which of the factors outlined above dominate the control of stratospheric humidity.

Assessment of water vapor trends could also be improved by expanding the implementation of continuous monthly balloon-based frostpoint hygrometer measurements. As we have described above, the tropics and midlatitudes are subject to different mechanisms which may change water vapor concentrations in different ways. In particular, while changes in the water vapor entering the stratosphere in the tropics affect the global stratosphere, changes in midlatitude convection may impact midlatitude water vapor concentrations differently. It would therefore be extremely beneficial to establish a long term tropical in situ water vapor record to provide measurements with better spatial resolution than that of satellites for detection of trends. As both tropical tropopause temperatures and midlatitude convection vary regionally, a network of such measurements around the globe would also provide important information for establishing a global picture of stratospheric water vapor trends.

In the second approach to predicting future stratospheric humidity, measurements of water vapor and water isotopes in combination with other tracers, wind patterns, and temperature, can be used to assess the hydration and dehydration mechanisms currently operating in the TTL. Such measurements could help determine if dehydration to levels of stratospheric entry occurs primarily within or outside of cold convective outflow, and in specific geographic regions or all around the globe. We expect the improved agreement among the suite of water vapor instruments to improve our understanding of these processes, as they require accurate knowledge of saturation levels, which were not well constrained in the past. Improved water vapor measurements may also allow for better assessment of the impact of convective hydration above the tropopause. While satellite measurements can detect high water vapor plumes, in situ measurements offer the opportunity for spatially resolved, concurrent measurements of various relevant trace gases. Multiple profiles through convective plumes can

be used to map their properties and spatial extent and to fill in gaps between satellite profiles. Such detailed measurements could then be combined with satellite measurements to evaluate the spatial and temporal prevalence of such high water events.

The continued assessment of trends in water vapor data combined with focused flight campaigns aimed at testing relevant hypotheses are important steps in improving our understanding of the mechanisms which may produce future changes in stratospheric humidity. As a strong greenhouse gas in an atmospheric region where absorption lines are unsaturated, stratospheric water vapor can significantly affect the radiation balance of the planet and therefore surface temperatures. It is critical to reduce uncertainty in predictions of future stratospheric humidity to assess this climate feedback as we continue to improve our understanding of the climate system.

References

Austin, J., and T. J. Reichler (2008), Long-term evolution of the cold point tropical tropopause: Simulation results and attribution analysis, *J. Geophys. Res.-Atmos.*, *113*.

Austin, J., and R. J. Wilson (2006), Ensemble simulations of the decline and recovery of stratospheric ozone, *J. Geophys. Res., 111*, D16314.

Butchart N., A. A. Scaife, M. Bourqui, J. de Grandpré, S. H. E. Hare, J. Kettleborough, U. Langematz, E. Manzini, F. Sassi, K. Shibata, D. Shindell, M. Sigmond (2006), Simulations of anthropogenic change in the strength of the Brewer–Dobson circulation, *Clim. Dyn., 27*, 727–741.

Chae, J. H., and S. C. Sherwood (2007), Annual temperature cycle of the tropical tropopause: A simple model study, *J. Geophys. Res., 112*, D19111.

Dessler, A. E., and S. C. Sherwood (2004), Effect of convection on the summertime extratropical lower stratosphere, *J. Geophys. Res.*, *109,* D23301.

Dessler, A. E., T. F. Hanisco, and S. Fueglistaler (2007), Effects of convective ice lofting on H2O and HDO in the tropical tropopause layer, *J. Geophys. Res., 112*, D18309.

Dhomse, S., M. Weber, and J. Burrows (2008), The relationship between tropospheric wave forcing and tropical lower stratospheric water vapor, *Atmos. Chem. Phys., 8*, 471–480.

Engel, A., T. Möbius, H. Bönisch, U. Schmidt, R. Heinz, I. Levin, E. Atlas, S. Aoki, T. Nakazawa, S. Sugawara, F. Moore, D. Hurst, J. Elkins, S. Schauffler, A. Andrews and K. Boering (2009), Age of stratospheric air unchanged within uncertainties over the past 30 years, *Nature Geosci., 2*, 28-31.

Forster, P. M., G. Bodeker, R. Schofield, S. Solomon, and D. Thompson (2007), Effects of ozone cooling in the tropical lower stratosphere and upper troposphere, *J. Geophys. Res., 34*, L23813.

Gettelman, A., D. J. Seidel, M. C. Wheeler, and R. J. Ross (2002), Multidecadal trends in tropical convective available potential energy, J. Geophys. Res., 107, D21, 4606.

Hanisco, T. F., E. J. Moyer, E. M. Weinstock, J. M. St. Clair, D. S. Sayres, J. B. Smith, R. Lockwood, J. G. Anderson, A. E. Dessler, F. N. Keutsch, J. R. Spackman, W. G. Read, and T. P. Bui (2007), Observations of deep convective influence on stratospheric water vapor and its isotopic composition, *Geophys Res Lett*, *34*(4).

Homan, C. D., C. M. Volk, A. C. Kuhn, A. Werner, J. Baehr, S. Viciani, A. Ulanovski, and F. Ravegnani (2010), Tracer measurements in the tropical tropopause layer during the AMMA/ SCOUT-O3 aircraft campaign, *Atmos. Chem. Phys., 10*, 3615–3627.

Johnson, N., and S.-P. Xie (2010), Changes in the sea surface temperature threshold for tropical convection, *Nature Geoscience, 3*, 842-845.

Li, F., J. Austin, and J. Wilson (2007), The Strength of the Brewer–Dobson Circulation in a Changing Climate: Coupled Chemistry–Climate Model Simulations, *J. Climate, 21*, 40-57.

Massie, S. T., J. Gille, C. Craig, R. Khosravi, J. Barnett, W. Read, and D. Winker (2010), HIRDLS and CALIPSO observations of tropical cirrus, *J. Geophys. Res., 115*, D00H11, doi:10.1029/2009JD012100.

Park, S., R. Jiménez, B. C. Daube, L. Pfister, T. J. Conway, E.W. Gottlieb, V. Y. Chow, D. J. Curran, D. M. Matross, A. Bright, E. L. Atlas, T. P. Bui, R.-S. Gao, C. H. Twohy, and S. C. Wofsy (2007), The CO_2 tracer clock for the Tropical Tropopause Layer, *Atmos. Chem. Phys., 7*, 3989–4000.

Park, S., E. L. Atlas, R. Jiménez, B. C. Daube, E.W. Gottlieb, J. Nan, D. B. A. Jones, L. Pfister, T. J. Conway, T. P. Bui, R.-S. Gao, and S. C. Wofsy (2010), Vertical transport rates and concentrations of OH and Cl radicals in the Tropical Tropopause Layer from observations of CO_2 and halocarbons: implications for distributions of long- and short-lived chemical species, *Atmos. Chem. Phys., 10*, 6669–6684.

Ploeger, F., P. Konopka, G. Günther, J.-U. Grooß, and R. Müller (2010), Impact of the vertical velocity scheme on modeling transport in the tropical tropopause layer, *J. Geophys. Res*., *115*, D03301, doi:10.1029/2009JD012023.

Rosenlof, K. H., and G. C. Reid (2008), Trends in the temperature and water vapor content of the tropical lower stratosphere: Sea surface connection, *J. Geophys. Res.-Atmos.*, *113*(D6).

Scherer, M., H. Vomel, S. Fueglistaler, S. J. Oltmans, and J. Staehelin (2008), Trends and variability of midlatitude stratospheric water vapour deduced from the re-evaluated Boulder balloon series and HALOE, *Atmos Chem Phys*, *8*(5), 1391-1402.

Solomon, S., D. W. J. Thompson, R. W. Portmann, S. J. Oltmans, and A. M. Thompson (2005), On the distribution and variability of ozone in the tropical upper troposphere: Implications for tropical deep convection and chemical-dynamical coupling, *Geophys. Res. Lett., 32*, L23813.

Solomon, S., K. H. Rosenlof, R. W. Portmann, J. S. Daniel, S. M. Davis, T. J. Sanford, and G. K. Plattner (2010), Contributions of Stratospheric Water Vapor to Decadal Changes in the Rate of Global Warming, *Science*, *327*(5970), 1219-1223.

Trapp, R. J., N. S. Diffenbaugh, and A. Gluhovsky (2009), Transient response of severe thunderstorm forcing to elevated greenhouse gas concentrations, *Geophys. Res. Lett*., 36, L01703.

Van Klooster, S. L. and P. J. Roebber (2009), Surface-Based Convective Potential in the Contiguous United States in a Business-as-Usual Future Climate, *J. Climate, 22*, 3317-3330.